

HARVARD UNIVERSITY
Graduate School of Arts and Sciences



DISSERTATION ACCEPTANCE CERTIFICATE

The undersigned, appointed by the
Department of Physics
have examined a dissertation entitled

Microscopy of interacting quantum systems

presented by Ming Eric Tai

candidate for the degree of Doctor of Philosophy and hereby
certify that it is worthy of acceptance.

Signature A handwritten signature in blue ink.

Typed name: Professor Markus Greiner, Chair

Signature A handwritten signature in blue ink.

Typed name: Professor Melissa Franklin

Signature A handwritten signature in blue ink.

Typed name: Professor Mikhail Lukin

Date: May 5, 2017

Microscopy of interacting quantum systems

A DISSERTATION PRESENTED
BY
MING ERIC TAI
TO
THE DEPARTMENT OF PHYSICS

IN PARTIAL FULFILLMENT OF THE REQUIREMENTS
FOR THE DEGREE OF
DOCTOR OF PHILOSOPHY
IN THE SUBJECT OF
PHYSICS

HARVARD UNIVERSITY
CAMBRIDGE, MASSACHUSETTS
MAY 2017

©2017 – MING ERIC TAI
ALL RIGHTS RESERVED.

Microscopy of interacting quantum systems

ABSTRACT

Ultracold quantum gases in optical lattices provide a rich experimental toolbox for simulating the physics of condensed matter systems. With atoms in the lattice playing the role of electrons or Cooper pairs in real materials, it is possible to experimentally realize condensed matter Hamiltonians in a controlled way. To realize the full potential of such quantum simulations, we leverage a quantum gas microscope which can spatially resolve the atoms in the optical lattice at the single site level and project arbitrary potential landscapes onto the atoms by combining the high resolution optics with static holographic masks or a spatial light modulator. The versatility of this system allows for a wide range of studies. In this thesis, we focus on three experiments that highlight the utility of a tunable platform and demonstrate the richness of physics that comes with interactions.

In the first, we observe on-site interparticle interactions introduce a non-linearity into the many-body energy spectrum of a harmonic oscillator. The excitation of a single atom into a higher band induces an energy shift in the excitation energy for the second atom, blocking the orbital excitation. We demonstrate a technique for deterministic number filtering based upon orbital excitation blockade. When applied to a high temperature Mott insulator, this number filtering realizes a form of algorithmic cooling, which can be used for initializing a large quantum register or creating low entropy initial states for many-body simulation.

In the second, we study the applicability of statistical physics in an isolated system governed by quantum mechanics. While the descriptive power of these two fields has been confirmed through repeated and varied empirical studies, their underlying axioms of entropy maximization and unitary evolution appear mutually exclusive. With our quantum gas microscope, we have the ability to probe local observables such as the on-site number statistics as well as measure the quantum mechanical purity through interference operations. With these capabilities, we are able to observe the local thermalization of a manifestly quantum mechanically pure many-body system.

In the last chapter, we report on the first cold atoms studies of an interacting system under an artificial gauge field. We consider the propagation of a pair of atoms in a $2 \times N$ ladder governed by the Harper-Hofstadter model. The eigenstates of this system include both scattering states, which can exhibit chiral propagation, and bound states. A superexchange energy shift in our initial state leads to imbalanced population in the two chiral scattering sectors, leading to chiral propagation dynamics. This effect is the result of both the presence of interactions and the artificial gauge fields. These two components are essential ingredients for fractional quantum Hall physics. Moreover, the dynamic tunable gauge field we develop and the control afforded by a quantum gas microscope make this platform well-suited for future studies in this regime.

Contents

0	INTRODUCTION	4
0.1	Outline	9
1	A QUANTUM GAS MICROSCOPE WITH AN ARTIFICIAL GAUGE FIELD	11
1.1	Optical lattices	11
1.2	Bose-Hubbard model	16
1.3	Artificial gauge fields for optical lattice emulators	21
2	EXPERIMENTAL TECHNIQUES	33
2.1	Quantum gas microscopy	34
2.2	Tunable artificial gauge fields	38
2.3	Instrumentation Control	52
3	ORBITAL EXCITATION BLOCKADE AND ALGORITHMIC COOLING	67
3.1	Interaction-induced orbital excitation blockade	68
3.2	Experimental apparatus	69
3.3	Orbital excitation blockade in a Mott insulator	71
3.4	Cooling through algorithmic number filtering	73
3.5	Algorithmic cooling of a finite temperature Mott insulator	75
3.6	Technical limitations	77
3.7	Conclusion	78
4	QUANTUM THERMALIZATION OF AN ISOLATED, MANY-BODY QUANTUM SYSTEM	80
5	MICROSCOPY OF THE INTERACTING HARPER-HOFSTADTER MODEL	82
5.1	Single-particle chiral dynamics	87
5.2	Single-particle band structure	95
5.3	Single-particle chiral eigenstates	101
5.4	Interaction-induced chirality	105
5.5	Two-particle eigenstates	109
5.6	Two-particle chirality	114
5.7	Short-time perturbation theory of the interacting propagation dynamics	118
5.8	Conclusion	120

APPENDIX A ATOMIC PHYSICS	123
A.1 Two-Level Atom	124
A.2 Three-Level Atom	134
APPENDIX B ORBITAL EXCITATION BLOCKADE	137
B.1 State Preparation	137
B.2 Higher Band Removal	138
B.3 Band Dependent Energy Shifts	138
B.4 Limits on entropies achievable with algorithmic cooling	140
APPENDIX C HARPER-HOFSTADTER LADDER	141
C.1 Experimental Sequence	141
REFERENCES	155

TO MY PARENTS AND SISTERS HELEN AND CHRISTIANA.

Acknowledgments

I HAVE SPENT AN INCREDIBLY LONG TIME AT HARVARD — in fact, my PhD career represents the longest period of my life I have spent in one city. At many times, I have questioned whether I'd have anything to present before you, my few readers. For the opportunity to have something to fill these pages, I have many people to thank. I want to acknowledge my adviser, Markus Greiner, for making that April 14th call to me so many years ago and supporting my time in his group ever since. Lyman 137 and 128 have been a wonderful place for me thanks to the peerless group Markus has assembled.

On the Rubidium team, I have worked with Waseem, Amy, Simon, Jon, Alex, Philipp, Philip, Rajibul, Alex, Matthew, Robert, and Adam. In addition, I overlapped briefly with Gregor, Casey, Tim, and Elijah in the lab. I want to thank Jon for being so patient with my questions and answering the questions that I wanted to ask but could not formulate. Without him, I would have also never learned the benefits of anaerobic exercise and pondered what would happen should I get a heart attack while benching. Also, as far as I know, he was the source of the ideas behind the tunable flux scheme described in this thesis. To this day, Jon continues to support me. I also want to especially thank Philipp. Throughout my time, he has been exceptionally engaged when I have needed his help on what are ostensibly my side projects and not his problem and moreover has been a champion of my causes. I will never forget how he was one that supported me when I wanted to install

and finally finish my work on the experimental control and patiently helped debug it alongside me and never made me feel like my project was not worth his or the group's while. And despite his time in the group coming to a close and him having nothing to gain, he once again cleared the jungle for me and made the opening for me to install the gauge field optics that paved the way for much of the work in this thesis. I will also never forget those hot nights in Paris.

The lab as a whole has also been a welcoming community. In the early years, we shared the office with Widagdo, Florian, Dylan, Kate, Max*, and Sebastian on the Lithium team. Later on, Anton, Christie, Daniel, and Geoff were added and an Erbium lab magically appeared with Aaron, Anne, Susannah, and Greg. Much of my fabrication abilities, with electronics and CNC machining, can be traced back to Florian. It was truly good fortune to have been able to learn from him as well as to be neighbors in the new office. He was also a ceaseless supporter, along with Anne and Matthew, of my musical endeavors. Daniel has now taken Florian's place by my desk and has been a great neighbor for physics discussions and otherwise. He has also had a large role in keeping me focused on my work. I hope to be effective and productive like a German some day. To Geoff, Robert, and Aaron, thanks for sharing your youth with me. May we return to Chicago together once again — and then Ibiza and Belgium. Matthew, thanks for the adventures: in Taiwan, on the bike, and hunched over electronics.

Within the department at large, I want to thank Jim, Manny, Steve, Stuart, Jan, Melissa, Jean, Clare, and Lisa. These people have made the department a place where all my efforts could in principle

*Parsons, and Max Ebner.

ple be focused on research. Jim has been instrumental[†] in many of my electronics projects and been a source of solutions for many of the problems in our lab. He is truly one of the treasures of the department, though not for his technical knowledge, but his patience and kindness. I also want to mention Fabian Grusdt and Mike Foss-Feig[‡] for their pivotal efforts in helping us understand the interacting data presented here.

I want to thank my mentors at Caltech who have helped me get here. Jeff Kimble got me started in atomic physics and for two years provided a welcoming place for me to do research. All of my work at Caltech was done in conjunction with Dal, who was infinitely patient with me as he taught me the ins and outs of softball and how to work in an optics lab. Dal truly had no dog in my project, but was generous with his time and friendship. He represents all that is good in Caltech graduate students. I also want to thank Rich Dekany for the early opportunity in research he gave me. Finally, the late Tom Tombrello was quite possibly my strongest advocate at Caltech. I spent one of my early Caltech years with him and despite falling asleep and revealing my stupidity in his class so many times, he was always there to help. I never understood what he saw in me and what would compel him to use his connections on me. Yet, whenever I had a stumbling block in my career, his immediate reply was one of “let’s overcome this.” I was always treated as another one of his bright, actual prodigies[§] despite being a poor student who was perhaps too engaged in interhouse sports and not actually any good at piano. I wish I had the chance to show him this thesis.

[†]He does lead the instrument design lab after all?

[‡]Fine, he’s at JQI.

[§]Milo and Dario?

ALTHOUGH THIS THESIS IS ABOUT MY SCIENTIFIC RESEARCH IN THE GREINER LAB, I would also like to use it as an opportunity to recognize and thank the many people not directly related to this endeavor that have enriched my life and blessed me with their kindness and friendship. I came to Boston after a decade in California, apprehensive of the old houses and the city life. As I close the PhD chapter of my life, I know there is so much that I cherish here.

I know not why I brought my violin with me when I moved to Boston — despite being with me during my undergraduate years, I only removed it from its case a handful of times. I also know not how Bert convinced me to not only sign the interest sheet for the Dudley House Orchestra but to also show up at the audition. Alison was perhaps my first friend at Harvard. In that first year, Andrew, Julie, Thomas, Corinna, Audrey, and she humored my love for Bach and we made perhaps the only seven-violin octet performance of a movement of Bach's *Art of Fugue* in history. Thomas probably also has the distinction of buying the first beer that has ever touched my lips. Through the years, Mike (and Jon) never failed to invite me to tropical parties or Halloween parties. While Jeff and I will likely never share the bond of playing Tubin No. 2 together, I appreciate our many physics discussions and that amazing steak he made at that July 4th barbecue. Although I consider myself to be the primary reason Aaron was ever involved in the Dudley House Orchestra, I have received so much from his leadership of the orchestra as well as his sincere friendship. Finally, I need to thank my many stand partners, whom include: Sahand, Jung-Mee, Sevan, and Miya, among many others. They have had the most intimate hearing into my wrong notes and harsh tone. Miya has been with me the longest and I value those times we made the most of some highly questionable rehearsals. Others that have enriched my time with the Dudley House Orchestra and many of which

have also honored me by playing chamber music with me include: Mikiko, Julia, Monica, August, Lane, Ryan, Lisa, Fan, Amy, Jon, Shu-shien, Xiuye, Tim, and Nick.

Basketball at Hemenway or the MAC was another escape of mine. I have enjoyed battling it out with you all: Rui, Qian, Eric, Francisco, LT, Steve, John, David, Rob, and Omar. You have made Sunday morning basketball one of the things that I will miss should I depart Boston.

During my time at Harvard, I spent a life-changing summer in Taiwan. I want to thank Yu-Ju for humoring me in her lab for those many weeks. I hope I was able to do something remotely useful for her lab. The EAPSI group made that time unforgettable: Stephanie, John, Mylene, Jeff, Amit, Mihaela, En-ju, John, Sharon, Richard, and Janis among many others. I still remember the first morning after we were left all on our own. I was so happy to stumble upon Stephanie and Joe at the Starbucks. I hope to see you all again soon.

Outside of these groups, I want to thank Anna[¶] Aizman, who is the other candidate for my first friend at Harvard. Jean Anne, Mikey, and Alex Frenzel have been great classmates and friends. I have known Po-ling since Caltech and appreciate the many a meal we have shared in her visits to Boston. Most of all, I would like to thank Jenny for being the fearless supporter of mine that I do not deserve.

FINALLY, I want to thank my parents and sisters Helen and Christiana who have been there for me my entire life.

[¶]I am not sure if I can ever get used to Ania.

Listing of figures

1.1	Band structure of a 1D lattice	13
1.2	Bloch wavefunctions in an $8E_{\text{rec}}$ lattice	14
1.3	Wannier functions in an $8E_{\text{rec}}$ lattice	16
1.4	Aharonov-Bohm phase for neutral atoms in an optical lattice	24
1.5	Two-photon Raman processes for Λ -type atoms and doublewells	26
1.6	Unit cell of a lattice with complex-valued tunnelings	28
2.1	Optical layout of the Raman fields for a tunable artificial gauge field	39
2.2	RF circuit for Raman field acousto-optic modulator	40
2.3	Raman and lattice fields through a common objective	41
2.4	Raman and lattice fields in a shared Fourier plane	42
2.5	Raman resonance scan in a bulk Mott insulator	46
2.6	Tilt calibration using $\hbar\Delta_{\text{tilt}} - U$ bulk resonance feature	46
2.7	Site-resolved Raman resonance scan	47
2.8	Secondary Raman resonance features at high powers	49

2.9	Renormalized tunneling in a driven optical lattice	50
2.10	Heating from laser-assisted tunneling	51
2.11	Heating decay rates as a function of effective flux	52
2.12	Combining the AD9522 with the PCIe-6536	56
2.13	Analog data memory structure	60
2.14	Experimental control synchronization	62
2.15	AC 60 Hz line synchronization	65
3.1	Orbital excitation blockade mechanism in an optical lattice	70
3.2	Time, frequency and site-resolved coherent transfer of atoms in a Mott insulator between orbitals	72
3.3	Algorithmic cooling in an optical lattice	76
3.4	Experimental realization of algorithmic cooling	77
5.1	Interacting Harper-Hofstadter model on a $2 \times N$ ladder geometry	84
5.2	Artificial gauge fields with a quantum gas microscope	86
5.3	Landau-Zener state preparation of the single-particle initial state	89
5.4	Single-particle chiral dynamics in a Harper-Hofstadter ladder	90
5.5	Band structure of isolated legs of a Harper-Hofstadter ladder	97
5.6	Band structure of a Harper-Hofstadter ladder	101
5.7	Chirality of Bloch bands	103
5.8	Eigenstate decomposition of single-particle initial states	104

5.9	Two-particle chiral dynamics in a Harper-Hofstadter ladder	106
5.10	Two-particle dynamics at multiple flux values	107
5.11	Flux dependence of shearing amplitude	108
5.12	Density of states for two-particle system	109
5.13	Decomposition of interacting eigenstates into free two-particle eigenstates	112
5.14	Bound and unbound dynamics in two-particle propagation	115
5.15	Initial state decomposition into and chiral character of many-body eigenstates . . .	116
5.16	Perturbation expansion of propagation dynamics	119
5.17	Theory comparison between perturbation theory and exact diagonalization	120
C.1	Experimental sequence for Harper-Hofstadter experiments	142
C.2	State preparation	145

*Almighty God, Who hast created man in Thine own
image, and made him a living soul that he might seek
after Thee, and have dominion over Thy creatures, teach
us to study the works of Thy hands, that we may subdue
the earth to our use, and strengthen the reason for Thy
service.*

James Clerk Maxwell

0

Introduction

OUT OF THE COMPLEXITY OF INTERACTING QUANTUM SYSTEMS often emerges physics that is both novel and rich. While a single electron exhibits comparatively elementary behavior — accelerating along electric field lines or executing cyclotron orbits in a magnetic field — ensembles of electrons can exhibit startlingly counterintuitive behavior. In a BCS superconductor, weak attrac-

tive interactions between constituent Fermions drive the formation of Cooper pairs that leads to superconductivity^{16,15}. In the presence of a magnetic field, Laughlin states⁵⁵ can emerge in 2D multi-electron systems — electrons minimize their energy by forming a highly-entangled state in which any given electron is in a superposition of being in the vortices formed by every other electron.

While the complexity of many-body systems underlies their rich physics, it also challenges their study. In a top-down approach, such as with solid-state paradigms or bulk quantum gases, it is easy to reach the many-body, strongly-interacting regime. However, microscopic probes that allow for the study of correlations are often unavailable and creating clean, reproducible, disorder-free systems can be subject to significant fabrication challenges. On the other hand, bottom-up approaches, for example with trapped ions¹⁹ or superconducting qubits⁴⁵, allow for full quantum control and readout, but present technical challenges for scaling to higher particle numbers and higher dimensions.

In the last decade, quantum gas microscopy¹¹ has emerged as a compelling avenue towards the study of interacting quantum systems. Under this experimental paradigm, high-resolution optical techniques are combined with ultracold quantum gases to realize Feynman’s proposal³¹ of using one quantum system to imitate another. The constituent atoms of the ultracold quantum gas interact with each other and a lattice potential created using light fields. At sufficiently low temperatures, this system exhibits behavior representative of electron gases in crystals⁴⁹. The imaging system, commonly based upon a high numerical aperture microscope objective, is used for the detection of the atomic distribution within the lattice and is capable of imaging atoms on individual lattice sites, allowing for the measurements of local observables and correlation functions.

In these systems, it is straightforward to realize two-dimensional geometries and since they are

often loaded from bulk quantum gases, high particle numbers are attainable. Despite this scalability, these experiments retain the ability to probe microscopically, with single-site resolution^{11,88,75} and in some cases number-resolved detection⁸⁰. In addition to the length scales being experimentally favorable, the relevant energy scales — 1 kHz to 10 Hz, corresponding to timescales of 1 ms to 100 ms — are often easily probed with current technology.

Another advantage of this approach is the tunability of the system. For imaged optical lattices, changing the geometry does not require manipulating the laser wavelengths¹¹. With phase-stabilized beams, it is possible to leverage interference effects to dynamically tune lattice geometries³⁵. In these lattices, it is easy to achieve a wide range of tunneling strengths through manipulation of optical powers. With certain atomic species, it is also possible to tune interparticle interactions by varying the magnetic field strength and leveraging Feshbach resonances. Finally, spatial light modulators⁹⁸ enable the projection of ultra-precise, nearly arbitrary light potentials.

Quantum gas microscopes have proven to be an effective system for studying quantum many-body physics. The on-site number fluctuations and adiabaticity timescales across the superfluid to Mott insulator transition¹¹ have been probed with single-site resolution. Spectroscopic measurements have revealed the presence of a Higgs mode, a collective excitation, in a superfluid near the quantum phase transition to the Mott-insulating state³⁰. Quantum magnetic phase transitions have been studied on a microscopic level with systems of pseudo-spins⁸⁹ and real spins (hyperfine states of ${}^6\text{Li}$)^{76,65}. In the latter experiments, long-range antiferromagnetic correlations have been observed and allowed for the benchmarking of various numerical techniques. The possibility of local manipulation and control^{32,98} has enabled investigations of the propagation of bound magnon states in

spin chains³² and the effects of quantum statistics in strongly-correlated quantum walks⁷⁹.

In this thesis, I present experiments conducted with a quantum gas microscope for bosonic Rubidium atoms. The versatility of this apparatus has enabled a broad array of investigations that probe interactions and many-body phenomena. In describing the technical backbone of the apparatus, I provide an in depth description of our instrumentation control and our novel technique for generating a tunable artificial magnetic field. With this apparatus we (1) investigate an interaction blockade mechanism¹⁴ useful for creating ultralow entropy initial states for quantum computing and many-body physics, (2) perform a foundational study on thermalization⁵² of an isolated quantum many-body system and (3) study a fundamental unit of larger chiral matter by performing the first studies of an interacting Harper-Hofstader system.

ORBITAL EXCITATION BLOCKADE In the Bose-Hubbard model, atoms interact via an on-site pairwise repulsion. For a pair of atoms situated on the same lattice site, this interaction energy will depend on the orbitals each atom occupies, i.e. the interaction energy of two particles in the ground orbital differs from that of one in the ground and one in the excited orbital or that of both in the excited orbital. Hence, the excitation of an atom to the excited orbital blockades the excitation of the second atom, a phenomena we term orbital excitation blockade.

In this work, we leverage orbital excitation to perform number filtering of a Mott insulator, the ground state of the Bose-Hubbard model in the strongly-interacting regime. Since the excitations in this regime are number fluctuations, this process is an example of algorithmic cooling. Using this technique, we are able to take a large thermal cloud and cool it to create a Mott insulator of

hundreds of atoms. This technique could be used to initialize the ultralow entropy states needed for many-body physics. In addition, the blockade technique can be leveraged for a controlled-NOT gate.

QUANTUM THERMALIZATION OF AN ISOLATED MANY-BODY SYSTEM The empirical evidence for both statistical physics and quantum physics is beyond reproach, yet fundamental premises of each, entropy maximization and unitary evolution seem at odds. With the pioneering ability to measure the purity of a quantum state^{48,78} and the scalability to probe a many-body state, our quantum gas microscope is uniquely poised to perform foundational experiments exploring this seeming dichotomy.

In these studies⁵², we quench our system to populate excited states where theories such as the eigenstate thermalization hypothesis are pertinent. Through measurements of the local entanglement entropy, we are able to identify a thermalization time and in the period following this time, we find the expected volume-law scaling of the entanglement entropy. Indeed, we find that thermodynamic predictions predicated on entropy maximization are consistent with the observed on-site number statistics of the thermalized state. In spite of what appears to be local thermalization, however, measurements of the quantum mechanical purity indicate that the state has remained globally pure and isolated from the environment.

MICROSCOPY OF THE INTERACTING HARPER-HOFSTADTER MODEL The combination of strong interactions and a gauge field leads to fractional quantum Hall physics. Using laser-assisted

tunneling to dress our Hamiltonian, we realize these elements by engineering the Harper-Hofstadter model. We investigate the edge modes present when this system is confined with hard boundaries.

Our studies of the propagation dynamics reveal the underlying chiral band structure.

We controllably introduce interactions by adding an additional particle. This system represents a fundamental building block by virtue of retaining all of the essential ingredients for chiral many-body states. We synthesize and probe this fundamental building block using a new scalable toolset, allowing the incremental creation of more complex systems. While top-down approaches to chiral matter can reach many-body physics, the complicated nature of such states often precludes the microscopic study and low entropies achieved in our work. Indeed, even in the two-particle limit explored by this experiment, we observe the complexity of the underlying physics associated with the synergy of interactions and gauge fields.

0.1 OUTLINE

The thesis is structured as follows:

CHAPTER 1 provides a theoretical overview of the scientific infrastructure behind our experimental apparatus. I cover the eigenstate spectrum of a single particle in an optical lattice and sketch a derivation for the many-body system, leading to the Bose-Hubbard Hamiltonian and a discussion of the superfluid and Mott insulator ground states. I conclude the chapter by discussing the use of laser-assisted tunneling to simulate a magnetic field in a Bose-Hubbard system.

CHAPTER 2 focuses on the technical details that buttress the quantum gas microscope as realized in this work specifically. I begin by briefly describing the core optical aspects and then describe our new tunable artificial gauge field scheme. I include a discussion of relevant techniques for calibrating the laser-assisted tunneling used for generating the flux. The chapter concludes with discussion of the instrumentation control system.

CHAPTER 3 focuses on our investigations of the orbital excitation blockade phenomenon introduced above, describing the effect and then demonstrating its utility in realizing a form of algorithmic cooling.

CHAPTER 4 focuses on our studies of the quantum thermalization and presents evidence of a state that is locally thermal with respect to subsystem entanglement entropy and volume-law scaling yet manifestly quantum mechanically pure.

CHAPTER 5 focuses on our microscopic studies of the Harper-Hofstadter model, detailing our single-particle and two-particle experiments as well as the theory to understand the observations of chiral propagation dynamics.

CHAPTER 6 provides a brief summary and describes future avenues for each of the experimental forays documented in this thesis.

Since it is good to stay on terra cognita as long as possible...

Eugene P. Wigner

1

A quantum gas microscope with an artificial gauge field

1.1 OPTICAL LATTICES

Within the two-dimensional plane of our atoms, the main tool we use for creating the potential energy landscape is the optical lattice. This lattice is created through the interference of two Gaussian

beams. If two equal intensity beams intersect with an angle θ_{NA} at the origin, they will form a periodic intensity distribution given by $I(x, y)$ for $r = \sqrt{x^2 + y^2}$ much less than the waist of the beams,

$$I(x, y) = I_0 \cos^2(k_{\text{latt}}x), \quad k_{\text{latt}} = k_{\text{laser}} \sin \theta_{\text{NA}}.$$

If we introduce a second pair that only interferes with itself and not the first pair, we have the potential

$$I(x, y) = I_0 [\cos^2(k_{\text{latt}}x) + \cos^2(k_{\text{latt}}y)].$$

In the limit that the light fields are far-detuned from any atomic resonance, they will induce an AC Stark shift* in the atoms, which maps the intensity profile to an energy landscape. The result is a regular square lattice with lattice vectors along the e_x and e_y directions and lattice spacing of

$$a \equiv \pi/k_{\text{latt}} = \frac{\pi}{k_{\text{laser}} \sin(\theta_{\text{NA}})}.$$

1.1.1 BAND STRUCTURE

Bloch's theorem states that the single-particle eigenstates of such a system can be written in the form

$$\phi_q^{(n)}(x) = e^{iqx/\hbar} u_q^{(n)}(x),$$

*See Appendix for how to calculate the AC Stark shift for Rubidium.

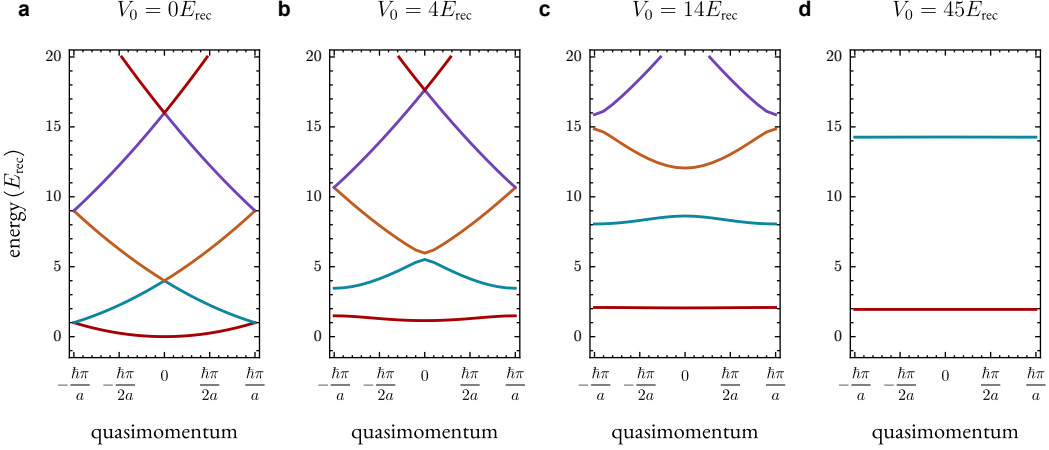


Figure 1.1: Band structure of a 1D lattice: The eigenstates of an optical lattice can be described by a Bloch wavefunction characterized by a band index and quasimomentum. Plotted are the first few bands for various lattice depths given in units of the recoil energy $E_{\text{rec}} = \hbar^2 k_{\text{latt}}^2 / (2m)$. As the lattice depth is increased, the bands depart from the parabolic, free-particle shape to flat bands of a harmonic oscillator.

where $u^{(n)}(x)$ is a function with periodicity that matches the lattice, i.e. it is periodic in $\pi/k = a$.

These states are labeled with a band index $n \in \mathbb{Z}_+$. The quasimomentum q is restricted to the interval $[-\pi/a, \pi/a]$ since higher frequencies can be incorporated into the periodic on-site functions $u_q^{(n)}(x)$. Physically, this corresponds to restricting our solutions to the first Brillouin zone.

Using this ansatz, it is straightforward[†] to compute the eigenstates, $\phi_q^{(n)}$, and eigenenergies, $E_q^{(n)}$.

In Figure 1.1 and Figure 1.2, we plot the band structure and eigenstates at a few representative lattice depths expressed in units of the recoil energy,

$$E_{\text{rec}} = h\nu_{\text{rec}} = \hbar\omega_{\text{rec}} = \frac{\hbar^2 k_{\text{latt}}^2}{2m}.$$

For low lattice depths, the system approaches a free system where the Hamiltonian consists of

[†]For one formulation of the solution, see §3.1.3 of Reference³⁷

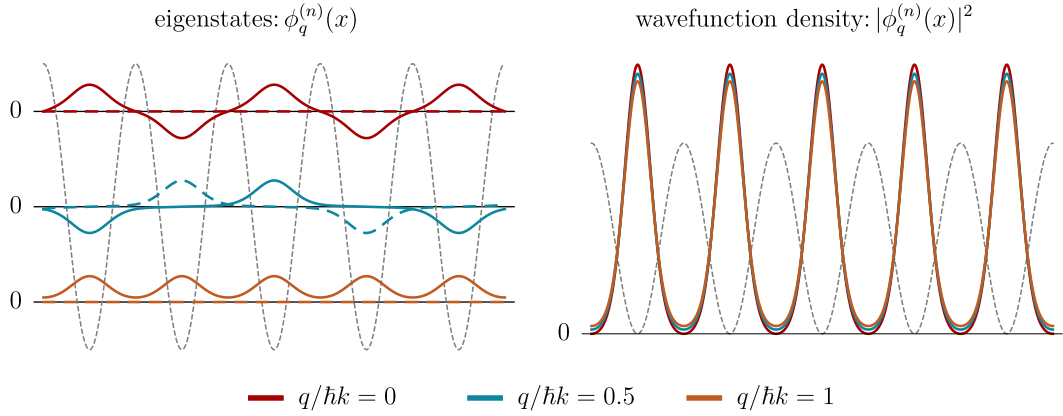


Figure 1.2: Bloch wavefunctions in an $8E_{\text{rec}}$ lattice: The Bloch wavefunctions are composed of a plane wave component describing the phase evolution from site to site and a periodic component that describes the on-site shape of the function. These states are only defined for quasimomenta in the interval $[-\pi/a, \pi/a]$, i.e. the first Brillouin zone, because higher spatial frequencies can be incorporated into the on-site component of the wavefunction. The real (solid) and imaginary (dashed) parts of the Bloch wavefunctions with quasimomenta $q/\hbar k = \{0, 0.5, 1\}$ in the lowest band are plotted in the left panel. The density for these states is plotted in the right panel. These wavefunctions were computed for an $8E_{\text{rec}}$ depth lattice. This figure is reproduced with permission from Reference⁶¹.

only a kinetic energy term. Thus, at low depths, the energy spectrum is parabolic. As the lattice depth is increased, the wavefunction is squeezed into the lattice sites. Confining the population more tightly into the periodically spaced lattice sites requires mixing in Fourier components that differ by $2\hbar k$, which corresponds to states at the same quasimomentum but in a higher band. Formally, a sinusoidal lattice potential $V(x)$ can be decomposed into $e^{\pm i2kx}$ Fourier components. Hence, the lattice depth appears along the off-diagonal for a Hamiltonian written in the Bloch basis. The effect of this coupling is to cause the states at a particular quasimomentum to repel each other, resulting in the opening of a band gap and flattening of the bands. The bandwidth decreases exponentially with the lattice depth. In the deep lattice limit, the population is largely confined to the quadratic minima of the optical potential, resulting in equally spaced bands matching that of a

harmonic oscillator. The spacing can easily be related to the lattice depth.

$$E_{n+1} - E_n = \hbar (\omega_{n+1} - \omega_n) = 2E_{\text{rec}} \sqrt{V_0/E_{\text{rec}}}.$$

1.1.2 WANNIER STATES

Wannier functions are an alternative basis for describing states in an optical lattice. In contrast to the completely delocalized Bloch states, the Wannier states are localized to individual lattice sites. For low temperature systems, it is common that band gaps prevent the populating of higher energy bands. When tunneling matrix elements or interaction energies are computed, as will be done in the next section, it is important that our basis does not consider unphysical contributions from higher bands. Hence, in constructing these states, we restrict the superposition to eigenstates of a particular band. In terms of the Bloch states, the Wannier function located at site i in band n is given by,

$$w_n(x - x_i) = \frac{1}{\sqrt{N}} \sum_q e^{-iqx_i/\hbar} \phi_q^{(n)}(x). \quad (1.1)$$

In order to completely specify the Wannier states, the phase of the Bloch states $\psi_q^{(n)}$ must also be fixed. Commonly, these phases are chosen to yield a maximally localized function. A complete discussion of the procedure can be found in Reference ⁶¹. The result is reproduced below

$$\psi_q^{(n)}(x) \rightarrow \begin{cases} \psi_q^{(n)}(x) \cdot \exp \left[-i \arg \left(\psi_q^{(n)}(x_i) \right) \right], & n \text{ even} \\ \psi_q^{(n)}(x) \cdot \exp \left[-i \arg \left(\left. \frac{d\psi_q^{(n)}(x)}{dx} \right|_{x=x_i} \right) \right], & n \text{ odd.} \end{cases}$$

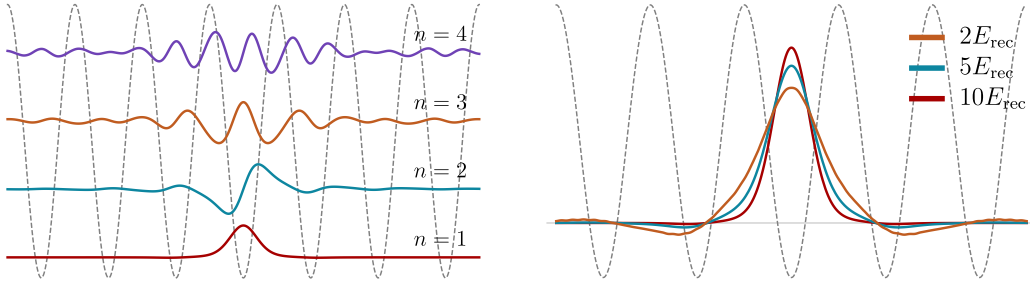


Figure 1.3: Wannier functions in an $8E_{\text{rec}}$ lattice: The Wannier states are often defined as the most localized states possible with linear combinations of Bloch wavefunctions of a single given band. Plotted on the left are the Wannier functions for the first four bands. As the lattice depth is increased, the Wannier states become increasingly localized on the lattice site. On the right, the Wannier functions are plotted for lattice depths of $[2E_{\text{rec}}, 5E_{\text{rec}}, 10E_{\text{rec}}]$. This figure is reproduced with permission from Reference⁶¹.

In Figure 1.3, we plot the Wannier functions for the first few bands and for a few example lattice depths.

1.2 BOSE-HUBBARD MODEL

In order to account for interparticle interactions, we use second quantization to formulate the many-body Hamiltonian,

$$\begin{aligned} \mathcal{H} = & \int d\mathbf{r} \hat{\Psi}^\dagger(\mathbf{r}, t) \left[-\frac{\hbar^2}{2m} \nabla^2 + V(\mathbf{r}) \right] \hat{\Psi}(\mathbf{r}, t) \\ & + \frac{1}{2} \int d\mathbf{r} d\mathbf{r}' \hat{\Psi}^\dagger(\mathbf{r}, t) \hat{\Psi}^\dagger(\mathbf{r}', t) V(\mathbf{r} - \mathbf{r}') \hat{\Psi}(\mathbf{r}, t) \hat{\Psi}(\mathbf{r}', t), \end{aligned} \quad (1.2)$$

where $\hat{\Psi}$ and $\hat{\Psi}^\dagger$ are bosonic annihilation and creation field operators, respectively. The potential $V(\mathbf{r})$ includes both the sinusoidal lattice potential and any other additional external potentials, i.e. a harmonic confining potential, that we will assume to vary slowly on the scale of the lattice

spacing. The second term accounts for the two-body interaction, where $V(\mathbf{r} - \mathbf{r}')$ describes the interparticle potential. In the ultracold limit of the experiments presented in this thesis, the many-body Hamiltonian reduces to the simple Bose-Hubbard Hamiltonian⁴⁹.

Instead of working with the field operators, it is convenient to use generalized versions of the Wannier functions we developed earlier. We introduce bosonic creation and annihilation operators $\hat{a}_{n,i}$ and $\hat{a}_{n,i}^\dagger$, which create and destroy a particle in the Wannier state of the n th band located at site i . In terms of the creation field operator and the Wannier function, the creation operator should have the following action on the vacuum state,

$$\hat{a}_{n,i}^\dagger |vac\rangle \equiv \int d\mathbf{r} \hat{\Psi}^\dagger(\mathbf{r}) w_n(\mathbf{r} - \mathbf{r}_i), \quad (1.3)$$

where we have implicitly generalized the one-dimensional Wannier functions developed earlier to the dimensions[‡] of \mathbf{r} and \mathbf{r}_i is the spatial location of site i . These operators obey the commutation relation $[\hat{a}_i, \hat{a}_j^\dagger] = \delta_{ij}$, which follows immediately from the orthonormality of the Wannier states and the commutation relation of the field operators. Now we want to rewrite the many-body Hamiltonian, Equation 1.2, in terms of these new operators. First, we derive an expression for the creation field operator by projecting it out of the definition in Equation 1.3.

$$\sum_i w_n^*(\mathbf{r}' - \mathbf{r}_i) \hat{a}_{i,n}^\dagger = \int d\mathbf{r} \hat{\Psi}^\dagger(\mathbf{r}) \sum_i w_n^*(\mathbf{r}' - \mathbf{r}_i) w_n(\mathbf{r} - \mathbf{r}_i)$$

[‡]For the separable lattice considered in this work, the three-dimensional analog is simply a product of Wannier functions in each direction, i.e. $w_0(\mathbf{r} - \mathbf{r}_i) = w_0(x - x_i) \cdot w_0(y - y_i) \cdot w_0(z - z_i)$.

We use the definition of the Wannier functions, Equation 1.1 to expand in terms of the Bloch functions, $\phi_q^{(n)}(\mathbf{r})$.

$$\begin{aligned} \sum_i w_n^*(\mathbf{r}' - \mathbf{r}_i) \hat{a}_{i,n}^\dagger &= \int d\mathbf{r} \hat{\Psi}^\dagger(\mathbf{r}) \sum_{i,n} \left[\frac{1}{\sqrt{\mathcal{N}}} \sum_q e^{i\mathbf{q}\cdot\mathbf{r}_i/\hbar} \left(\phi_q^{(n)}(\mathbf{r}') \right)^* \right] \\ &\quad \times \left[\frac{1}{\sqrt{\mathcal{N}}} \sum_p e^{-i\mathbf{p}\cdot\mathbf{r}_i/\hbar} \phi_p^{(n)}(\mathbf{r}) \right] \\ \sum_i w_n^*(\mathbf{r}' - \mathbf{r}_i) \hat{a}_{i,n}^\dagger &= \int d\mathbf{r} \hat{\Psi}^\dagger(\mathbf{r}) \frac{1}{\mathcal{N}} \sum_{p,q} \left(\phi_q^{(n)}(\mathbf{r}') \right)^* \phi_p^{(n)}(\mathbf{r}) \sum_i e^{i(\mathbf{q}-\mathbf{p})\cdot\mathbf{r}_i/\hbar} \end{aligned}$$

The identity $\mathcal{N}^{-1} \sum_i e^{i(\mathbf{q}-\mathbf{p})\cdot\mathbf{r}_i/\hbar} = \delta_{qp}$ allows us to remove one of the summation indices.

$$\sum_i w_n^*(\mathbf{r}' - \mathbf{r}_i) \hat{a}_{i,n}^\dagger = \int d\mathbf{r} \hat{\Psi}^\dagger(\mathbf{r}) \sum_q \left(\phi_q^{(n)}(\mathbf{r}') \right)^* \phi_q^{(n)}(\mathbf{r})$$

Finally, we use the completeness of the Bloch functions.

$$\begin{aligned} \sum_i w_n^*(\mathbf{r}' - \mathbf{r}_i) \hat{a}_{i,n}^\dagger &= \int d\mathbf{r} \hat{\Psi}^\dagger(\mathbf{r}) \delta(\mathbf{r} - \mathbf{r}') \\ \Rightarrow \hat{\Psi}(\mathbf{r}) &= \sum_i w_n(\mathbf{r} - \mathbf{r}_i) \hat{a}_{i,n} \end{aligned}$$

With substitution of this relation into the many-body Hamiltonian (Equation 1.2), we obtain

$$\mathcal{H} = \underbrace{- \sum_{ij} J_{ij} \hat{a}_i^\dagger \hat{a}_j}_{\text{tunneling}} + \underbrace{\frac{1}{2} \sum_{ijkl} U_{ijkl} \hat{a}_i^\dagger \hat{a}_j^\dagger \hat{a}_k \hat{a}_l}_{\text{interactions}} + \underbrace{\sum_i \epsilon_i a_i^\dagger a_i}_{\text{external potential}} . \quad (1.4)$$

The term ε_i is straightforward to compute since we assume the external potential is a slowly-varying envelope, hence $\varepsilon_i = V_{\text{ext}}(x_i)$. The tunneling matrix elements J_{ij} and the interaction terms U_{ijkl} can be computed from integrals of the Wannier functions,

$$J_{ij} = \int d\mathbf{r} w_0^*(\mathbf{r} - \mathbf{r}_i) \left[\frac{\hbar^2}{2m} \nabla^2 + V_{\text{latt}}(\mathbf{r}) \right] w_0(\mathbf{r} - \mathbf{r}_j)$$

$$U_{ijkl} = \int d\mathbf{r} d\mathbf{r}' w_0^*(\mathbf{r} - \mathbf{r}_i) w_0^*(\mathbf{r}' - \mathbf{r}_j) w_0(\mathbf{r} - \mathbf{r}_k) w_0(\mathbf{r}' - \mathbf{r}_l) V(\mathbf{r} - \mathbf{r}').$$

The experiments in this thesis occur at the low energy limit where the interparticle potential can be approximated by a contact interaction of the form

$$V(\mathbf{r}) = \frac{4\pi\hbar^2 a_s}{m} \delta(\mathbf{r})$$

where $\delta(\mathbf{r})$ is a Dirac delta function in three dimensions and the the s -wave scattering length, a_s , parametrizes the strength of the interaction.

In the tight-binding limit, we treat the atoms as being well-localized to a single lattice site and thus consider only nearest neighbor tunneling matrix elements and on-site interaction terms. This approximation leads to the Bose-Hubbard Hamiltonian,

$$\mathcal{H} = \frac{U}{2} \sum_{i,j} \hat{n}_{i,j} (\hat{n}_{i,j} - 1) - \sum_{\langle i,j \rangle} \left(J \hat{a}_{i,j+1}^\dagger \hat{a}_{i,j} + \text{h.c.} \right), \quad (1.5)$$

where U is an on-site, pairwise repulsive interaction energy, J is a tunneling amplitude between

nearest neighbors, $\langle ij \rangle$, on the lattice. The tunneling matrix element, $J \equiv J_{01}$, is directly given by the bandwidth of the ground band,

$$J = \frac{1}{4} \left(\max(E_q^{(0)}) - \min(E_q^{(0)}) \right),$$

which exponentially decreases with the lattice depth. The interaction energy, $U \equiv U_{0000}$, is given by an integral of the Wannier functions,

$$U = \frac{4\pi\hbar^2 a_s}{m} \int d\mathbf{r} |w(\mathbf{r})|^4.$$

In the deep lattice limit, the Wannier functions can be approximated with Gaussian functions and yield

$$U = \hbar \sqrt{\omega_x \omega_y} \sqrt{\frac{2}{\pi}} \frac{a_s}{\ell_z},$$

where ω_x and ω_y are the trap frequencies in the xy plane, and ℓ_z is the harmonic oscillator length in the z direction. While this expression overestimates the interaction energy, the dependence on the lattice depth can be gleaned. Since $\omega_i \sim \sqrt{V_i}$, the interaction energy only has a fourth root dependence on any given lattice depth. Given the tunneling term's exponential dependence and the interaction term's weak fourth root dependence, the ratio of these two terms, U/J , can be varied widely by tuning the lattice depth, which can be done easily through the optical power. The interaction term has stronger dependence with the lattice spacing, i.e. $U \sim \sqrt{k_i}$ where k_i is the wavevector of a single lattice direction, and thus is more useful for increasing the interaction energy.

1.3 ARTIFICIAL GAUGE FIELDS FOR OPTICAL LATTICE EMULATORS

Ultracold atoms have been an effective experimental paradigm for studying quantum many-body physics. In these systems, timescales and spatial structures are often at experimentally feasible levels for investigation. This has allowed for many studies into systems of interacting particles. The on-site number fluctuations and adiabaticity timescales have been probed in the superfluid to Mott insulator transition¹¹. Quantum magnetic phase transitions have been studied with systems of pseudo-spins⁸⁹ and with hyperfine spins⁷⁵. Cavity-mediated interactions have allowed the realization of long-range interactions and the Dicke model¹⁸, resulting in the observation of a supersolid phase⁵⁶. These systems are characterized by an order parameter and can be understood through the lens of spontaneous symmetry breaking. This picture, however, is inadequate for topological phases of matter, for example, quantum hall states. These states are instead characterized by topological invariants, such as the Chern number. The topological nature of these states is often directly related to an underlying gauge field. Studying topological order arising from a gauge field is and has been an on-going focus within the cold atoms community.

The most familiar example of a gauge field is the magnetic field. Incorporating such a field into a cold atoms experiment is nontrivial. Experiments with itinerant particles, i.e. if we exclude trapped ion experiments, are almost exclusively concerned with neutral atoms, for which a real magnetic field does not result in a Lorentz-type force.

Many techniques have been developed to emulate gauge fields in systems of ultracold neutral atoms^{63,59,50,54,62,3,60,6}. In these experiments, rotation and laser-assisted tunneling have both been

used to induce a Lorentz-like force in neutral atoms. Using the former technique, the magnetic field arises from a mathematical equivalence between the Lorentz force and the Coriolis force. In these experiments, the magnetic field drives the formation of a lattice of Abrikosov vortices, each of which carry a quantum of magnetic flux^{100,26}. Quite recently, experiments with arrays of rotating micro-traps have observed signatures of FQH states through photoassociation measurements³⁴. Using laser-assisted tunneling, the Harper-Hofstadter Hamiltonian has been realized through Floquet engineering^{5,68}, an example of the Peierls prescription for incorporating a magnetic field in a tight-binding Hamiltonian. These experiments have been able to investigate a number of single-particle effects, e.g. chiral edge currents⁶⁴, skipping orbits⁹², and the topological Chern number of bands⁷.

To simulate a magnetic field in our Rubidium quantum gas microscope, we modify the tunneling terms in the Bose-Hubbard model such that complex phases are associated with certain tunneling processes, realizing the Harper-Hofstadter Hamiltonian,

$$\mathcal{H} = \frac{U}{2} \sum_{i,j} \hat{n}_{i,j} (\hat{n}_{i,j} - 1) - \sum_{i,j} \left(K e^{-i\phi_{i,j}} \hat{a}_{i+1,j}^\dagger \hat{a}_{i,j} + J \hat{a}_{i,j+1}^\dagger \hat{a}_{i,j} + \text{h.c.} \right). \quad (1.6)$$

Tunneling in the x direction is now parametrized by a strength K and is associated with a spatially-dependent complex phase known as the Peierls phase. This model was pioneered in the Ketterle group at MIT⁶⁸ and the Bloch group in Munich⁶ using laser-assisted tunneling techniques^{50,54}.

The correspondence between complex-valued tunneling and a magnetic field is readily seen by recalling the Aharonov-Bohm phase. When a particle traverses a closed contour, \mathcal{C} , it acquires a phase, the Aharonov-Bohm phase Φ_{AB} , given by the magnetic flux piercing the surface, \mathcal{S} , formed

by the closed contour,

$$\Phi_{AB} = \frac{q}{\hbar} \iint_S \mathbf{B} \cdot d\mathbf{S}. \quad (1.7)$$

Using Stokes' Theorem, the Aharonov-Bohm phase can be rewritten as a line integral of a vector potential, \mathbf{A} ,

$$\Phi_{AB} = \frac{q}{\hbar} \int_{\partial S} \mathbf{A} \cdot d\ell. \quad (1.8)$$

For a particle tunneling around a unit cell as shown in Figure 1.4, the line integral for this path can be subdivided,

$$\int_{\partial S} = \int_{A \rightarrow B} + \int_{B \rightarrow C} + \int_{C \rightarrow D} + \int_{D \rightarrow A} \quad (1.9)$$

$$\Rightarrow \Phi_{AB} = \phi_{A \rightarrow B} + \phi_{B \rightarrow C} + \phi_{C \rightarrow D} + \phi_{D \rightarrow A} \quad (1.10)$$

For a real magnetic field, if $q = 0$ as with neutral atoms, each of the $\phi_{X \rightarrow Y}$ are trivial. However, on a lattice, the phases $\phi_{X \rightarrow Y}$ can be mimicked by the phases associated with the tunneling processes connecting sites X and Y . By engineering the tunneling elements to give a non-zero phase for a circuit around a unit cell, we can emulate a non-zero Aharonov-Bohm phase, thereby simulating a non-zero field piercing that unit cell. We term this effective Aharonov-Bohm phase the flux per unit cell, even though what we are calling the flux is actually $q/\hbar \times$ (effective magnetic flux). Finally, we note that the flux per unit cell is directly proportional to the strength of the synthetic magnetic field.

From Equation 1.10, we can see that since the flux per unit cell is determined by the sum of four

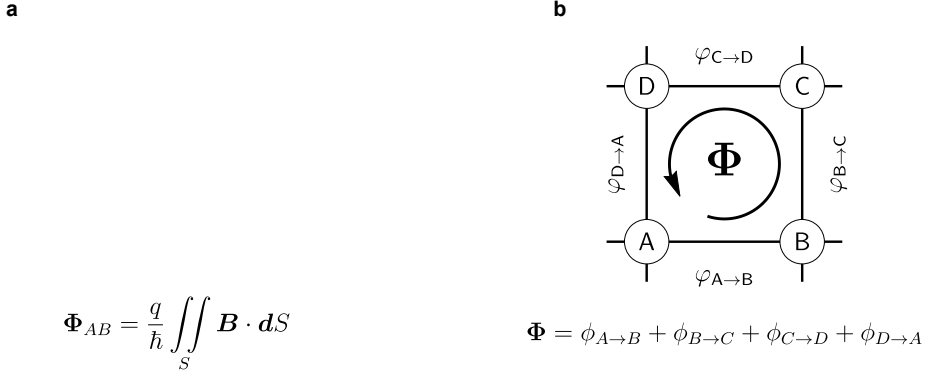


Figure 1.4: Aharonov-Bohm phase for neutral atoms in an optical lattice: **a** A charged particle traversing a closed circuit in space will acquire an Aharonov-Bohm phase directly related to the magnetic flux enclosed by that closed contour. **b** A particle hopping around a unit cell of a lattice acquires a phase given by the sum of the complex phases of the four tunneling elements. This phase can be interpreted as an Aharonov-Bohm phase from an effective magnetic field.

phases, there are actually multiple ways of achieving the same magnetic field. This is a manifestation of gauge freedom. Each arrangement of phases represents a different effective vector potential, but each vector potential can give the same synthetic magnetic field.

In contrast to free systems, optical lattice systems allow us to more easily reach a strongly interacting regime. High fields are also readily reached by increasing the complex phase associated with the tunneling process. To reach Φ flux per plaquette in a solid-state system with a lattice spacing of order 1 \AA would require a magnetic field strength of

$$\frac{q}{\hbar} \times B \cdot (1 \text{ \AA})^2 = \Phi \Rightarrow B = \frac{\Phi}{(1 \text{ \AA})^2} \frac{\hbar}{q}.$$

For $\Phi = \pi/2$, which has been demonstrated by many experiments^{6,68} including those presented in this thesis, one would need a laboratory magnetic field of strength 10^6 T .

1.3.1 LASER-ASSISTED TUNNELING

In our experiment, we use laser-assisted tunneling, as proposed by Jaksch⁵⁰ and Kolovsky⁵⁴ and realized by the Bloch⁶ and Ketterle⁶⁸ groups, to engineer the complex phases necessary to realize the Harper-Hofstadter model.

The laser-assisted tunneling process is analogous to a two-photon Raman transitions in a three-level Λ -type system. We consider the three-level system shown in Figure 1.5 with driving fields

$\mathbf{E}_1(r, t)$ and $\mathbf{E}_2(r, t)$,

$$\mathbf{E}_i(t) = \hat{\varepsilon} \mathcal{E}_i(r, t) e^{-i\nu_i t} + \hat{\varepsilon} \mathcal{E}_i^*(r, t) e^{i\nu_i t},$$

where $\hat{\varepsilon}$ is the polarization of the field and $\hbar\omega_{ij} = |E_i - E_j|$ are the transition frequencies. We treat the atom-field interaction within the dipole approximation as well as make the slowly-varying envelope approximation[§], resulting in the following Hamiltonian for the system,

$$\mathcal{H} = -\hbar (\omega_{12}|2\rangle\langle 2| + \omega_{13}|3\rangle\langle 3|) - \hat{d} \cdot (\mathbf{E}_1(t) + \mathbf{E}_2(t)).$$

After transforming to a rotating frame, making the rotating-wave approximation, and taking the far-detuned limit where $\delta_i \ll \Omega_i$ (See §A.2), we arrive at the Hamiltonian in the rotating frame,

$$\mathcal{H}_{\text{RF}} = -\hbar (\delta_1|2\rangle\langle 2| + \delta_1|1\rangle\langle 1|) + \hbar\Omega_1(|3\rangle\langle 1| + |1\rangle\langle 3|) + \hbar\Omega_2(|2\rangle\langle 3| + |3\rangle\langle 2|),$$

[§]In the *slowly-varying envelope approximation*, we take the length scale and time scale over which the field changes to be much smaller than the wavelength ($2\pi/|\mathbf{k}_i|$) and the period ($1/\nu_i$), respectively.

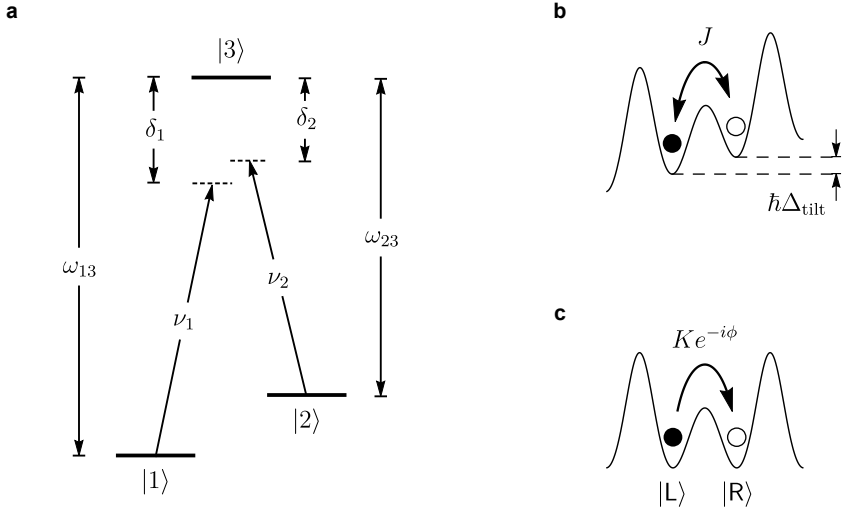


Figure 1.5: **a** A three-level Λ -type atom has two ground states, $|1\rangle$ and $|2\rangle$, and an excited state $|3\rangle$. In the presence of coherent driving fields at ν_1 and ν_2 , detuned from the $|1\rangle \rightarrow |3\rangle$ and $|2\rangle \rightarrow |3\rangle$ transitions, effective two level dynamics emerge. The effective coupling element carries a non-zero complex phase given by the phase of the Raman lasers at the spatial location of the atom. **b** Shown is a doublewell with tunnel coupling J between the left and right sites. The tilt causes a zero-point energy difference between the sites of $\hbar\Delta_{\text{tilt}}$. **c** Using Raman coupling fields, an effective resonant coupling between the two sites can be induced. This coupling in general is complex-valued.

where we have defined the single-photon detunings and introduced Rabi frequencies,

$$\nu_i - \omega_{i3} = \delta_i, \quad \hbar\Omega_i = \langle i | \hat{\varepsilon} \cdot \hat{d} | 3 \rangle \mathcal{E}_i(r, t), \quad i \in \{1, 2\}.$$

Additionally, we term $\delta = \delta_1 - \delta_2$ the *two-photon detuning* and $\Delta = \delta_1$ the *Raman detuning*.

In the specific case where the two driving fields are in the far-detuned limit and tuned to two-photon resonance, i.e. $\delta_i \gg \Omega_i$ and $\delta = 0$, the excited state population can be adiabatically eliminated.

nated and the system admits effective two-level dynamics given by,

$$\mathcal{H}_{\text{eff}}/\hbar = \frac{|\Omega_1|^2}{\Delta} |1\rangle\langle 1| + \frac{|\Omega_2|^2}{\Delta} |2\rangle\langle 2| + \left(\frac{\Omega_1^* \Omega_2}{\Delta} |1\rangle\langle 2| + \text{h.c.} \right) \quad (1.11)$$

In general, the effective coupling $\Omega_{\text{eff}} = \Omega_1^* \Omega_2 / \Delta$ between the ground states $|1\rangle$ and $|2\rangle$ is complex.

The complex phase of the coupling is given by the phase of the Raman fields at the location of the atom through

$$\Omega_{\text{eff}} \sim \mathcal{E}_1^*(r, t) \cdot \mathcal{E}_2(r, t).$$

In addition to coupling the ground states, the two-photon Raman process effectively imprints the phase of the light field onto the atom.

A similar Λ -type system can emerge in a tilted doublewell system. Consider a doublewell with sites $|L\rangle$ and $|R\rangle$ and a tunnel coupling J . If these two sites are detuned by an energy $\hbar\Delta_{\text{tilt}}$ where $\hbar\Delta_{\text{tilt}} \gg J$, tunneling between the sites is suppressed. Effective two-level dynamics are restored in the presence of Raman beams with a difference frequency $\Delta\nu = |\nu_1 - \nu_2|$ that matches the detuning Δ_{tilt} . As it was for the three-level atom discussed previously, the effective coupling between $|L\rangle$ and $|R\rangle$ is in general complex and thus tunneling between the sites is accompanied by a complex phase.

1.3.2 MINIMUM DIMENSION FOR ARTIFICIAL GAUGE FIELDS

While the use of laser-assisted tunneling leads to complex-valued tunnelings in the doublewell Hamiltonian, it does not lead to physically observable differences for single-atom experiments. The

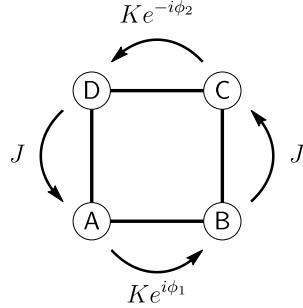


Figure 1.6: For the Harper-Hofstadter studies in this thesis, we consider a lattice system with complex-valued and real-valued tunneling matrix elements in the horizontal and vertical directions, respectively. In order to observe effects of the magnetic field, the system must contain at least two dimensions.

laser-assisted coupling can be written as $\Omega_{\text{eff}} = K e^{i\phi}$, where $K \in \mathbb{R}$. If we switch to a basis defined by,

$$|L\rangle = |\tilde{L}\rangle, \quad |R\rangle = |\tilde{L}\rangle e^{-i\phi},$$

the effective Hamiltonian will have completely real tunnelings,

$$\mathcal{H}_{\text{eff}}/\hbar = \frac{|\Omega_1|^2}{\Delta} |\tilde{L}\rangle\langle\tilde{L}| + \frac{|\Omega_2|^2}{\Delta} |\tilde{R}\rangle\langle\tilde{R}| + K \left(|\tilde{L}\rangle\langle\tilde{R}| + |\tilde{R}\rangle\langle\tilde{L}| \right). \quad (1.12)$$

In general, rotating nearest-neighbor tunneling terms in the complex plane does not result in physically observable changes for one-dimensional systems. [CHECK WITH FABIAN]. In contrast, consider the 2×2 system shown in Figure 1.6. Using the same trick described above, we can make the coupling between $|A\rangle$ and $|B\rangle$ completely real by defining $|B\rangle = |\tilde{B}\rangle e^{-i\phi_1}$. In order to keep the tunneling between $|B\rangle$ and $|C\rangle$ completely real, $|C\rangle$ needs to also be redefined $|C\rangle = |\tilde{C}\rangle e^{-i\phi_1}$. Continuing from site C to D and site D back to A, we would need to define $|D\rangle = |\tilde{D}\rangle e^{-i(\phi_1 - \phi_2)}$

and $|\mathbf{A}\rangle = |\tilde{\mathbf{A}}\rangle e^{-i(\phi_1 - \phi_2)}$, respectively. However, this redefinition must be consistent with the originally defined $|\tilde{1}\rangle$, which is true if and only if $(\phi_1 - \phi_2)/(2\pi) \in \mathbb{Z}$ and hence will not be true for arbitrary ϕ_1 and ϕ_2 . In section §5.2, we will re-encounter the fact that the vector potential does not have physically observable effects in 1D when we develop the band structure of the Harper-Hofstadter model in a $2 \times N$ ladder geometry. Physically, we can also understand this requirement to be in at least two dimensions from the Aharonov-Bohm phase. In lower dimensions, there is no notion of enclosing any magnetic flux.

1.3.3 RUNNING LATTICE

We extend the doublewell example to a 2D real-space lattice. For this extended system, we must consider the spatial structure of the Raman beams. Here, we consider the experimentally relevant case of an optical lattice in the xy plane with a potential gradient along the x direction that causes an energy difference between nearest neighbor sites of $\hbar\Delta_{\text{tilt}}$. The two Raman fields can be written out explicitly as

$$\mathbf{E}_R^i(\vec{r}, t) = \vec{E}_0^i \cos(\vec{k}_i \cdot \vec{r} - \omega_i t),$$

for $i \in \{1, 2\}$, leading to an intensity distribution

$$\begin{aligned} I(\vec{r}, t) &= |\mathbf{E}_R^1(\vec{r}, t) + \mathbf{E}_R^2(\vec{r}, t)|^2 \\ I(\vec{r}t) &= |\vec{E}_0^1|^2 \cos^2(\omega_1 t - \vec{k}_1 \cdot \vec{r}) + |\vec{E}_0^2|^2 \cos^2(\omega_2 t - \vec{k}_2 \cdot \vec{r}) \\ &\quad + \vec{E}_0^1 \cdot \vec{E}_0^2 [\cos(\Sigma\omega t - \Sigma\vec{k} \cdot \vec{r}) + \cos(\delta\omega t - \delta\vec{k} \cdot \vec{r})], \end{aligned}$$

where $\Sigma\omega = \omega_1 + \omega_2$ and $\delta\omega = \omega_1 - \omega_2$ with the likewise relations for $\Sigma\vec{k}$ and $\delta\vec{k}$. If we temporally average the fast timescales and set the field amplitudes to be identical, we find that the intensity distribution is that of a running lattice with phase velocity $\delta\omega/\delta\vec{k}$,

$$I(\vec{r}, t) = I_{\text{mod}}(1 + \cos(\delta\omega t - \delta\vec{k} \cdot \vec{r})), \quad I_{\text{mod}} \equiv |E_0|^2.$$

This running lattice adds a time-dependent distortion to the static 2D optical lattice, changing the shape of lattice sites and modifying the bare tunneling between nearest neighbors. However, for weak modulations, we can ignore these short length scale effects and treat the running lattice as only a modulation of the zero-point energy on each lattice site. In this approximation, each site is modulated at frequency $\delta\omega$ with an amplitude of V_{mod} . The phase of this modulation is described by

$$\phi_{m,n} \equiv \delta\vec{k} \cdot \vec{r}_{m,n} = m\phi_x + n\phi_y,$$

where $r_{m,n}$ is the location of site (m, n) , $\phi_x = \delta k_x a$, and $\phi_y = \delta k_y a$. Formally, this approximation is represented by the Hamiltonian,

$$\begin{aligned} \mathcal{H}(t) &= \sum_{m,n} \left(-J_x \hat{a}_{m+1,n}^\dagger \hat{a}_{m,n} - J_y \hat{a}_{m,n+1}^\dagger \hat{a}_{m,n} + \text{h.c.} \right) \\ &\quad + \sum_{m,n} (V_{\text{mod}} \cos(\delta\omega t - \phi_{m,n}) + \hbar\Delta_{\text{tilt}} m) \hat{n}_{m,n} \end{aligned}$$

where we have removed the DC term that would have carried over from $I(\vec{r}, t)$. Each pair of nearest neighbor sites in the x direction is detuned by $\hbar\Delta_{\text{tilt}}$ and realizes the doublewell described in the previous section. Hence, tunneling in the x direction with a site dependent complex phase is induced by the Raman fields. Using Floquet theory (Section §3.4 of Reference⁴), it can be shown that this driving leads to a tunneling strength, K , of

$$K = J_x \mathcal{J}_1 \left[\frac{V_{\text{mod}}}{\hbar\Delta_{\text{tilt}}} \sin(\phi_x/2) \right]. \quad (1.13)$$

In the y direction, the resonance condition where the modulation frequency $\delta\omega$ matches the energy difference between nearest neighbors is not fulfilled since the gradient is only in the x direction. Instead, the modulation detunes the lattice sites, causing a reduction in the tunneling strength given by

$$J = J_y \mathcal{J}_0 \left[\frac{V_{\text{mod}}}{\hbar\Delta_{\text{tilt}}} \sin(\phi_y/2) \right].$$

Combining these two results gives a time-independent Hamiltonian,

$$\mathcal{H} = \sum_{m,n} \left(-K e^{-i\phi_{m,n}} \hat{a}_{m+1,n}^\dagger \hat{a}_{m,n} - J \hat{a}_{m,n+1}^\dagger \hat{a}_{m,n} + \text{h.c.} \right),$$

the celebrated Harper-Hofstadter Hamiltonian. Since the complex phase is only associated with the horizontal tunneling terms, the net flux acquired by a particle upon a counterclockwise circuit around a unit cell, Φ , is given by the Raman phase difference between adjacent rows, ϕ_y , i.e. Φ depends only upon the vertical projection of the running lattice wavevector δk . The Raman phase

difference between adjacent columns, ϕ_x , changes the strength of the laser-assisted tunneling and maximal tunneling is achieved for $\phi_x = \pi$.

*Hofstadter's Law: It always takes longer than you expect,
even when you take into account Hofstadter's Law.*

Douglas R. Hofstadter

2

Experimental Techniques

The technological bedrock of this thesis is quantum gas microscopy. In the Greiner and other labs around the world, this experimental platform has demonstrated remarkable utility for the fields of quantum simulation and many-body physics. Experiments utilizing quantum gas microscopes have studied such wide-ranging phenomena as the onset of long-range order in the Fermi-Hubbard model, formation of bound magnons, and thermalization in isolated systems. To this versatile plat-

form, we introduce the ability to simulate gauge fields, equipping this apparatus for the study of topological physics. In this chapter, we review the essentials of quantum gas microscopy as realized in this apparatus, discuss our scheme for realizing a tunable artificial gauge field based upon laser-assisted tunneling techniques, and finally document a robust, user-friendly instrumentation control system geared towards orchestrating atomic physics experiments.

2.1 QUANTUM GAS MICROSCOPY

The idea behind quantum gas microscopy¹¹ is to employ high-resolution imaging systems in the service of quantum simulation with ultracold atoms in optical lattices. While this merger takes two very complicated and highly technical disciplines and does not make either any easier, the combined apparatus has many unique capabilities that make it a useful platform for studying a variety of physics. The quantum gas microscope used for the experiments in this work has been detailed extensively in both papers¹¹ and theses^{61,78,10}. We detail only the essentials and refer the reader to more detailed descriptions when appropriate.

2.1.1 OPTICAL LATTICES

The physics of our system occurs within a single xy -plane. In this plane, a 2D optical lattice provides regular confinement. To restrict physics to this 2D plane, we use a 1D optical lattice in the z -direction and work in a single site of this lattice.

IMAGED LATTICES IN THE xy -PLANE

The optical lattices in the xy -plane of our system are created by imaging a hologram. For each axis of our 2D lattice, x and y , there is a holographic mask with alternating 0 and π phase shift stripes.

Although the hologram imprints a phase pattern and not an intensity pattern on the beam, higher diffraction orders are eliminated by the finite numerical aperture resulting in a sinusoidal intensity pattern in the atom plane. This sinusoidal intensity pattern has a periodicity of $a = 680$ nm in both the \mathbf{e}_x and \mathbf{e}_y directions.

STANDING WAVE LATTICE IN THE z -DIRECTION

The 1D lattice in the z -direction is created using standing wave interference. The final optical element in our imaging system is a hemispherical lens. The vertical lattices are created by reflecting off this surface. The spacing of the resulting lattice is determined by both the wavelength of the light and the angle at which the laser reflects off the hemispherical lens. In our system, we have two beams that reflect off the hemispherical lens, allowing us to achieve vertical lattice spacings of $10\ \mu\text{m}$ and $1.5\ \mu\text{m}$.

SPECTRALLY BROAD LIGHT

The light used for each of these axes is derived from spectrally broad light derived from an EXALOS SLED that is amplified using Eagleyard tapered amplifiers. The spectrum is centered at 755 nm with a spectral width of approximately 3 nm, far-detuned from the Rb⁸⁷ D1 and D2 transitions. This

light has a very short temporal coherence length and thus path lengths must be well matched in order to interfere. This is ensured for the two diffraction orders of a given lattice axis by the imaging system. However, diffraction orders of separate lattice axes do not interfere as the path lengths are not interferometrically matched. Thus, the resulting sinusoidal potentials add incoherently as described in §1.1. A related consequence of using temporally incoherent light is that stray reflections that intersect with our region of interest will in most cases add incoherently rather than coherently with the desired optical potential since it is unlikely for a stray reflection to have a path length that is within a coherence length of the optical path length of the lattice beams.

SPATIAL FOURIER FILTERING

We employ another technique to reduce the optical disorder in our lattice beams. In the ideal case, the lattice beams appear as small spots in the Fourier plane of our imaging system. Most aberrations induced by, for example, dust or scratches on optics manifest as stray light at other locations in Fourier plane. The use of pinholes in the Fourier plane can mitigate these effects. This technique is described in detail in §4.3 of Reference⁶¹

2.1.2 ULTRACOLD ATOMS

Our experiments are conducted with a Bose-Einstein condensate (BEC)^{28,9} of Rb⁸⁷ in the $|F = 1, m_F = -1\rangle$ state created using standard techniques. We begin by loading a magneto-optical trap (MOT)^{69,81} from background atomic vapor for 6 s . Following polarization gradient²⁷, we have cold gas of $\sim 10^9$ Rb⁸⁷ atoms at approximately 40 μK . This cold gas of atoms is magnetically transported³⁶ from the

MOT chamber into a glass cell that serves as our science chamber. Magnetic transport allows us to separate the low vacuum region suited for fast loading of the MOT and a science chamber at UHV (~ 40 s atom lifetime). In addition, a separate science chamber allows for ample optical access. In the science chamber, the atoms undergo forced RF evaporation in a QUIC trap. Following ≈ 25 s of evaporation, we obtain a BEC of $\sim 10^5$ atoms.

This BEC is pushed vertically to a location $10 \mu\text{m}$ below the surface of the hemispherical lens where it is loaded into the first node of the $10 \mu\text{m}$ -spacing vertical lattice. We increase the depth of this lattice to compress the cloud into a pancake after which we transfer to the sixth node of the $1.5 \mu\text{m}$ -spacing vertical lattice. Following these two stages, the BEC is in a single xy -plane, harmonically trapped in the vertical direction with a trap frequency $\omega_z \approx 2\pi \times 8 \text{ kHz}$.

From this pancake of atoms, we turn on a tightly focused dipole beam, i.e. a dimple beam, to select out atoms in the center of the cloud. By turning off the magnetic trap, we expel the atoms not trapped by the dimple. By adjusting the power in this beam, we can vary the number of retained atoms. In addition, this beam allows us to select the coldest atoms in the cloud and in general represents the last cooling step in our preparation.

Following the dimple, the atoms are adiabatically loaded into a large harmonic trap with trap frequencies in the range of $10 - 20 \text{ Hz}$. From here, the atoms are loaded into the conservative 2D lattices described earlier. Following an adiabatic ramp, the superfluid state is transferred to a Mott insulator with uniform filling. We are able to achieve fillings of up to 99% on individual sites and in the 95 – 98% range for the extended regions of ≈ 10 sites.

2.2 TUNABLE ARTIFICIAL GAUGE FIELDS

Although laser-assisted tunneling for the generation of synthetic gauge fields^{50,54} has been demonstrated in many groups utilizing both real-space^{6,68} and synthetic lattices^{92,64}, these experiments have thus far not been able to realize a magnetic field that can be readily varied. By combining Raman techniques with our quantum gas microscope, we realize a platform that allows us to dynamically tune the effective magnetic field from the weak to strong field limits within a single experiment, without having to change the laser wavelengths.

In accordance with the discussion in the previous chapter, a potential gradient must be applied to the lattice to detune nearest neighbor bare tunneling as well as to allow for the use of two-photon Raman transitions. We achieve an energy offset of $\Delta_{\text{tilt}} \approx 2\pi \times 870 \text{ Hz}$ between nearest neighbors along the x -direction using a magnetic field gradient. This gradient effectively suppresses the tunneling of $J_x/\hbar \approx 2\pi \times 100 \text{ Hz}$ associated with the lattice depth of $V_x = 4E_r$ used in our experiments. This gradient is provided by running current through our Ioffe coil.

The configuration of our Raman beams is shown in Figure 2.1. The two fields are derived from an EXALOS SLED source centered at $\lambda_{\text{SLED}} \approx 755 \text{ nm}$ and spectrally narrowed to a FWHM of $\approx 3 \text{ nm}$ using interference filters. Because the light source is spectrally broad, the path lengths for the two Raman beams must be matched well to ensure full interference contrast in the image plane. In the Raman 1 beam path, there is a delay line with a mirror on a one-axis stage that allows us to tune the length of the delay using a micrometer.

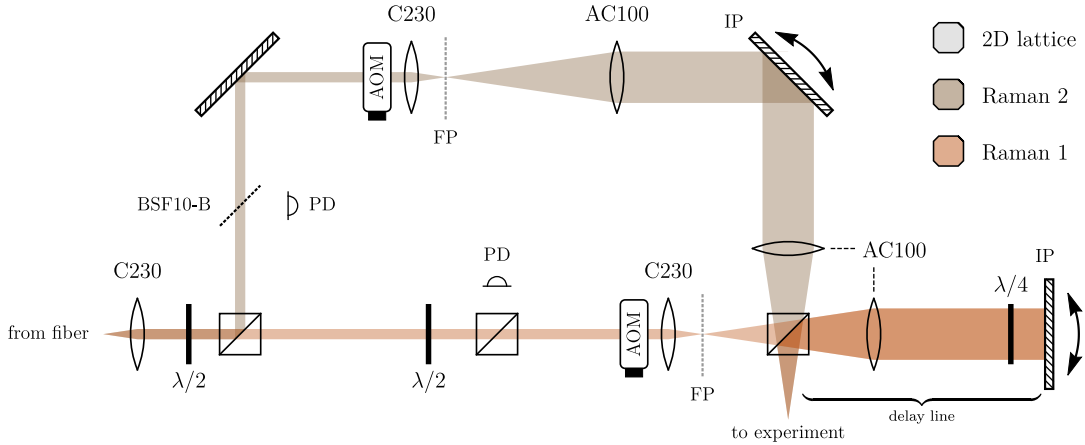


Figure 2.1: Optical layout of the Raman fields for a tunable artificial gauge field: The Raman fields are sourced from a broadband SLED source. They are independently frequency-shifted by two acousto-optic modulators (AOM) to achieve the necessary relative detuning. The angular deflection caused by the AOMs is not shown. Because of the broadband nature of the light, the optical path lengths of the two paths are matched with a delay line to ensure interference in the image. Piezo-mounted mirror in intermediate image planes on both arms allow for the effective magnetic field strength to be tuned.

To control the beat frequency, $\Delta\nu = \nu_2 - \nu_1$, between the two Raman fields at frequency* ν_1 and ν_2 , each beam is passed through an acousto-optic modulator (AOM) with phase-locked RF tones. The RF circuit used to generate the tones is shown in Figure 2.2. The first RF tone is derived from a CRYSTEK CVC055CL-0060-0110 voltage-controlled oscillator (VCO) locked to $f_{\text{PLL}} = 80 \text{ MHz}$ by an ANALOG DEVICES ADF4002 PLL chip†. The second RF tone comes from an AGILENT E3300B signal generator running in FM mode wherein the output frequency is controlled via an analog voltage V_{FM} . In this mode, the output frequency is given by $f_{\text{E3300B}} = 80 \text{ MHz} + \delta f_{\text{FM}}(V_{\text{FM}})$ where the voltage $V_{\text{FM}} \in [-1 \text{ V}, 1 \text{ V}]$ modulates $\delta f_{\text{FM}}(V)$ over the inter-

*Unlike in §1.3.1, we define these frequencies in Hertz, rather than angular frequencies, i.e. rad/s.

†In some sense, the VCO is not locked to 80 MHz, but instead to some multiple of the frequency on the reference port of the ADF4002. As configured, the reference signal is 10 MHz and the ADF4002 locks the VCO to eight times that frequency, thus achieving 80 MHz.

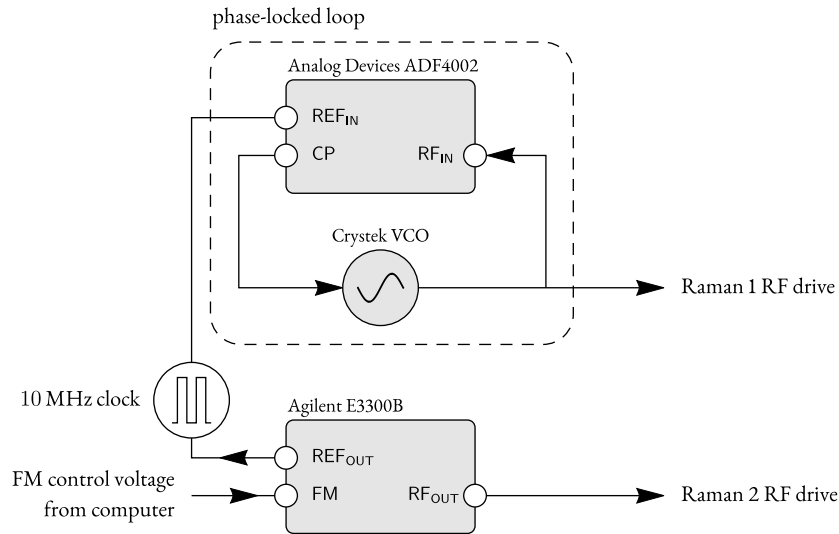


Figure 2.2: RF circuit for Raman field acousto-optic modulators: The RF fields driving the frequency-shifting AOMs in Figure 2.1 are generated from an Agilent E3300B signal generator and a VCO that is phase-locked to a 10 MHz reference signal from the Agilent.

val $[-1 \text{ kHz}, 1 \text{ kHz}]$. In order to drive two-photon Raman transitions, these two RF tones must be phase coherent and to this end, the ADF4002 uses a 10 MHz reference signal generated by the AGILENT E3300B signal generator. Following the AOMs, the Raman frequencies are then

$$\left. \begin{aligned} \nu_1 &= \nu + f_{\text{PLL}} = \nu + 80 \text{ MHz} \\ \nu_2 &= \nu + f_{\text{E3300B}} = \nu + 80 \text{ MHz} + \delta f_{\text{FM}}(V_{\text{FM}}) \end{aligned} \right\} \Rightarrow \Delta\nu = \delta f(V_{\text{FM}}),$$

allowing us to tune the Raman beat frequency with an analog voltage.

The phase between the two RF tones affects the phase of the Raman beams on the atoms. This phase is not identical between experiments since the RF sources are not triggered on every experi-

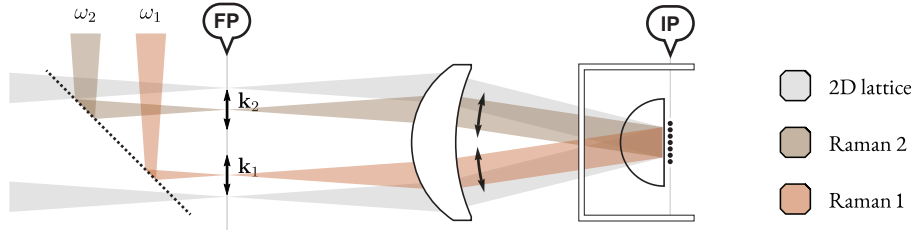


Figure 2.3: The Raman and lattice fields are imaged through a common objective. They share a common Fourier plane with which the flux can be calibrated. Translating the Raman beam in the Fourier plane leads to a shift in the angle at which the Raman fields intersect with the image plane.

ment and instead are free running. While it is possible to achieve a consistent relative RF phase[‡], the relative optical path length between the two Raman beams must *also* be stabilized in order to ensure a reproducible Raman lattice phase in the atom plane. This path length must be interferometrically stable, i.e. to within a wavelength. In our parameter regime where $h\Delta\nu \gg J, K$, this phase variation is quickly averaged out and irrelevant to the dynamics we observe.

Following the optical setup shown in Figure 2.1, the Raman beams are imaged onto the 2D plane of the atoms. This imaging system is shared with the static, Bose-Hubbard lattice and hence there is a common Fourier plane as shown in Figure 2.3. In this plane lies a thin, glass correction plate used for reducing aberrations in our imaging system. Scatter from this plane can be conveniently used for imaging the light fields in the Fourier plane which is one method we use for calibrating the flux per plaquette in our system.

A schematic representation of this intermediate Fourier plane is shown in Figure 2.4. Here, the

[‡]This would involve using two phase-locked reference signals derived from a direct digital synthesizer (DDS). The DDS signals would act as references for a pair of PLL chips to frequency lock narrowband VCOs. Changing the Raman beat frequency would involve programming one of the two DDS's to output a different frequency. The key advantage here with DDS technology is the option to clear phase accumulator, which would need to be done on both DDS's prior to the experiment to achieve a consistent RF phase.

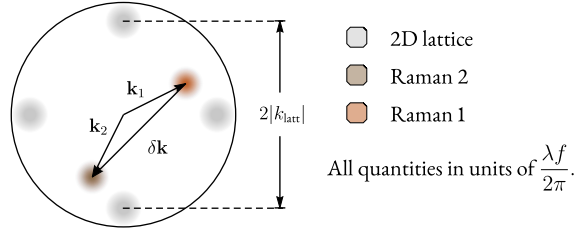


Figure 2.4: Raman and lattice field in a shared Fourier plane: The Raman fields appear as a pair of spots in the shared Fourier plane. The vector connecting these two spots is proportional to the wavevector of the Raman lattice. The vertical (horizontal) separation of the beams affects the flux per plaquette (tunneling strength). The spatial separation between the lattice beams is proportional to the lattice wavevector.

Bose-Hubbard lattice appears as four spots[§] located at a radius of $k_{\text{latt}} f / k_{\text{laser}} = f \sin(\theta_{\text{NA}})$ along the $\pm \mathbf{e}_x$ and $\pm \mathbf{e}_y$ directions, where $f = 12.1$ mm for our objective. As described in the previous chapter, the Raman beams also interfere to form a lattice and so, in the Fourier plane, this results in two spots within the radius set by the lattice beams located at $\mathbf{k}_1 f / k_{\text{laser}}$ and $\mathbf{k}_2 f / k_{\text{laser}}$. The wavevector associated with the Raman lattice is given by the difference between the two individual Raman wavevectors, i.e. $\delta\mathbf{k} = \mathbf{k}_1 - \mathbf{k}_2$. This wavevector is directly related to the vector connecting the two Raman beams in the Fourier plane.

The horizontal separation of these beams, $\delta\mathbf{k} \cdot \mathbf{e}_x$, gives rise to the horizontal component of the Raman lattice's phase velocity. To maximize the tunnel coupling for a given modulation depth of the Raman lattice (See Equation 1.13), we position the beams such that $\delta\mathbf{k} \cdot a\mathbf{e}_x = \phi_x = \pi$. In this case, the wavelength in the horizontal direction is twice that of the lattice spacing a and the horizontal separation of the Raman beams is half that of the lattice beams.

The vertical separation of the Raman beams determines the phase difference between one row of

[§]The Bose-Hubbard lattice consists of two independent lattices, each of which has a field proportional to $\cos(kx_i) \propto e^{ikx_i} + e^{-ikx_i}$, where $x_i \in \{x, y\}$.

the running lattice and the next, $\phi_y = \delta\mathbf{k} \cdot a\mathbf{e}_y$. As discussed in the previous section, this phase difference gives rise to the flux per plaquette in our system. Hence, we can tune the effective magnetic field strength by adjusting the vertical separation of the Raman beams.

To translate the Raman beams in the Fourier plane and adjust either the flux and/or the laser-assisted tunneling strength, we use piezo-actuated mirrors (THORLABS POLARIS K1PZ mounts) located in the intermediate image plane shown in Figure 2.1. These mirrors adjust the angle of the beams in the image plane, which manifests as a change in position in the Fourier plane. To calculate the flux range we can achieve with this scheme, it is possible and perhaps easier to think in terms of adding fringes to the Raman beam in the image plane rather than displacements in the Fourier plane. The $\approx 500 \mu\text{rad}$ angular deviation of the K1PZ mount and the $\approx 30 \text{ mm}$ beam size on the mirror results in being able to vary the number of interference fringes by

$$\frac{500 \mu\text{rad} \times 30 \text{ mm}}{755 \text{ nm/fringe}} \approx 20 \text{ fringes.}$$

There is a de-magnification of ≈ 500 from the image plane on the piezo-actuated mirror to the atom plane, resulting in a final beam size of ≈ 90 sites. A variation of ≈ 20 fringes per piezo-actuated mirror means a total variation of ≈ 40 fringes over ≈ 90 sites, corresponding to a tuning range for ϕ_x or ϕ_y of $\frac{40}{90} \times 2\pi \approx \pi \text{ rad}$.

The flux can also be adjusted by flipping the sign of the relative detuning between the Raman beams. To drive laser-assisted tunneling, it is only the magnitude of the relative detuning, $2\pi \times |\Delta\nu|$, that must match the frequency offset, Δ_{tilt} . Hence, the sign of $\Delta\nu$ can be reversed, reversing the

phase velocity or effectively reversing the progression of time. In this case, if a given row had previously been lagging its neighboring row by a phase ϕ_y , it would now be leading its neighboring row by a phase ϕ_y , effectively reversing the sign of the flux or equivalently the magnetic field. Reversing the sign of the relative detuning can be achieved by changing the RF drive into Raman 2 from $80 \text{ MHz} + \Delta_{\text{tilt}}/(2\pi)$ to $80 \text{ MHz} - \Delta_{\text{tilt}}/(2\pi)$, which is possible through tuning V_{FM} . When the range of fluxes achievable through translating in the Fourier plane is added, we have the ability to adjust the flux $\Phi = \phi_y$ across almost the full relevant interval, $[-\pi, \pi]$.

As a final note, we note that the number of fringes we can add to the beam through the piezo-actuated mirrors is fixed by the throw of the piezos, which is somewhat fundamentally limited. Without departing from piezo-actuated mirrors, it is possible to increase the flux range by increasing the demagnification so that the number of sites over which the number of fringes can vary is decreased. Alternatively, one could use galvanometer-mounted mirrors rather than piezo-actuated mirrors to achieve a larger range for the number of fringes.

2.2.1 RESONANCE CALIBRATION

In order to drive laser-assisted tunneling, the relative frequency $2\pi \times \Delta\nu$ and the offset frequency Δ_{tilt} between neighboring lattice sites must match. In our system, we meet this condition by tuning the beat frequency and keeping the offset frequency fixed. For a coarse calibration, we look for a resonance feature in the bulk:

1. Create a large $n = 1$ Mott insulator.
2. Ramp on a magnetic field gradient to tilt the optical lattice in the \mathbf{e}_x direction.

3. Ramp down the lattice in the \mathbf{e}_x direction.
4. Illuminate with Raman beams at a given beat frequency.
5. Image site occupation.

In the tilted lattice, tunneling is suppressed in spite of the low lattice depth. When the beat frequency is on resonance with the energy offset, the laser-assisted tunneling couples neighboring lattice sites. Due to the uniform filling of the Mott state, atoms must not only overcome the energy offset, but also the interaction energy of having two atoms on the same site. Hence, we expect resonance features at $\hbar\Delta_{\text{tilt}} + U$ and $\hbar\Delta_{\text{tilt}} - U$ in the site occupations. On resonance, we expect tunneling to drive the formation of doubly- and non- occupied sites, which are evident when probing the parity of site occupations, p_{odd} . In Figure 2.5 we plot this quantity as a function of the beat frequency $\Delta\nu$, which exhibits the $\hbar\Delta\nu = \hbar\Delta_{\text{tilt}} + U$ and $\hbar\Delta\nu = \hbar\Delta_{\text{tilt}} - U$ resonance features. The average of these two peak locations gives Δ_{tilt} which indicates the value of $\Delta\nu$ needed for resonant tunneling. These measurements also provide a means to calibrate the control voltage for the magnetic field. In Figure 2.6, we focus on the $\hbar\Delta\nu = \hbar\Delta_{\text{tilt}} - U$ peak and plot the spectrum obtained at various magnetic field strengths. The variation of the peak location with the control voltage, along with the fixed point obtained from the average of the peaks in Figure 2.5, is sufficient to characterize our magnetic field gradient.

The resonance features from these bulk measurements are susceptible to inhomogeneous broadening caused by local disorder in the lattice potential. To minimize these effects, we probe the system with a single line of atoms. This experiment is the same as the bulk experiment listed above, except that after the Mott insulator is formed (between steps 1 and 2), we use our DMD to cut out a

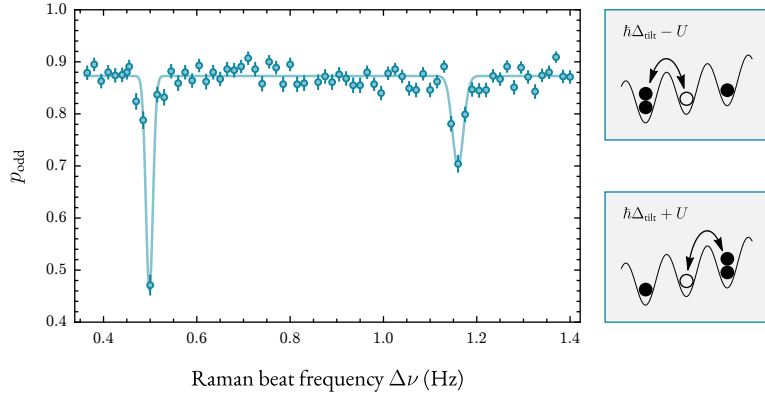


Figure 2.5: Raman resonance scan in a bulk Mott insulator: Scanning the Raman beat frequency in the bulk leads to two resonance features at $\hbar\Delta_{\text{tilt}} \pm U$ corresponding to the processes shown in the panels on the right.

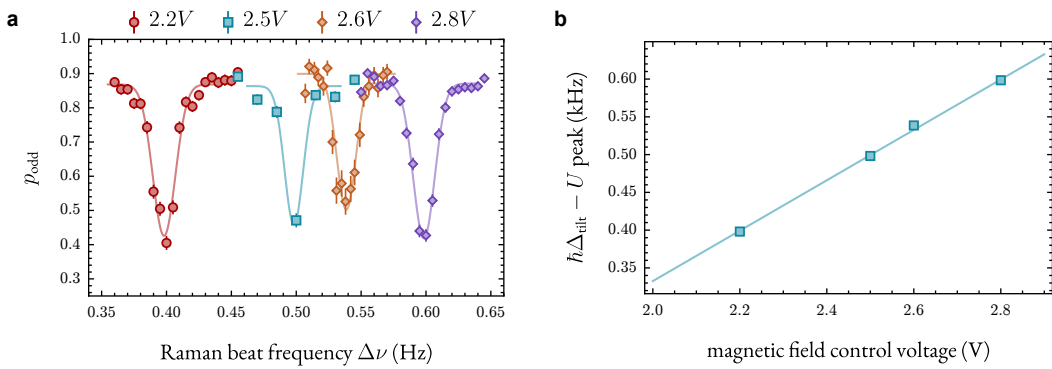


Figure 2.6: Tilt calibration using $\Delta_{\text{tilt}} - U$ bulk resonance feature: The location of the $\hbar\Delta_{\text{tilt}} - U$ resonance feature allows us to calibrate the control voltage for the magnetic field gradient that tilts the optical lattice potential

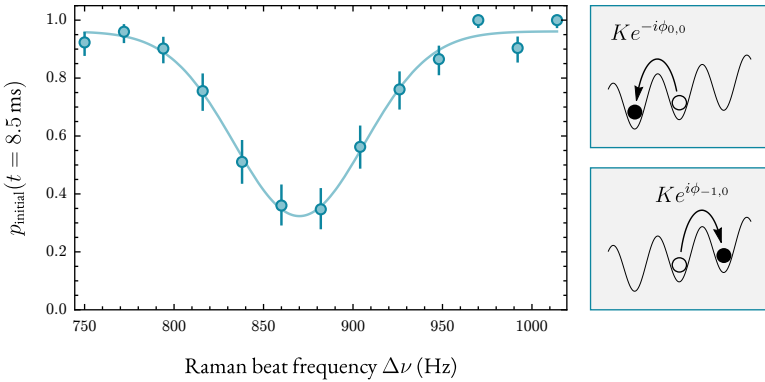


Figure 2.7: Site-resolved Raman resonance scan: By scanning the Raman relative detuning in a system with a single line of atoms, we can directly observe the Δ_{tilt} and mitigate effects of local disorder. Plotted is the occupation of the initial site in a tilted lattice after $t = 8.5$ ms of evolution plotted against the relative detuning of the Raman beams.

single line of atoms in the \mathbf{e}_y direction.

Unlike the bulk measurements, the resonance features are not shifted by the interaction energy U because the high lattice depth in the \mathbf{e}_y direction prevents atoms from interacting with atoms in neighboring rows (horizontal tubes). On resonance, coupling between nearest neighbors in each column is restored, causing the initially localized atom to perform a quantum walk outwards and decreasing the occupation of the original site. In Figure 2.7, we plot this occupation following an evolution time of $t = 8.5$ ms as a function of the beat frequency of the two beams. The detuning where the site occupation is minimal corresponds to the point where resonant tunneling is restored. For more precise measurements, we can restrict the number of columns over which we average. For the quantum walk experiments shown in Chapter 5, the resonance was calibrated using 3 rows and found to be located at $\Delta\nu \approx 870$ Hz, which is the minimum of a Gaussian fit to the data.

For these calibrations, there are a few important considerations.

EVOLUTION TIME For a tunneling rate of K , the occupation of the initial site, p_{initial} , following an evolution time of t is given by⁴²

$$p_{\text{initial}}(t) = \left| \mathcal{J}_0 \left(\frac{4K}{h\delta} \sin(\pi\delta t) \right) \right|^2,$$

where $h\delta = \hbar\Delta_{\text{tilt}} - h\Delta\nu$ is the detuning from resonance of the Raman beat frequency. This equation is only monotonic for small times t . Hence, it is important that the evolution time is restricted to early times to avoid non-linear broadening effects, $t \ll \hbar/(2K)$.

HIGH POWERS The laser-assisted tunneling strength increases with the modulation depth of the Raman lattice. However, it is important to stay in the regime where the Floquet approximation, Equation 1.13, is valid. We require that J_x , the bare tunneling, and K , the restored tunneling, are both much smaller than the tilt per site $\hbar\Delta_{\text{tilt}}$. In the phasor picture discussed earlier, population in the neighboring site tunnels to the next nearest neighbor before enough cycles have occurred on the neighboring site to cause the phasor sum to vanish when the drive is off-resonant. In addition to these broadening effects, harmonics appear at factors of the resonance frequency. We observe signatures of these effects in Figure 2.8a. We include a simulation which shows similar features in b.

2.2.2 TUNNELING CALIBRATION

The quantum walk experiments in the previous section can also be used to calibrate the strength of the laser-assisted tunneling since the outward propagation rate depends only on this strength when

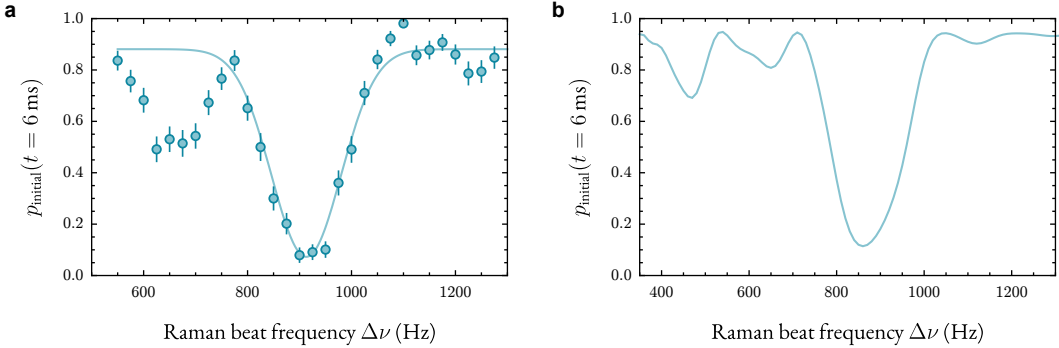


Figure 2.8: Raman Harmonics: **a** Raman resonance scan taken at high powers that exhibits peaks at harmonics of the tilt frequency $\Delta_{\text{tilt}}/(2\pi)$. **b** Simulated Raman resonance scan for modulation depth of $V_{\text{mod}}/(\hbar\Delta_{\text{tilt}}) = 0.5$, bare tunneling rate $J_x = 100$ Hz, and tilt per lattice site of $\Delta_{\text{tilt}} = 2\pi \times 880$ Hz. This simulation does not use the time-independent Hamiltonian given by Floquet theory, but instead treats the Raman driving as a time-dependent modulation of the zero-point energies on each site.

the Raman beams have been tuned into resonance. A single atom is initialized in a one-dimensional lattice along x at site $i = 0$ and the evolution of the density distribution is obtained (Figure 2.9a)⁷⁹. We expect the density distribution on site i to evolve according to⁴².

$$p_i(t) = \left| \mathcal{J}_i \left(\frac{4K}{h\delta} \sin(\pi\delta t) \right) \right|^2,$$

where \mathcal{J}_i is the i th Bessel function of the first kind. The theoretical density distribution is fitted to the data (Figure 2.9a), yielding $K/h = 11.4$ Hz. We also investigate the dependence of the tunneling rates on the power of the Raman beams by performing single-particle quantum walks along x and y for several Raman lattice depths. The resulting tunneling rates and fits of the expected dependence⁷ are shown in Figure 2.9.

For the experiments presented in Chapter 5, evolution is restricted to a $2 \times N$ ladder. The poten-

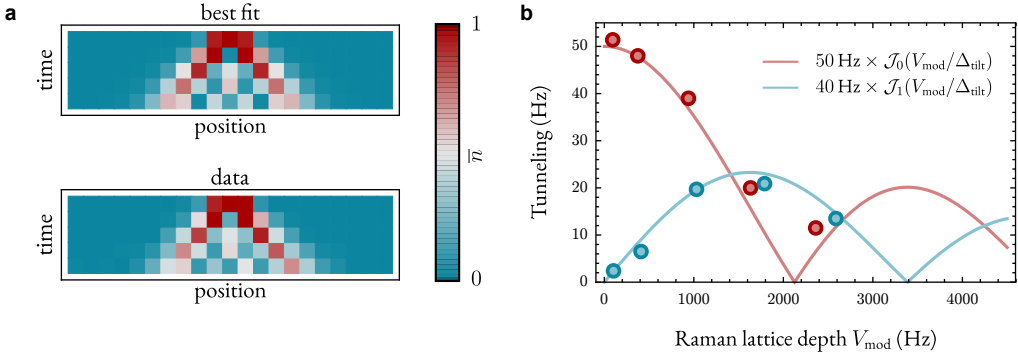


Figure 2.9: Restored and suppressed tunneling in a driven optical lattice: **a**, Quantum walk in a one-dimensional lattice along the leg dimension x . **b**, Dependence of the tunneling rates along x (blue) and y (red) on the gauge field power. Here, $\mathcal{J}_{0,1}$ are Bessel functions of the first kind. They are scaled by the bare tunneling strengths 40 Hz along x and 50 Hz along y that we measure in the absence of tilt and Raman lattice.

tial along the rungs, i.e. the short axis of the ladder, is modified by the confining potential derived from the DMD. To calibrate the tunneling J in this potential, we measure the the double-well oscillation frequency. We initialize an atom on one side of a double-well potential and measure its time evolution. The occupation number undergoes oscillations between the sites with frequency $2J$. We obtain the tunneling rate $J/h = 34$ Hz from a fit to the data.

2.2.3 HEATING RATES IN A RAMAN LATTICE

We estimate heating rates in our Raman lattice by measuring the atom number decay as a function of time for different fluxes Φ . Our experiments are performed on a time scale where this exponential decay is entirely dominated by its linear term, yielding

$$N(t) = N_0 \exp\left(-\frac{t}{t_0}\right) \approx N_0 - \frac{N_0}{t_0}t,$$

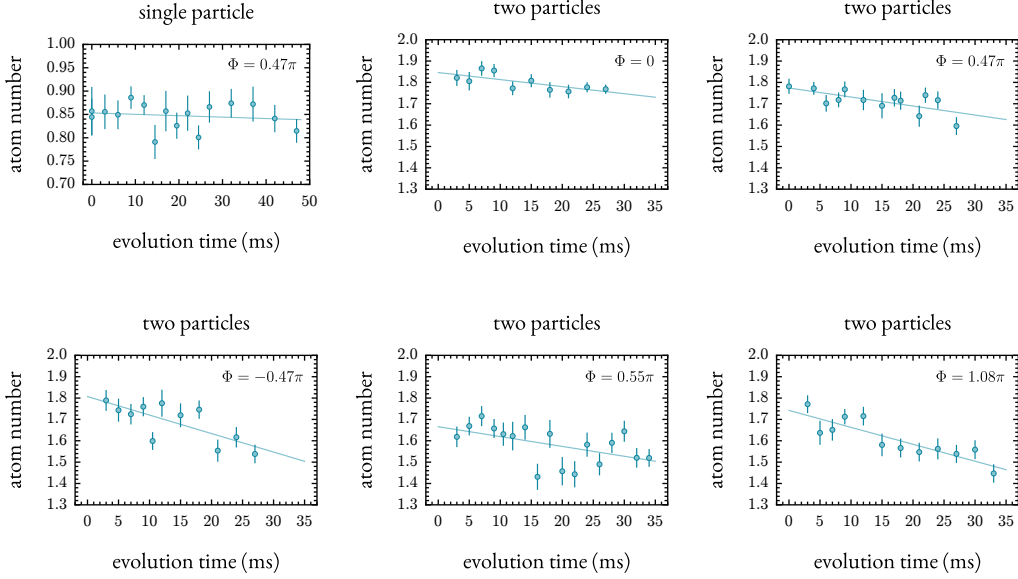


Figure 2.10: Heating rates from laser-assisted tunneling: Plotted is the average atom number as a function of time for different flux values and single- and two-particle experiments. For each set of parameters, the decay is fitted to a line which we interpret as the linear term in a power series expansion of an exponential atom number decay.

where N_0 and t_0 are the initial atom number and the $1/e$ decay time, respectively. Using these quantities as free parameters, we fit individual decay curves to our experimental data, the results of which are shown in Fig. 2.10.

Due to a variation of single-particle fidelities in the corresponding Mott insulators, the initial (average) atom number varies for different flux values Φ , but the subsequent decay of the population is given by the heating dynamics in the Raman lattice. For the single-particle case with $\Phi = \pi/3$, the fitted decay time scale can not be distinguished from our vacuum-limited lifetime within the statistical error. For the experiments with two interacting particles in the ladder, we can compare the case without Raman lattice ($\Phi = 0$) to the case with photon-assisted tunneling for flux values

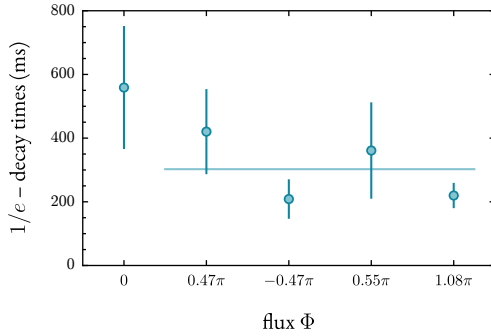


Figure 2.11: Atom number decay rates: The fitted decay rates for the five two-particle experiments plotted as a function of flux. Solid line is the average of decay rate for those cases where flux is non zero.

$\Phi = \pi/3, -\pi/3, \pi/2$ and π (cf. Fig. 2.11).

2.3 INSTRUMENTATION CONTROL

Optical lattice emulator experiments require a precise symphony of digital and analog signals. For our apparatus, this sequence is typically ~ 45 s in length while requiring millisecond or better timing accuracy for short durations (~ 2 s). The digital signals control, for example, shutters for blocking laser beams, MOSFETs for connecting coils to power supplies, switches for passing RF drives to acousto-optic modulators, and triggers for cameras. The analog signals are primarily used as set-points for the feedback loops that control the optical power of our various lasers, which typically have a 0.5 V/decade gain profile. A typical experiment requires 50–100 digital channels and 10–20 analog channels. Hardware control in our experiment is based on hybrid system of two Viewpoint DIO-64 digital I/O and two National Instruments PCIe-6536 high-speed digital I/O systems for digital and analog control, respectively.

DIGITAL CONTROL The Viewpoint DIO-64 cards provide 64 independent, digital output channels with a sample clock of 20 MHz. Digital pulses are easily defined via start and stop times. These signals are galvanically isolated using optocouplers before being utilized on the apparatus. At the time of writing, Viewpoint is now a part of National Instruments and the DIO-64 system is no longer available.

ANALOG CONTROL The National Instruments PCIe-6536 cards provide 32 independent, digital output channels with a sample clock of up to 25 MHz⁴. These digital outputs are used to program digital-to-analog converters, specifically the DAC9881 from Texas Instruments.

The following chapter focuses on our implementation of the PCIe-6536 for generating analog outputs. We discuss the DIO-64 system only in its interactions with the analog control system.

2.3.1 SERIAL COMMUNICATION

The DAC9881 digital-to-analog converters utilize a standard 4-wire SPI synchronous serial interface for communication. To program an analog voltage, a host device must send the appropriate digital waveforms on the CS, SCLK, and SDI channels of each client DAC9881. The CS channel signals to the DAC9881 that a serial command is incoming. The SDI channel is toggled high and low to indicate the value of the bit to be transferred. A rising edge on the SCLK channel triggers the device to probe the SDI channel to determine the bit value. The fourth connection on this 4-wire interface is the SDO channel.

⁴A sample clock of up to 50 MHz (10 MHz) is available with the PCIe-6537 (5).

is designed such that multiple DAC9881 devices can be daisy-chained with each device costing only one additional digital output from the host (rather than three). In our experiment, we do not implement daisy-chaining and the SDO channel is left unconnected.

2.3.2 CLOCK DISTRIBUTION WITH AD9522

INCREASING SCALABILITY In this system, each PCIe-6536 acts as an SPI host¹, generating the necessary serial commands to produce the desired analog voltage waveforms. If DAC9881 devices were directly connected to a PCIe-6536 host, each host would be limited to a maximum of $\lfloor \frac{32}{3} \rfloor = 10$ DAC9881 devices. In this case, each client device would have a dedicated digital output on its PCIe-6536 host for each of its CS, SCLK, and SDI digital inputs. To increase the capacity of each PCIe-6536 host in our implementation, the CS and SCLK lines are shared. One digital channel from each PCIe-6536 host is used as a reference signal for a AD9522 clock distribution chip associated to that PCIe-6536 host. The reference signal is connected to the port labeled REFIN on the datasheet². The AD9522 is configured to create 24 identical clock outputs, phase-locked to the reference clock from the PCIe-6536. Two DIO channels from each PCIe-6536 host are used as CS channels for that host's client devices. Each DIO channel used for this purpose is shared between 12 client devices. This reduces the per client channel usage and allows us to reach a maximum capacity of 24 DAC9881 clients per PCIe-6536 host. The DIO channels used for the reference signal connected to each AD9522, the two DIO channels used as shared CS channels, and the 24 DIO channels connected to the client SDI

¹In principle, the DIO-64 devices are capable of acting as a SPI host, however they have very limited memory and are not suited for this role.

inputs are listed in Table 2.2 and drawn schematically in Figure 2.12.

CLOCK DOUBLING In addition to multiplexing the high-speed clock signal, each AD9522 also serves the crucial function of doubling the frequency of the input reference clock. If f_{SMP_CLK} is the sample clock frequency of the clock signal to each PCIe-6536 host, then that PCIe-6536 could change digital values on each of its DIO outputs at a rate of at most f_{SMP_CLK} . Hence, the DIO output used as the reference for the AD9522 would be able to output a clock frequency of at most $f_{SMP_CLK}/2$. If this reference frequency were not doubled, then the digital waveform streamed to each client DAC9881 on its SDI channel would need to be restricted to at most $f_{SMP_CLK}/2$. To satisfy this condition, each bit generated by the PCIe-6536 host to SDI channels on client devices would have to be repeated to reduce the digital waveform data rate to $f_{SMP_CLK}/2$. With the AD9522, this inconvenience can be avoided. The AD9522 has a number of on-chip dividers that allow for the distributed clocks to be at a different frequency from the input reference signal. In our case, we choose the distributed clocks to have a frequency of f_{SMP_CLK} , i.e. double the frequency of the input reference signal at $f_{SMP_CLK}/2$. In Table 2.1, we compile the necessary values for the various dividers and counters on the AD9522 to achieve f_{SMP_CLK} on its outputs for f_{SMP_CLK} values of 12.5 MHz and 25 MHz.

2.3.3 MEMORY STRUCTURE

Whereas start/stop times define the digital waveforms for the DIO-64, a 1D array of 32-bit integers, which we name `NI_waveform`, defines the digital waveforms for all of the DIO channels on a given PCIe-6536. In Figure 2.13, we diagram how the analog voltage for a single unit of time is

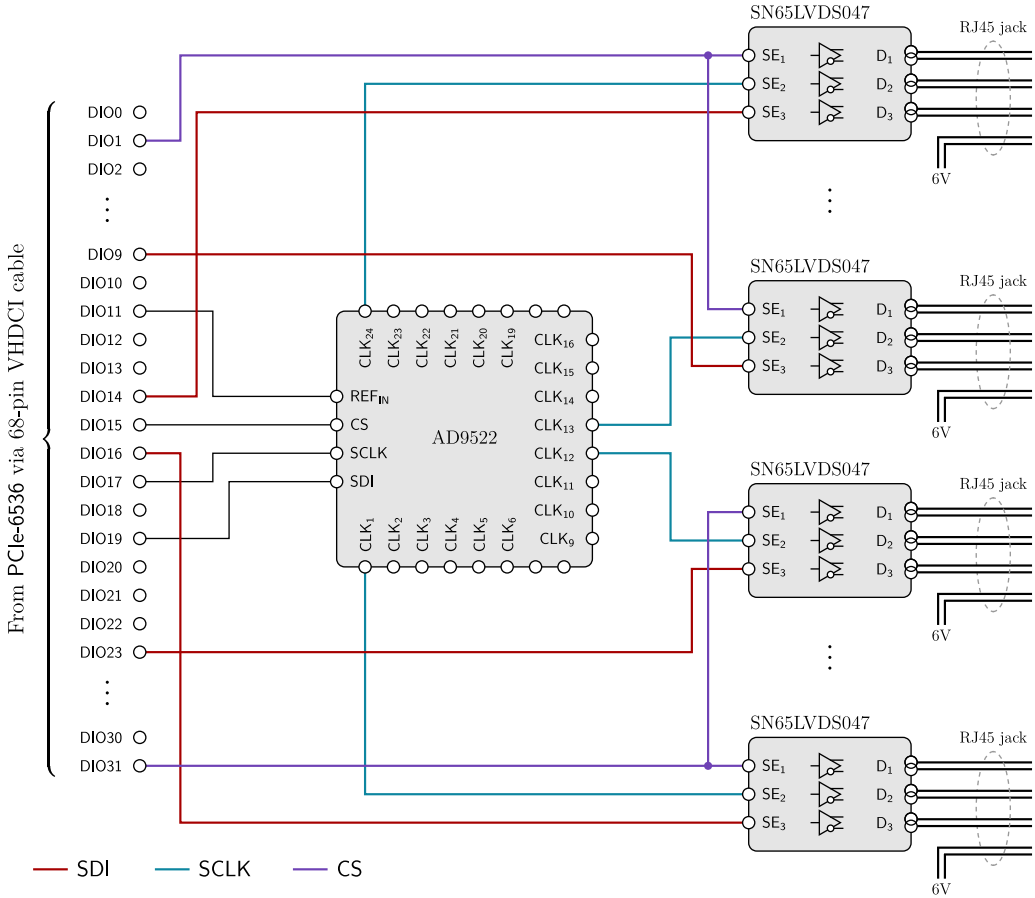


Figure 2.12: Combining the AD9522 with the PCIe-6536: In order to increase the scalability of the analog control system, we utilize an AD9522 clock distribution chip to duplicate a single DIO on the PCIe-6536, obviating the need to devote a DIO for every client device. In addition, the AD9522 allows us to double the reference clock from the PCIe-6536.

Device Configuration				
Setting	Value	Value	Units	Notes
Sample Rate	368	735	kHz	Update rate of analog voltages
f_{Agilent}	12.5	25	MHz	frequency of Agilent clock fed to the PCIe-6536
f_{REFIN}	6.25	12.5	MHz	Reference clock generated by PCIe-6536 which is then multiplied and distributed by the AD9522. Fixed by software to a maximum value of $f_{\text{Agilent}}/2$.
R divider	1	1		Reference clock is divided down by the R divider and then fed to the phase frequency detector (PFD)
f_{VCO}	2.4	2.55	GHz	Frequency of the on-chip VCO. According to the datasheet, this is limited to 2.530 to 2.5950, but 2.4 seems to work.
N divider				
P/P+1 prescalar	32	16		
B counter	12	12		
A counter	0	12		
f_{PFD}	6.25	12.5	MHz	The frequency fed to the PFD determines the recommended VCO Calibration Divider (See Table 30 of Reference ²).
VCO Calibration Divider	4	8		According to the datasheet ² , any value should work for $f_{\text{PFD}} = 6.25 \text{ MHz}$. In practice, 8 does not work, but 4 does.
VCO divider	6	6		
Channel Divider				
N counter	15	8		
M counter	15	7		
$f_{\text{CLK1..24}}$	12.5	25	MHz	
clock doubler	off	off		Clock doubler does not seem to work (no reason given, but disabled based upon suggestion from an AD engineer)

Table 2.1: AD9522 Configuration This table details the settings needed for Agilent E33250A and the AD9522 to support 368 kHz and 735 kHz analog update rate operation. 57

programmed. Each programming voltage instruction to the DAC9881 host devices requires 34 sample clock cycles, i.e. a 34-bit word, in our implementation^{**}. Hence, the analog update rate of our control system is $f_{SMP_CLK}/34$, which is approximately 368 kHz for the current configuration of $f_{SMP_CLK} = 12.5$ MHz, corresponding to a time step of approximately $3 \mu\text{s}$. In the first step, the desired voltage for channel n at t_0 , $V_n(t_0)$, is converted into a digital word, $V_n^B(t_0)$, approximating the analog value to 18-bit precision. Associated with the analog values of all the DAC9881 devices connected to a particular PCIe-6536 at each time is a 34-int32 stretch of `NI_waveform`. In the second step, $V_n^B(t_0)$ is stored into the n th int32 of that 34-int32 stretch as shown in **b**. In the third step, the first 32 int32's of the 34-int32 stretch are bit-wise transposed^{††}, resulting in the memory structure shown in **c**. In **d**, we graphically represent how this 34-int32 stretch of `NI_waveform` translates to outputs on each of the DIO outputs. The last two int32's shown in Figure 2.13**b-d**, which we name `CSblock`, are used for setting the global chip-select channels, DIO1 and DIO31, high^{‡‡} and appear in every 34-int32 stretch of `NI_waveform`.

The PCIe-6536 is capable of directly accessing (DMA) a computer's random access memory (RAM). Thus, even though the PCIe-6536 has a small on-board FIFO buffer, it is able to perform latency-free output for a large `NI_waveform` array. As currently configured, we transfer the `NI_waveform` array in sections of 7,650,000 int32's at a time^{*} using the `DAQmxWriteDigitalU32` function.

^{**}In principle, the DAC9881 only requires 24 clock cycles for each instruction, excluding the necessary chip-select actions.

^{††}To perform this bit-wise transpose, we use a straight-line version of `transpose32c` as described in Reference⁹⁴ and available at hackersdelight.org.

^{‡‡}In addition, DIO13 and DIO21, the DIO channels associated with the `SYNC` and `PD` inputs on each AD9522, are set high.

^{*}This number was chosen somewhat arbitrarily, the only consideration which I can recall is that it be an integer multiple of 34, in which case it would represent an integer number of bit-wise transpose operations.

In order for this piece-by-piece streaming of `NI_waveform` to work properly, it is important that `DAQmxConfigPipelinedSampClkTiming` is used for configuring the PCIe-6536 task.

2.3.4 PCIe-6536 DIO CHANNEL BUDGET

The AD9522 itself carries a 3 channel overhead as it itself needs to be configured to run properly.

More details regarding the use of each output channel of the PCIe-6536 host is shown in Table 2.2.

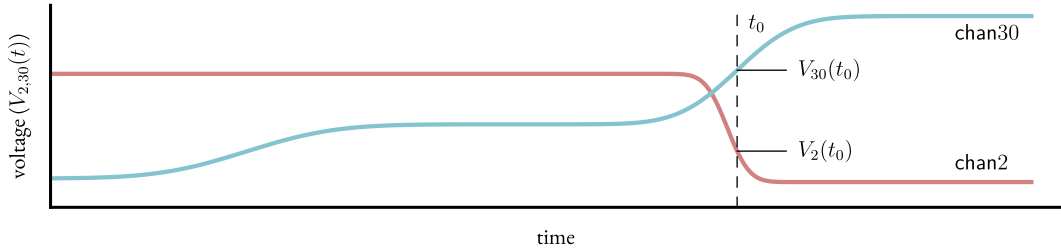
2.3.5 CLIENT DEVICES

In our experiment, we use DAC9881 designed in three different circuits, allowing for $[0, 5]V$, $[-5, 5]V$, and $[-10, 10]V$ operation. In addition, the PCIe-6536 system described is not restricted to programming DAC9881 devices. The digital waveforms sent to each potential peripheral device are subject to constraints due to the shared CS and SCLK lines. Additionally, due to the programming scheme described in the previous section, our implementation is restricted to communicating in words of exactly 32 bits wide. In spite of these constraints, the serial communication modules on many digital electronics are amenable to programming with this system and, at present, we also use this hardware control system to program the ADF4002 for generating radio frequency signals.

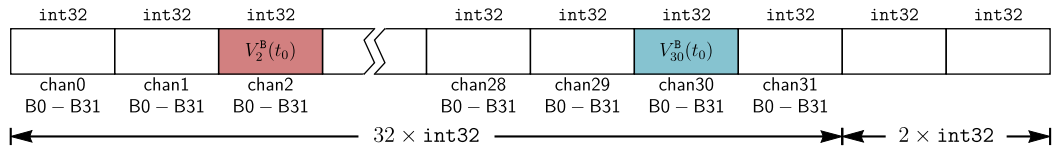
2.3.6 REDUCING NOISE

In order to reduce potential noise sources, the connection between the PCIe-6536 host and the DAC9881 clients is galvanically isolated using ADUM Isolators. In addition, the serial data are transmitted as LVDS signals on shielded twisted pair cables (easily available given their use as Ethernet

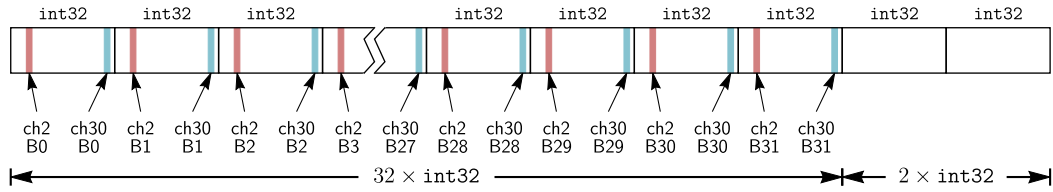
a desired analog waveform $V_n(t)$ in time for channels $n = 2, 30$



b $V_n^B(t_0)$ as initially stored in memory



c final memory (i.e. following bit-wise transpose) associated with $V_n^B(t_0)$



d memory as given to output

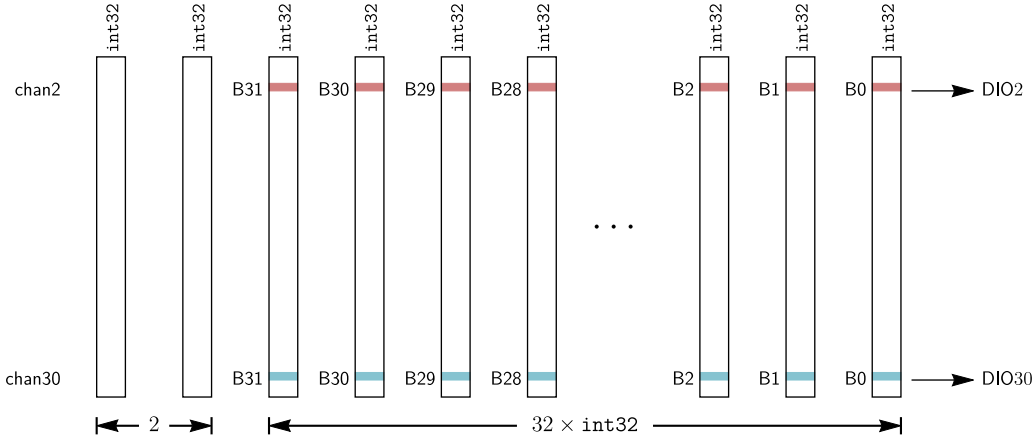


Figure 2.13: Analog data memory structure: This figure describes the protocol for generating the appropriate digital waveforms on the PCIe-6536 from the desired analog waveforms. **a**, We consider the analog voltage from channels 2 and 30 at time t_0 , $V_2(t_0)$ and $V_{30}(t_0)$. **b** Associated with time t_0 is a 34-int32 stretch of memory. We convert $V_2(t_0)$ and $V_{30}(t_0)$ into binary values with 18-bit precision, $V_2^B(t_0)$ and $V_{30}^B(t_0)$, and store them into the 2nd and 30th locations of the 34-int32 stretch of memory. **c** A bit-wise transpose is performed on this stretch of memory. **d** The bits are streamed out of the DIO ports as shown graphically.

Channel		
Type	#	Function
DIO	0	serial data channel
DIO	1	global chip select ($\text{DIO}(n < 15)$)
DIO	2	serial data channel
DIO	3	serial data channel
DIO	4	serial data channel
DIO	5	serial data channel
DIO	6	serial data channel
DIO	7	serial data channel
DIO	8	serial data channel
DIO	9	serial data channel
DIO	10	serial data channel
DIO	11	reference clock for AD9522
DIO	12	serial data channel
DIO	13	<u>SYNC</u> on AD9522
DIO	14	serial data channel
DIO	15	chip select for AD9522 programming
DIO	16	serial data channel
DIO	17	serial clock for AD9522 programming
DIO	18	serial data channel
DIO	19	serial data for AD9522 programming
DIO	20	serial data channel
DIO	21	<u>PD</u> for AD9522
DIO	22	serial data channel
DIO	23	serial data channel
DIO	24	serial data channel
DIO	25	serial data channel
DIO	26	serial data channel
DIO	27	serial data channel
DIO	28	serial data channel
DIO	29	serial data channel
DIO	30	serial data channel
DIO	31	global chip select ($\text{DIO}(n > 15)$)

Table 2.2: This table lists the function of each DIOchannel for each PCIe-6536. 24 channels serve as serial data channels and 2 channels serve as chip-select channels for client devices. The rest of the channels are used for the programming and control of the AD9522 associated with each PCIe-6536.

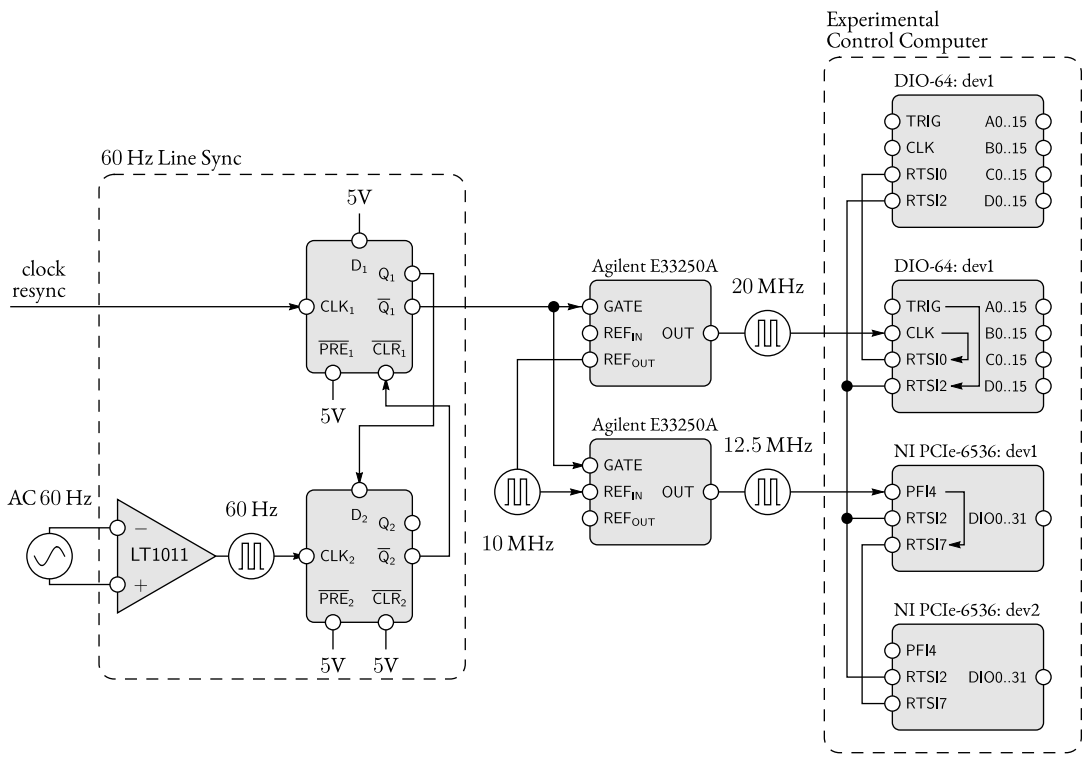


Figure 2.14: Experimental control synchronization: The circuit for the LT1011 has been dramatically simplified. For the actual circuit, see the circuit design for “Noise Immune 60 Hz Line Sync” on page 12 of Reference¹

cables), as shown in Figure 2.12. Both techniques are documented in more detail in References^{46,86}.

2.3.7 SYNCHRONIZATION

At the time of writing, the experiment utilizes two DIO-64 and two PCIe-6536 cards. Digital channels from the same device as well as separate devices must be consistently referenced to each other from experiment to experiment. In Figure 2.14, the synchronization scheme is diagrammed.

Starting from the right, the first DIO-64 device is clocked by an AGILENT E33250A function generator running at 20 MHz with 5V amplitude. This clock signal is internally rerouted to the RTSI0 and RTSI2 lines. The second DIO-64 device is clocked by a 10 MHz signal from the first generator. The NI PCIe-6536: dev1 board is clocked by a 12.5 MHz signal from the second generator. The NI PCIe-6536: dev2 board is also shown but has no connections. The Experimental Control Computer is connected to the DIO-64 boards via DIO lines A0..15, B0..15, C0..15, and D0..15, and to the NI PCIe-6536 boards via PFI4, RTSI2, and RTSI7 lines. A ‘clock resync’ signal is also present.

line on the RTSI bus shared by the two PCIe-6536 and two DIO-64 cards. The second DIO-64 device sources its sample clock from the RTSI0, thus synchronizing the DIO-64 devices. The first PCIe-6536 device receives a 12.5 MHz[†] 3.3V clock signal from an AGILENT E33250A function generator on its PFI4 line. This clock signal is internally rerouted to the RTSI7 line, which then clocks the second PCIe-6536 device.

The first DIO-64 is internally triggered. This pulse is internally rerouted to the RTSI2 line to trigger the rest of the devices. To maintain the phase reference, it is also important that the two AGILENT E33250A clocks are phase-referenced, which is accomplished through a shared 10 MHz reference.

The above protocol ensures mutual synchronization between all of the control devices. However it is also helpful to synchronize the experiment to the same phase of the 60 Hz AC line. This is accomplished through the 60 Hz line synchronization portion on the left side of the diagram in Figure 2.14, consisting of a LT1011 to convert the 60 Hz sine wave into a square wave and a pair of rising edge triggered D flip flops in the SN74HCT74 package. The output of this circuit gates the two AGILENT E33250A devices, which are set to Gated Burst mode[‡]. When the `clock_resync` line is low, the output of this circuit is high, allowing the two function generators to run and the PCIe-6536 and DIO-64 devices to output the programmed digital waveforms.

When a rising edge from the `clock_resync` line is detected, the AC line synchronization circuit is reset, with the output going low. This output will remain low until a specific point in the 60 Hz AC

[†]It is possible to double the analog update rate. The procedure includes setting this AGILENT E33250A function generator to 25 MHz. See Table 2.1 for more details.

[‡]The time between the rising edge on the gate and the first edge of the generated clock is fixed.

cycle. The overall effect is that a variable phase shift is added to the clock signals fed into the DIO-64 and PCIe-6536.

The DIO-64 can readily deal with the phase shift because it generates pulses based upon counting cycles of that input clock. The PCIe-6536 system cannot deal with the phase shift. While each PCIe-6536 is synchronized to follow the AGILENT E33250A function generator (whether directly or indirectly through the RTSI7 line) and thus should simply exhibit the phase shift required to synchronize with the AC line in its generated digital waveform at the time of the `clock_resync` pulse, the clock that is sent to the DAC9881 devices is generated from that PCIe-6536's associated AD9522[§]. On each AD9522 is a phase-locked loop (PLL) that locks an on-chip VCO to the reference signal on its `REFIN` port, which we have configured to be the digital waveform from DIO11 of its associated PCIe-6536 (See Table 2.2). Under normal operation, DIO11 outputs a consistent square wave. However, the phase shift that occurs when the `clock_resync` line is pulsed will throw the PLL on the AD9522 out of lock, thus feeding the DAC9881 peripherals with irregular waveforms and resulting in spurious output on these peripherals. The PLL on each AD9522 needs time to re-lock when it encounters this phase shift. Hence, prior to each `clock_resync` pulse, instructions are sent to each AD9522 through the SPI channel defined by DIO15, DIO17, and DIO19 to power down the distributed clocks, thus preventing any client devices from clocking in data. The distributed clocks are re-enabled 3.05 ms after the AGILENT E33250A function generators are re-enabled by the AC line synchronization circuit, a duration which is sufficiently long to allow for each AD9522's PLL to re-lock.

The `clock_resync` line and corresponding 60 Hz line synchronization are activated twice in the

[§]See discussion on *Increasing Scalability* in §2.3.2.

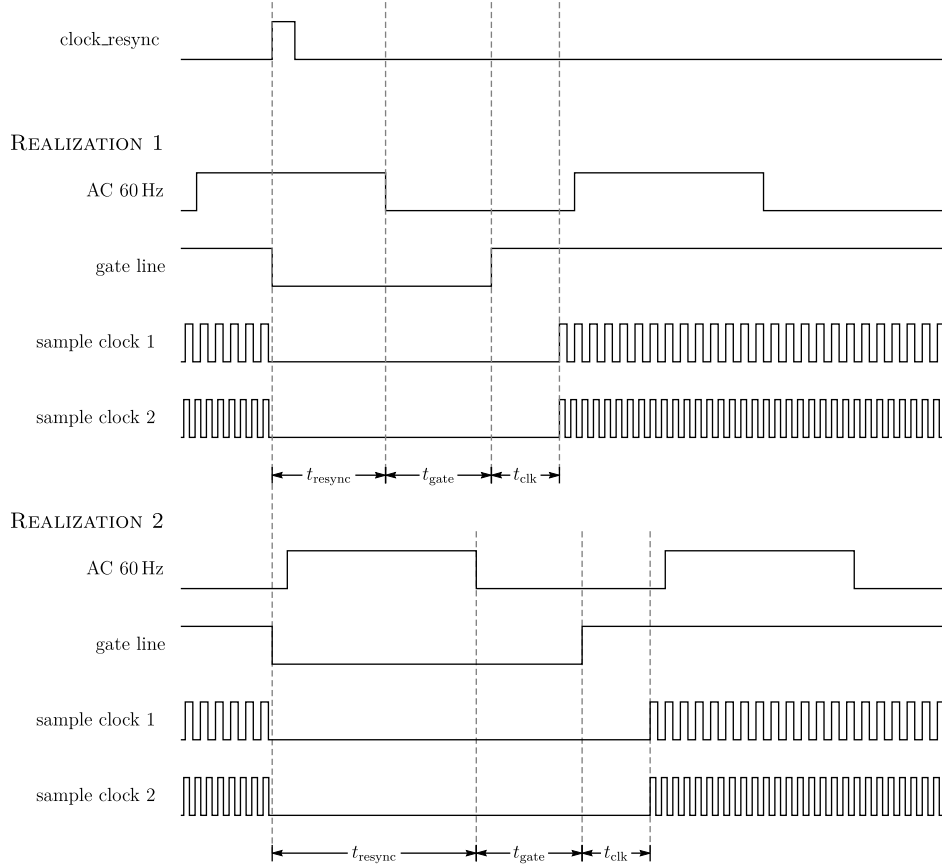


Figure 2.15: AC 60 Hz line synchronization: In this figure, we show two example timing diagrams for the sequence events that following a pulse on the `clock_resync` line shown in Figure 2.14. When a rising edge on the `clock_resync` line is detected, the gate line is forced low, causing the Agilent clock sources to cease outputting as shown by the flat-lining of sample clock 1 and sample clock 2 in the diagram (drawn frequencies are much slower than the 20 MHz and 12.5 MHz used in reality). The gate line stays low for a period t_{resync} during which the line sync circuit waits for a specific phase of the AC 60 Hz, which we have chosen arbitrarily for this diagram. As can be seen by comparing Realization 1 and Realization 2 in the diagram, t_{resync} is variable— changing because the experiment is not a fixed number of 60 Hz cycles. After t_{resync} , there are fixed delays of t_{gate} and t_{clk} (given by the electronics) after which the gate and sample clocks resume, respectively.

course of an experiment, once at the beginning and once following RF evaporation.

You should call it entropy, for two reasons. In the first place your uncertainty function as been used in statistical mechanics under that name, so it already has a name. In the second place, and more important, no one really knows what entropy really is, so in a debate you always have the advantage.

John von Neumann

3

Orbital excitation blockade and algorithmic cooling

This chapter has appeared in:

“Orbital Excitation Blockade and Algorithmic Cooling in Quantum Gases,”

W. S. Bakr, P. M. Preiss, M. E. Tai, R. Ma, J. Simon, M. Greiner

Nature 480, 500-503 (2011)

AN ULTRACOLD GAS OF BOSONIC ATOMS IN THE GROUND BAND OF AN OPTICAL LATTICE is described by the Bose-Hubbard model⁴⁹, in which atoms can tunnel between neighboring sites and interact via an onsite repulsive contact interaction. In a deep lattice where the interactions dominate, the ground state of the system is a Mott insulator with a fixed atom number per site that is locally constant over a region of the insulator³⁸. The energy per site in the absence of tunneling is $\frac{1}{2}U_{gg}n(n - 1)$, where U_{gg} is the interaction energy for two atoms in the ground lattice orbital state and n is the atom number on the site. The Mott state exhibits a transport blockade phenomenon in which the presence of an atom on a site energetically prevents tunneling of a neighboring atom onto that site even in the presence of a small bias between the sites. The transport is blocked unless the bias makes up for the interaction cost, making it possible, for example, to count atoms tunneling across double-wells in a superlattice²⁴. In this work, we explore an excitation blockade phenomenon that does not involve transport in the lattice. The excitation transfers localized atoms between different orbitals on the same site through modulation of the lattice depth at a frequency close to a vibrational resonance. Physics in higher optical lattice orbitals has been the focus of much recent experimental work including the study of dynamics in higher orbitals⁷⁰, multi-orbital corrections to the interaction energy⁹⁶, and unconventional forms of superfluidity involving higher orbitals^{97,90}.

3.1 INTERACTION-INDUCED ORBITAL EXCITATION BLOCKADE

The orbital excitation blockade (OEB) mechanism can be understood in the simplest scenario for two atoms in a single site of a deep three-dimensional lattice, in which the vibrational frequencies

in all three directions are taken to be different to avoid degeneracies. The lattice depth along the z -direction is modulated weakly, which in the presence of anharmonicity of the lattice potential drives atoms between the ground orbital and a single, specific excited z -orbital, subject to a selection rule that only allows coupling to orbitals of the same symmetry. For a single atom, excitation to the m th orbital requires modulation at a frequency $\omega_{z,0 \rightarrow m}$ which is approximately $m\omega_{z,0 \rightarrow 1}$ ignoring the anharmonicity of the onsite potential. With more than one atom on a site, the interaction introduces an orbital-dependent shift of the energy levels as shown in Figure 3.1. In general, the interaction shifts U_{gg} , U_{ge} , and U_{ee} are all different and the differences are a significant fraction of U_{gg} , where $g(e)$ denotes atoms in the ground (excited) orbital. If the coupling strength due to the modulation is small compared to these differences and the modulation frequency is tuned to $\omega_{z,0 \rightarrow m} + (U_{ge} - U_{gg})/\hbar$, only a single atom is transferred to the higher orbital and the transfer of a second atom is off-resonant. In this sense, the first excitation blocks the creation of a second excitation.

3.2 EXPERIMENTAL APPARATUS

The following experiments are utilize a two-dimensional Bose-Einstein condensate of rubidium atoms residing in a single plane of a one-dimensional optical lattice, henceforth referred to as the axial lattice, with a vibrational frequency of $\omega_{z,0 \rightarrow 1} = 2\pi \times 5.90(2)$ kHz. The z -axis is perpendicular to the plane and points along the direction of gravity. In addition, we introduce a lattice in the plane with a spacing of $a = 680$ nm and a depth of $45E_r$ (trap frequency of 17 kHz), where

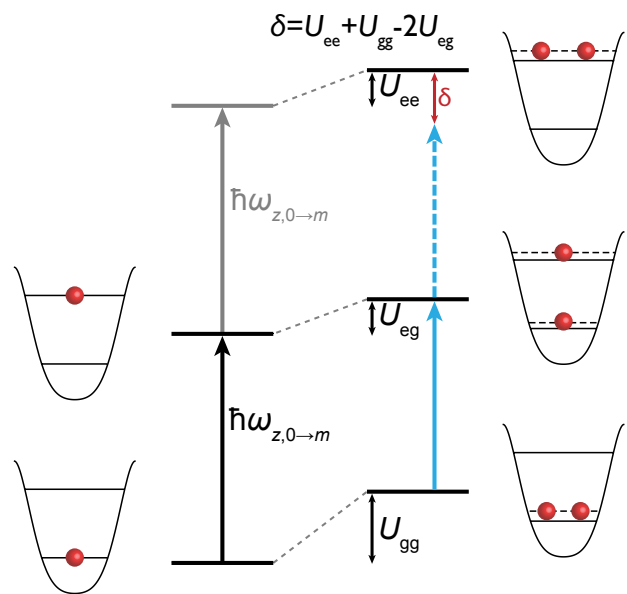


Figure 3.1: Orbital excitation blockade mechanism in an optical lattice. A single atom on a site is excited to a higher orbital by resonantly modulating the lattice depth. For two atoms on the same site, interactions lead to an orbital-dependent energy shift. Modulation at the appropriate frequency excites one of the atoms to the higher orbital, but is off-resonant for exciting the second with a blockade energy δ .

$E_r = \hbar^2/8ma^2$ is the recoil energy of the effective lattice wavelength, with m the mass of ^{87}Rb .

The resulting Mott insulator is at the focus of a high resolution optical imaging system capable of detecting atoms on individual lattice sites through fluorescence imaging. Light-assisted collisions at the start of the imaging process reduce the occupation of a site to its odd-even parity¹³.

3.3 ORBITAL EXCITATION BLOCKADE IN A MOTTO INSULATOR

We start by demonstrating coherent driving of atoms in a Mott insulator between two orbitals. In the presence of a harmonic trap, the atoms in a 2D Mott insulator are arranged in concentric rings of fixed atom number per site, known as shells, with the largest occupation at the center¹³. We prepare a Mott insulator with two shells and modulate the axial lattice depth by $\pm 1.1(1)\%$ at a frequency chosen to transfer atoms from the ground state to the second excited orbital. A modulation frequency corresponding to exactly $\omega_{z,0 \rightarrow 2}$ is resonant for atoms in the outer shell with one atom per site ($n = 1$). Excitation to the fourth excited orbital is suppressed because of an energy shift of $\hbar \times 1200(80)$ Hz owing to the anharmonicity of the onsite potential. Rabi oscillations between the states $|g\rangle$ and $|e\rangle$ are detected by lowering the axial lattice depth at the end of the modulation so that the excited orbital state becomes unbound and any population in it escapes along the z -axis due to gravity. The Rabi oscillations in that shell, shown in Figure 3.2b, have a frequency $\Omega = 2\pi \times 23.3(2)$ Hz.

The OEB is demonstrated in the inner $n = 2$ shell by modulating at a frequency of $\omega_{z,0 \rightarrow 2} + (U_{ge} - U_{gg})/\hbar$. For our parameters, U_{gg} , U_{ge} , and U_{ee} are $\hbar \times 480(30)$, $360(20)$, $310(20)$ Hz respectively. The

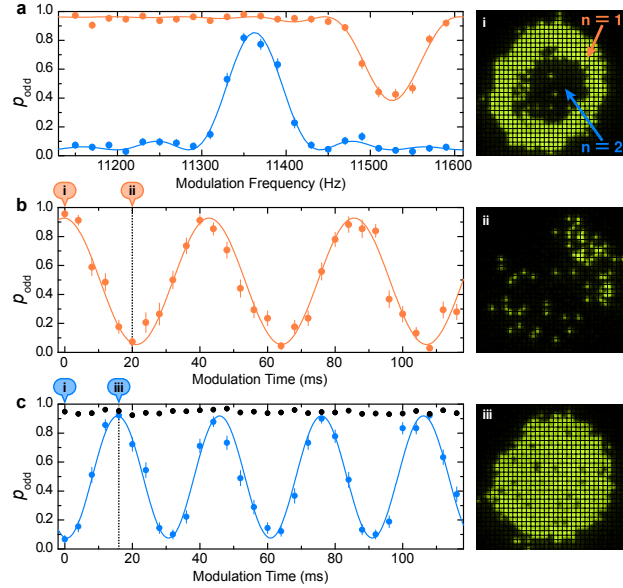


Figure 3.2: Time, frequency and site-resolved coherent transfer of atoms in a Mott insulator between orbitals. **a**, Excitations transferring a single atom in the $n = 1$ (orange) or $n = 2$ shell (blue) from the ground to the second excited orbital are spectroscopically resolved in a two-shell Mott-insulator. **b**, Rabi oscillations between the two orbitals are observed by driving at the resonant frequencies for atoms in the $n = 1$ shell and **c**, $n = 2$ shell of a Mott insulator. Bose-enhancement leads to faster oscillations in the $n = 2$ shell. When the atom number is reduced to obtain one atom per site in the region previously containing two atoms, the interaction shift suppresses oscillations (black). All error bars are one standard error of the mean. (i-iii) Site-resolved snapshots of the Mott insulator are shown at different points in the Rabi cycles.

Rabi oscillations between $|g, g\rangle$ and $1/\sqrt{2}(|e, g\rangle + |g, e\rangle)$ are detected as an oscillation of the parity between even and odd after ejecting the atom in the excited orbital and are shown in Figure 3.2c. For the same modulation amplitude as before, the oscillations are expected to occur $\sqrt{2}$ times faster than the resonant oscillation in the $n = 1$ shell owing to Bose-enhancement³³. We indeed observe a frequency ratio of 1.42(1) between the oscillation frequencies. A full frequency spectrum in the two shells is shown in Figure 3.2a and the frequency separation of the two resonances of 160(10) Hz matches well with the theoretically expected value of 165(35) Hz when the impact of virtual orbital changing collisions is included (see Methods).

3.4 COOLING THROUGH ALGORITHMIC NUMBER FILTERING

We next employ OEB to demonstrate a new path to cooling quantum gases. Evaporative cooling has been the workhorse technique for cooling atomic gases to nanokelvin temperatures. However, current interest in studying the physics of strongly-correlated materials, such as high- T_c cuprates, using ultracold gases^{58,20} has spurred research into developing new cooling techniques that can reach the requisite picokelvin regime^{66,67}. The field of quantum information offers an alternative cooling paradigm, wherein a sequence of unitary quantum gates purifies a subset of the qubits in a system by moving entropy and isolating it in another part of the system²¹. One realization of such a cooling scheme, heat-bath algorithmic cooling, has been successfully demonstrated with solid-state nuclear magnetic resonance qubits¹⁷. We introduce an analogous technique for quantum gases where the unitary operations are achieved using OEB, building on previous theoretical proposals in

this direction^{82,77,73,87}.

A bosonic quantum gas at a finite temperature T adiabatically loaded into the ground band of a optical lattice stores its entropy in the form of atom number fluctuations in the zero-tunneling limit. Within the local density approximation, a lattice site with a local chemical potential μ is described by a density matrix $\hat{\rho} = \sum_n p_n |n\rangle\langle n|$, where p_n , the probability of having n atoms on the site, is given by $e^{-\beta(\frac{1}{2}U_{gg}n(n-1)-\mu n)}/Z$. Here, $\beta = 1/k_B T$ and Z is the grand canonical partition function. Cooling to zero temperature is achieved by changing the atom number distribution on each site to obtain $p_n = \delta_{n,[\mu/U_{gg}]}$.

The crucial ingredient for algorithmic cooling is a unitary operation that realizes the transformation $|n, m\rangle \rightarrow |n - 1, m + 1\rangle$ for each n separately, where $|n, m\rangle$ denotes a Fock state with n atoms in the ground band and m atoms in an excited band. Resonant lattice modulation in the presence of OEB results in a rotation gate,

$$\hat{R}_{nm}(t) = \exp [i(\Omega_{nm}t|n - 1, m + 1\rangle\langle n, m| + c.c.)],$$

where Ω_{nm} is the transition's Rabi frequency and the required transformation is achieved for a modulation time $t = \pi/2\Omega_{nm}$. Entropy is transferred from the ground band to the excited band by performing a sequence of π gates $\hat{R}_{N-s,s}$ from $s = 0$ to $s = N - 1$ with N chosen large enough such that $p_N \approx 0$ in the initial state. At the end of this sequence, most of the entropy of the gas has been transferred to the excited band and can be removed from the system by ejecting the atoms in that band. The local chemical potential μ is readjusted to recover a situation closer to thermal equi-

librium by reducing the harmonic confinement to a new value ω_{low} so that $\mu < U_{gg}$ throughout the gas. At this point, residual entropy is stored in the resulting $n = 1$ Mott insulator in the form of holes that are preferably located near the edge of the cloud. The gas is allowed to rethermalize by lowering the lattice depth to allow tunneling, and the final entropy of the thermalized state would be significantly reduced compared to the initial state.

3.5 ALGORITHMIC COOLING OF A FINITE TEMPERATURE MOTTO INSULATOR

We start by experimentally demonstrating the algorithm on a state with known atom number, namely a four shell Mott insulator, and reducing the site occupation everywhere in the insulator to a single atom per site. To increase the blockade energy for this set of experiments, we transfer atoms to the fourth axial orbital rather than the second. We also replace the rotation gates demonstrated in the first part of this work with Landau-Zener transitions to improve the fidelity of the algorithm.

We linearly sweep the modulation frequency from 20.90 kHz to 21.65 kHz in 250 ms. The chirp realizes a sequence of quantum operations that transfer atoms to the excited orbital one at a time, until only one atom remains in the ground state in all shells (Figure 3.3a). We probe the ground orbital occupancy at different points in the frequency chirp by ejecting atoms in the higher orbital as before and then performing the parity imaging. The parity of the different shells during the chirp is shown in Figure 3.4a, and an analogue of the typical Coulomb blockade staircase is seen in the data. Shell-sensitive manipulation of a Mott insulator had been achieved in previous experiments using a microwave transition between hyperfine states, but the lack of a strong blockade allowed transfer of

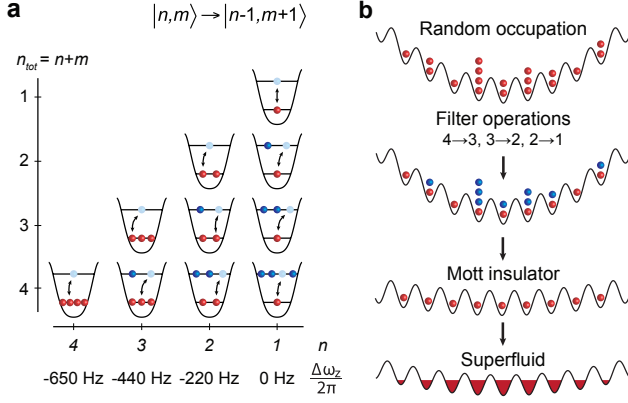


Figure 3.3: Algorithmic cooling in an optical lattice. **a**, Landau-Zener chirp for transferring entropy from the ground to the fourth band. The lattice modulation frequency is swept across the transition resonances from left to right. The interaction shifts $\Delta\omega_z$ for excitation of one of n atoms to the fourth orbital relative to the excitation frequency for a single atom on a site, are shown for different orbital occupations. Excitation processes in the same column happen at almost the same frequency to within 30 Hz (see Supplementary Table B.1). **b**, A state with random occupation in a deep lattice is far from the Mott insulating ground state. Sequential filtering operations followed by reduction of the confinement prepares the ground state, which can be adiabatically converted to a thermalized superfluid in a shallow lattice. Red (blue) spheres denote atoms in the ground (excited) band.

only a small fraction of the population to the target state²².

Next, we demonstrate cooling by performing the algorithm on a state that is far from the many-body ground state. To prepare such a state, we non-adiabatically load a condensate into a deep lattice, projecting the wavefunction onto a state with Poissonian site occupancy that rapidly loses coherence between sites. Using the same operation sequence as before, we progressively reduce the randomness of the ground band occupancy, preparing a single-occupancy Mott insulator (Figure 3.3b). We enhance the odd occupancy from 0.45(1) to 0.76(2) (Figure 3.4b), demonstrating significant atom number squeezing limited by the conversion efficiency of the Landau-Zener transitions. To complete the algorithm, we readjust the harmonic confinement to obtain a state close to the many-body ground state. We verify the ground state character by ramping back adiabatically to a $5E_r$

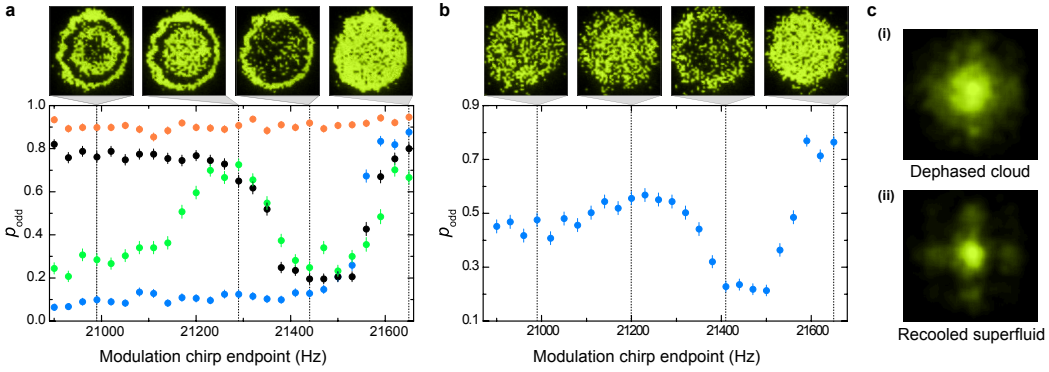


Figure 3.4: Experimental realization of algorithmic cooling. **a**, By chirping the modulation towards higher frequencies, atoms in a four-shell Mott insulator are sequentially excited one at a time to the fourth orbital. Population in the higher orbital is subsequently ejected at the end of the chirp. The average parity in the $n = 1$ (orange), $n = 2$ (blue), $n = 3$ (black) and $n = 4$ (green) shell is shown at different points in the chirp, together with single shot images, illustrating the conversion to a three, two and finally one shell insulator. **b**, The same frequency chirp algorithmically cools a state with random occupancy into an $n = 1$ Mott insulator, observed as an enhancement in odd occupancy. All error bars are one standard error of the mean. **c**, (i) An incoherent cloud does not exhibit an interference pattern in a 5 ms time of flight expansion after adiabatically lowering the lattice depth. (ii) Cooling converts the incoherent cloud to a Mott insulator in the deep lattice. After adiabatically lowering the lattice depth, a superfluid forms and an interference pattern is obtained in the expansion images.

lattice in 100 ms and releasing the atoms from the lattice. Without cooling, we obtain a featureless cloud shown in Figure 3.4c(i), indicating an absence of the coherence expected in the superfluid ground state. With cooling, the Mott insulator is adiabatically converted to a superfluid, giving rise to matter wave interference peaks shown in Figure 3.4c(ii).

3.6 TECHNICAL LIMITATIONS

We now discuss the limits on the entropies that can be achieved with algorithmic cooling. The conversion efficiency to a single-occupancy Mott insulator is technically limited in our system by heating due to spontaneous emission during the sweep and to a lesser extent, by the efficiency of the Landau-Zener sweep for clouds with large average occupancies (see Methods). While we have

demonstrated cooling of hot clouds, the single-occupancy probability we have achieved using algorithmic cooling in a two-shell Mott insulator is $0.94(1)$. This is comparable to what had been previously achieved with evaporative cooling, corresponding to an average entropy of $0.27k_B$ per particle¹³. Nevertheless, lattice heating can be made negligible by using a further-detuned lattice (e.g. 1064 nm), while shaped pulses can improve the Landau-Zener transfer efficiency⁷⁷. More fundamentally, the single-shot cooling algorithm we have implemented is limited by initial holes in the Mott insulator which cannot be corrected. However, repeated iterations of the algorithm can circumvent this problem and bring the cloud to zero entropy with quick convergence⁷⁷. The cycle alternates between (a) using OEB to produce a reduced entropy $n = 1$ insulator in a harmonic confinement ω_{low} (demonstrated above) and (b) adiabatically increasing the confinement to ω_{high} in the presence of tunneling to move hot particles to the center of the cloud where they can be removed again. Alternatively, the outer edge of the cloud containing the holes can be removed using the high resolution available in our system⁹⁵.

3.7 CONCLUSION

In conclusion, we have observed a new blockade phenomenon in optical lattices when exciting atoms to higher orbitals, analogous to dipole excitation blockade in Rydberg atoms. The blockade permits deterministic manipulation of atom number in an optical lattice. We have used it to convert a multi-shell Mott insulator into a singly-occupied insulator with over a thousand sites, the largest quantum register achieved so far in an addressable system. The same technique allows initialization

of registers in longer wavelength lattices where a Mott insulator cannot be prepared⁷². OEB also opens a route to implementing quantum gates in optical lattices. Single-site addressing⁹⁵, possible with our microscope, can perform rotations of individual orbital-encoded qubits rather than the global rotations demonstrated in this work. Controlled-NOT gates can be implemented by conditionally moving the control qubit onto the target qubit site, and performing an interaction-sensitive rotation of the target qubit⁸⁴. Finally, the algorithmic cooling technique we have developed could potentially achieve the ultralow entropies required for quantum simulation^{58,20} and computation in optical lattices, and establishes a bridge to quantum information for importing novel ideas for cooling quantum gases.

Don't let your heart depend on things

That ornament life in a fleeting way!

He who possesses, let him learn to lose,

He who is fortunate, let him learn pain.

Friedrich Schiller in *Die Braut von Messina*

4

Quantum thermalization of an isolated, many-body quantum system

Portions of this chapter have appeared in:

“Quantum thermalization through entanglement in an isolated many-body system,”

A. M. Kaufman, M. E. Tai, A. Lukin, M. N. Rispoli, R. Schittko, P. M. Preiss, M. Greiner

Science 353, 6301, 794-800 (2016)

THE CONCEPT OF ENTROPY IS FUNDAMENTAL TO THERMALIZATION, yet appears at odds with basic principles in quantum mechanics. Statistical mechanics relies on the maximization of entropy for a system at thermal equilibrium. However, an isolated many-body system initialized in a pure state will remain pure during Schrödinger evolution, and in this sense has static, zero entropy. The underlying role of quantum mechanics in many-body physics is then seemingly antithetical to the success of statistical mechanics in a large variety of systems.

We have experimentally studied the emergence of statistical mechanics in a quantum state and observed the fundamental role of quantum entanglement in facilitating this emergence. We performed microscopy on an evolving quantum system and we saw thermalization occur on a local scale, while we measured that the full quantum state remained pure. We directly measured entanglement entropy and observed how it assumes the role of the thermal entropy in thermalization. Although the full state remained measurably pure, entanglement created local entropy that validated the use of statistical physics for local observables. In combination with number-resolved, single-site imaging, we demonstrated how our measurements of a pure quantum state agreed with the Eigenstate Thermalization Hypothesis and thermal ensembles in the presence of a near-volume law in the entanglement entropy.

We did all of this and reported the results through a manuscript published in 2016⁵². For more details, I must refer you to `(future thesis)`.

The effect of a uniform magnetic field on the conduction electrons in a magnetic field is of general interest for a variety of magnetic phenomena.

Philip G. Harper

5

Microscopy of the interacting Harper-Hofstadter model

Portions of this chapter will appear in:

“Microscopy of the interacting Harper-Hofstadter model in the two-body limit,”

M. E. Tai, A. Lukin, M. N. Rispoli, R. Schittko, T. Menke, D. Borgnia, P. M. Preiss,
F. Grusdt, A. Kaufman, M. Greiner

THE INTERPLAY OF MAGNETIC FIELDS AND INTERACTING PARTICLES can lead to exotic phases of matter exhibiting topological order and high degrees of spatial entanglement²⁵. While these phases were discovered in a solid-state setting^{93,55}, recent techniques have enabled the realization of gauge fields in systems of ultracold neutral atoms^{63,59,50,54,62,3,60,6,8,53}, offering a new experimental paradigm for studying these novel states of matter. This complementary platform holds promise for exploring exotic physics in fractional quantum Hall systems due to the microscopic manipulation and precision possible in cold atom systems^{91,40,34}. However, these experiments thus far have mostly explored the regime of weak interactions^{85,100,51,92,64,5,68}. Here, we show how strong interactions can modify the propagation of particles in a $2 \times N$, real-space ladder governed by the Harper-Hofstadter model^{41,44}. We observe inter-particle interactions affect the populating of chiral bands, giving rise to chiral dynamics whose multi-particle correlations indicate both bound and free-particle character. The novel form of interaction-induced chirality observed in these experiments demonstrates the essential ingredients for future investigations of highly entangled topological phases of many-body systems.

The Harper-Hofstadter Hamiltonian is a model for describing lattice systems in the presence of a gauge field. When the system is confined to a ladder or strip geometry, two bands of opposite chirality emerge and give rise to chiral edge modes⁴⁷. Edge modes have been a subject of increasing interest in the condensed matter and quantum information communities⁷¹ because of their topologically-protected properties, which arise due to the absence of backscattering in the presence of chirality⁴³. They have been studied in photonic systems³⁹, and in atomic lattice systems with synthetic dimensions using macroscopic observables^{92,64}. While synthetic dimensions provide an

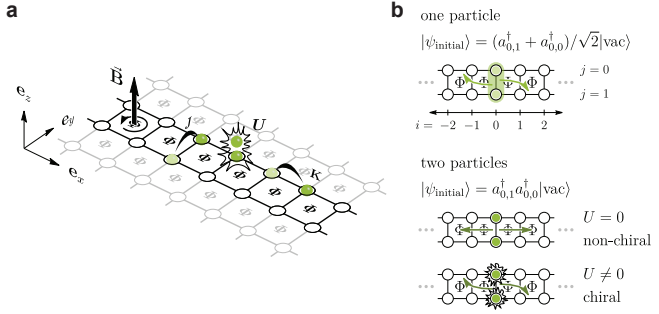


Figure 5.1: **a**, From a 2D lattice, we isolate a $2 \times N$ ladder region in which we study the Harper-Hofstadter model. Nearest neighbor lattice sites in the x and y direction are coupled by complex- and real-valued tunnelings with magnitudes K and J , respectively, realizing an artificial gauge field with constant flux per unit cell Φ . When multiple atoms occupy the same lattice site, they experience a pairwise interaction shift U . **b**, We first study the motion of a single particle delocalized over two sites of a given rung. Due to the coupling of motion in the x and y directions induced by the gauge field, chiral dynamics emerge where rightward (leftward) motion is correlated with a bias towards the lower (upper) leg of the ladder. However, a pair of non-interacting particles initialized onto opposite sides of a single rung does not exhibit chirality even in the presence of a gauge field. The addition of interactions breaks the symmetry between particles going to the left and to the right, thereby reintroducing chiral motion.

elegant solution to realize well-controlled, finite systems²³, we introduce a tunable, real-space, finite lattice that can be extended in straightforward ways to studies in arbitrary geometries (Figure 5.1a). We create a finite ladder in which we perform microscopic studies of the edge modes at the single-particle level: we prepare a well-defined initial state to load these edge modes and allow the state to evolve under the Hamiltonian to expose the chiral nature of the dynamics (Figure 5.1b). An imbalanced decomposition of the initial state into the two chiral bands results in shearing in the particle propagation, i.e. a particle is more likely to occupy a specific leg of the ladder and which leg is dependent on its velocity. This shearing indicates a coupling of the dynamics along the leg (x) and rung (y) directions of the ladder that is reminiscent of a Lorentz force.

In the presence of interactions, the dynamics of even two particles is substantially modified from the expectation obtained from a single-particle picture. The interactions modify the eigenspectrum

such that states of both scattering and bound nature emerge, the population of which governs the observed dynamics. Importantly, the interactions provide an avenue through which states of a certain chirality can be preferentially populated, giving rise to chiral trajectories in situations where such chirality would be absent for vanishing interactions, even in the presence of a gauge field (Figure 5.1b). By exploiting the toolset of quantum gas microscopy^{11,88} — spatially resolved correlations and single-particle observables — we experimentally identify the mechanisms through which interactions produce these chiral dynamics. Importantly, while the measurements performed here are all non-equilibrium, the excellent agreement between theory and experiment, in the presence of interactions, paves the way for equilibrium measurements of chiral ground states^{29,91,40,83}.

Our experiments begin with a two-dimensional Bose-Einstein condensate of Rubidium-87 atoms. These atoms sit at the focus of a high-resolution imaging system through which we project a square optical lattice with spacing $a = 680$ nm. By collecting atomic fluorescence, we detect the parity of site occupations on the individual site level. On this platform, we realize the Harper-Hofstadter Hamiltonian,

$$\mathcal{H} = \frac{U}{2} \sum_{i,j} \hat{n}_{i,j} (\hat{n}_{i,j} - 1) - \sum_{i,j} \left(K e^{-i\phi_{i,j}} \hat{a}_{i+1,j}^\dagger \hat{a}_{i,j} + J \hat{a}_{i,j+1}^\dagger \hat{a}_{i,j} + \text{h.c.} \right), \quad (5.1)$$

where U is an on-site, pairwise repulsive interaction energy and K and J are tunneling amplitudes between nearest neighbors on the lattice. $\hat{a}_{i,j}^\dagger$, $\hat{a}_{i,j}$, and $\hat{n}_{i,j}$ are the creation, annihilation, and number operators for site (i, j) , where $i \in \mathbb{Z}$ and $j \in \{0, 1\}$ for a ladder geometry. The spatially varying complex tunneling phases, $\phi_{i,j}$, are realized through the combination of a magnetic field gradient

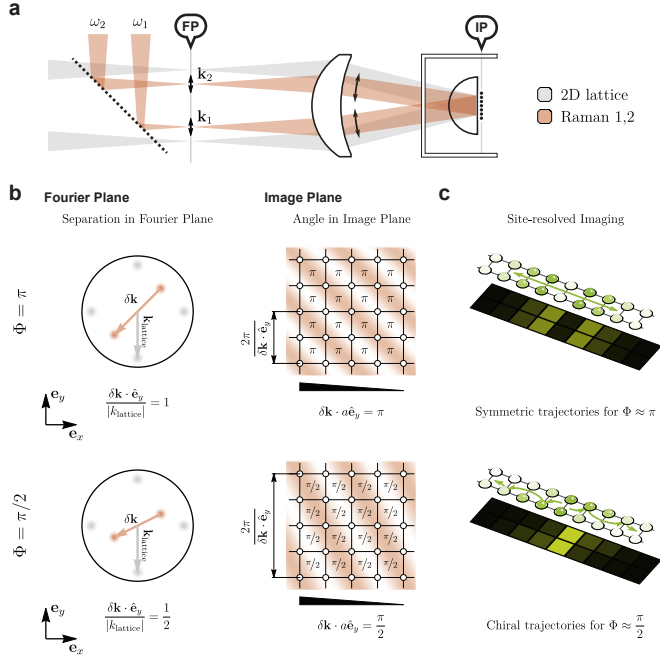


Figure 5.2: Using a quantum gas microscope, we can realize artificial gauge fields of variable strength by projecting a running lattice with variable spacing through the same objective used to project the static 2D lattice and image the atoms. **a**, A pair of beams (in gray) interfere in the image plane of the microscope, creating one axis of the 2D optical lattice. A pair of Raman beams with wavevectors \mathbf{k}_1 and \mathbf{k}_2 and slightly different frequencies ω_1 and ω_2 (in brown) also interfere in the image plane, creating a running lattice. We can adjust the periodicity and orientation of the Raman lattice by moving the position of the beams in the Fourier plane of the microscope. **b**, Top (bottom) row: example realizing flux $\Phi = \pi$ ($\Phi = \pi/2$) in the system. Fourier plane of the microscope: gray (brown) disks correspond to the beams used to create the 2D (Raman) lattice with resulting wavevector k_{lattice} ($\delta\mathbf{k} \equiv \mathbf{k}_1 - \mathbf{k}_2$). The ratio of the y component of the Raman lattice wave vector and the lattice wave vector determines the flux in the system^{6,68}. Resulting image plane structure: The 2D lattice is represented by the black grid. The brown shading represents the spatial intensity distribution of the running Raman lattice at one instance in time. The black triangle indicates the potential gradient imposed by a physical magnetic field, which is used to detune lattice sites along the x direction. **c**, Resulting dynamics for example cases of $\Phi \approx \pi$ and $\Phi \approx \pi/2$ flux. The top diagram for each example illustrates the time dynamics of the center of mass for particles traveling to the left and to the right from the initial rung. The bottom diagram is the measured density distribution following time evolution, exhibiting asymmetric propagation for a flux $\Phi \approx \pi/2$.

to energetically detune nearest neighbors and a running lattice to drive Raman transitions to restore tunneling between these sites^{6,68}. For a loop around a unit cell, these tunneling phases result in a non-trivial net phase Φ , yielding an effective magnetic field by playing the role of the Aharonov-Bohm phase acquired by a charged particle in a real magnetic field. The flux Φ is controlled in our system by the angle between the running lattice and the static lattice on which the atoms reside. Because the Raman lattice is projected through the objective, as shown in Figure 5.2a, we are able to dynamically tune the effective magnetic field from the weak to strong field limits within a single experiment, without having to change the laser wavelengths (see §2.2). Finally, we utilize a digital micromirror device in a Fourier plane of our projection path to superimpose arbitrary optical potentials⁹⁸, which we use in state preparation and to confine evolution to a $2 \times N$ ladder region. For the experiments that follow, we operate in the regime where $K/h \approx 10$ Hz, $J/h \approx 35$ Hz, and $U/h \approx 130$ Hz, with h being Planck's constant. The spatially varying phase can be expressed $\phi_{i,j} = \pi \cdot i + \Phi \cdot j$.

5.1 SINGLE-PARTICLE CHIRAL DYNAMICS

We probe the band structure of the $2 \times N$ Harper-Hofstadter ladder by studying single-particle dynamics⁴⁷. The band structure of this system admits eigenstates of opposite chirality. We preferentially load eigenstates of a certain chirality by preparing a specific initial state. We study the resulting chiral propagation by recording the time evolution of the density distribution.

For the experiments that follow, we focus on studying the dynamics of an atom delocalized be-

tween the two sites of a single rung. To create this state, we start from a Mott insulator and remove all but a single atom^{79,48}. By means of a magnetic field gradient, we apply a large potential offset in the rung direction (\mathbf{e}_y) at a high lattice depth so that this single localized atom realizes the ground state of a single rung. The potential offset is then adiabatically decreased to zero, realizing a Landau-Zener sweep to a rung with no energy offset between the two constituent sites (Figure 5.3). In this final configuration, the ground state is a symmetrically delocalized state. Hence, we start with the initial state

$$|\psi_{\text{initial}}\rangle_{1p} = \frac{1}{\sqrt{2}}(a_{0,1}^\dagger + a_{0,0}^\dagger)|\text{vac}\rangle \equiv \hat{a}_{0,S}^\dagger|\text{vac}\rangle.$$

If we had instead configured the potential offset such that the localized atom were on the higher energy site of the rung, the adiabatic sweep to a balanced rung would prepare

$$|\psi_{\text{opposite sweep}}\rangle = \hat{a}_{0,A}^\dagger|\text{vac}\rangle = \frac{1}{\sqrt{2}}(a_{0,1}^\dagger - a_{0,0}^\dagger)|\text{vac}\rangle,$$

which is the highest energy state of the rung subsystem.

From the initial state $\hat{a}_{0,S}^\dagger|\text{vac}\rangle$, we investigate the effect of the artificial magnetic field on the atom's propagation dynamics after suddenly reducing the lattice depth in the x direction^{92,64,8}. In each experimental realization, we image the atom to be in a single location of the ladder. Through averaging multiple realizations, we obtain the wavefunction density distribution, which can be repeated for several evolution times.

At zero flux, the particle's motion is separable and, hence, we would expect no dynamics along

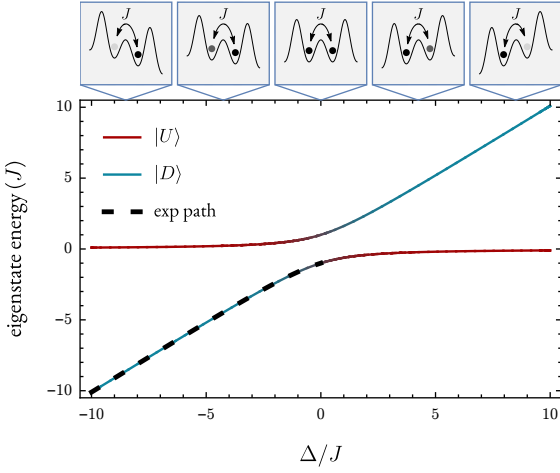


Figure 5.3: A doublewell with sites $|U\rangle$ and $|D\rangle$ describes an isolated rung of a $2 \times N$ ladder. In the presence of a tunnel coupling J and energy offset Δ , the system admits two dressed states. We start in the limit where Δ is such that the ground state is approximately $|D\rangle$ and adiabatically sweep the energy offset to realize the ground state at $\Delta = 0, (|U\rangle + |D\rangle)/\sqrt{2}$.

the y direction since we prepared the atom in the ground state along this dimension. However, a particle's coupling to a magnetic field gives rise to a non-separable Hamiltonian, yielding chirality and multi-dimensional dynamics in the atom's motion which are revealed in the temporal evolution of the density distribution. In Figure 5.4b, we focus on the center-of-mass of these distributions. Since the magnetic field couples to the velocity of a particle, we expect that leftward and rightward motion to be affected differently. Hence, our analysis considers the left (blue) and right (orange) halves separately, which should separate the behavior of leftward- and rightward-moving particles. For each half, we plot the x and y components of the center-of-mass, x_{COM} and y_{COM} respectively, as a function of evolution time in the ladder.

For short times, the magnetic field causes shearing in the population distribution—the population that propagates to the right (left) is initially biased towards the upper (lower) leg of the ladder,

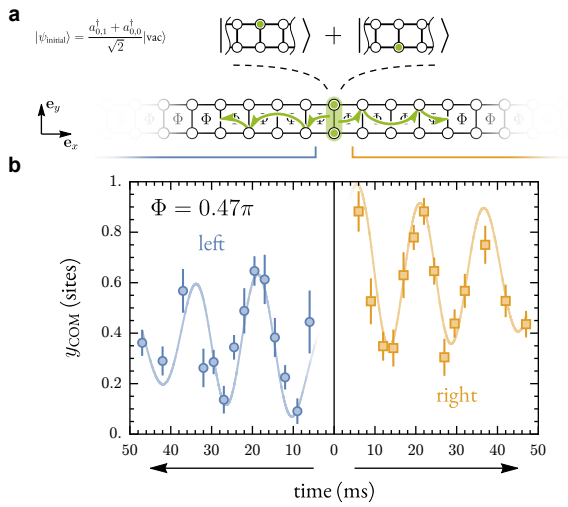


Figure 5.4: **a**, In the presence of a gauge field, a particle delocalized across a single rung exhibits chiral motion (an exemplary trajectory is indicated by the green arrows). **b**, To quantify the chiral dynamics, we track the time evolution of the x and y components of the center-of-mass for the left (blue) and right (orange) halves of the system for a flux of $\Phi = 0.47\pi$. Population on the initial rung is always excluded from the center-of-mass determination. While the particle symmetrically delocalizes over multiple sites in the x direction (see Methods), its motion in the y direction is asymmetric with respect to the central rung. The data is matched well by a simulation using exact diagonalization of the Harper-Hofstadter model, performed for our system with the tunnelings fit to $K/h = 12(1)$ Hz and $J/h = 29(2)$ Hz. Due to technical errors in the initial state preparation (see Methods), the chiral trajectory is slightly modified from the case of a symmetric superposition.

similar to what one would expect for a Lorentz force. As time progresses, the population encounters the edge of the system and reflects, making semicircular trajectories reminiscent of skipping orbits. These oscillations in the density persist for long times and remain out of phase with each other and biased towards opposite legs.

5.1.1 PREPARATION ERRORS

Due to technical issues, we do not prepare exactly the symmetric superposition state. If we parametrize the initial state as

$$\psi = \sin \theta |0, 0\rangle + e^{i\varphi} \cos \theta |0, 1\rangle,$$

non-adiabaticity in the Landau-Zener sweep can result in a non-zero phase ϕ . If the sweep does not terminate with a completely balanced double well, the population mixing angle θ will deviate from $\pi/4$.

A non-zero relative phase ϕ will result in oscillations of y_{COM} even in the absence of a magnetic field. However, the oscillations in the left and right halves of the system will occur in phase with each other. It is only in the presence of a magnetic field that these oscillations can be temporally shifted relative to each other.

5.1.2 BLOCH SPHERE

While an appeal to classical physics makes the chiral orbits unsurprising, the single particle quantum walks can be treated more quantum mechanically by considering an effective one-dimensional

coupling axis	coupling direction	matrix element	Bloch sphere action
along rungs	\uparrow	J	precession about x -axis
along rungs	\downarrow	J	precession about x -axis
along legs	\rightarrow	$Ke^{-i\phi_{i,j}}$	$\Delta\phi = \Phi$ azimuthal rotation
along legs	\leftarrow	$Ke^{i\phi_{i-1,j}}$	$\Delta\phi = -\Phi$ azimuthal rotation

Table 5.1: The $2 \times N$ Harper-Hofstadter ladder can be mapped to a 1D chain of Bloch spheres. We tabulate the actions of the original coupling terms in the effective Bloch spheres.

chain of two-level systems. On rung i of the ladder, the two sites, $(i, j), j \in \{0, 1\}$, of the doublewell compose an effective two-level system for which we define the Bloch vector where $|1\rangle_0\rangle_m$ and $|0\rangle_1\rangle_m$ lie along the north and south pole, respectively, where $|1\rangle_0\rangle_m$ ($|0\rangle_1\rangle_m$) denotes an atom on the top (bottom) leg of rung m . States in the xy -plane are superposition states of the form $|1\rangle_1\rangle_m + e^{i\phi_m} |0\rangle_0\rangle_m$. This Bloch vector lives in a Bloch sphere that only pertains to the state of rung m of the ladder. The length of this local Bloch vector is given by the total population in that rung. The polar angle is given by the mixing angle between the $|1\rangle_0\rangle_m$ and $|0\rangle_1\rangle_m$.

Each rung of the ladder defines a Bloch sphere with an associated Bloch vector. The vertical J coupling causes each local Bloch vector to precess around the \mathbf{e}_x axis in its local Bloch sphere. Simultaneously, the horizontal K coupling causes population to move between the local Bloch spheres, where transfer between the Bloch spheres is accompanied by a rotation about the \mathbf{e}_z axis, the direction of which depends on whether the transfer goes towards the right or left on the ladder. This directional-dependence is the key to the chirality in the single-particle quantum walks. These actions are summarized in Table 5.1.

The initial state $|\psi_{\text{initial}}\rangle = (a_{0,1}^\dagger + a_{0,0}^\dagger)/\sqrt{2} |\text{vac}\rangle$ lies along the \mathbf{e}_x axis. Due to the horizontal K coupling, the population will propagate outwards, causing the Bloch vectors in the neighboring

local Bloch spheres to grow. In addition to increasing in magnitude, they will also rotate from the initial position along the \mathbf{e}_x axis. The Bloch vectors in the local Bloch spheres to the right (left) of the initial rung will be rotated towards positive (negative) ϕ values. The vertical J coupling will cause each of these local Bloch vectors to precess about the \mathbf{e}_x axis. For a positive (negative) ϕ value, the Bloch vector will rotate towards the north (south) pole, which corresponds to the top (bottom) leg.

This Bloch sphere framework also allows us to consider other initial states.

- The antisymmetric superposition, $(a_{0,1}^\dagger - a_{0,0}^\dagger)/\sqrt{2}|\text{vac}\rangle$ lies along the $-\mathbf{e}_x$ axis. Whereas the symmetric state picks up a ϕ phase such that it precesses towards the north pole when the population propagates to the right, i.e. $\vec{\Omega} \times (\text{Rot}_z(\Phi)\mathbf{e}_x) > 0$, the antisymmetric state starts from the $-\mathbf{e}_x$ axis, so the rotation caused by the J coupling actually causes the population to precess towards the south pole for the same propagation direction, i.e. $\vec{\Omega} \times (\text{Rot}_z(\Phi)(-\mathbf{e}_x)) < 0$. This results in an orbit to the symmetric state, except with a chirality of opposite sign.
- An atom localized on the top leg will lie along the \mathbf{e}_z axis. The direction-dependent rotation about the polar axis caused by the horizontal K coupling has no effect on this state since it lies along the polar axis. The vertical J coupling will cause the state to precess about the \mathbf{e}_x axis, taking it off the polar axis. However, the resulting direction-dependent rotation from the horizontal K coupling does not lead to any imbalance in the top and bottom leg for leftward and rightward moving population since

$$\vec{\Omega} \times (\text{Rot}_z(\Phi) \text{Rot}_x(\epsilon_\theta) \mathbf{e}_z) = \vec{\Omega} \times (\text{Rot}_z(-\Phi) \text{Rot}_x(\epsilon_\theta) \mathbf{e}_z)$$

- The beamsplitter state, $(a_{0,1}^\dagger + ia_{0,0}^\dagger)/\sqrt{2}|\text{vac}\rangle$, which can be easily created by allowing a single localized atom to evolve in a doublewell, lies along the \mathbf{e}_y axis. It does not exhibit any chirality because the action of the direction-dependent rotation from the horizontal K coupling does not result in any difference in the precession caused by the $\vec{\Omega}$ coupling.

$$\vec{\Omega} \times (\text{Rot}_z(\Phi) \mathbf{e}_y) = \vec{\Omega} \times (\text{Rot}_z(-\Phi) \mathbf{e}_y)$$

coupling axis	coupling direction	matrix element	Bloch sphere action
along rungs	\uparrow	$Ke^{-i\phi_{i,0}}$	precession about $\text{Rot}_z(\Phi \cdot m)\mathbf{e}_x$ axis
along rungs	\downarrow	$Ke^{i\phi_{i,0}}$	precession about $\text{Rot}_z(\Phi \cdot m)\mathbf{e}_x$ axis
along legs	\rightarrow	J	no azimuthal rotation
along legs	\leftarrow	J	no azimuthal rotation

Table 5.2: We tabulate the actions of the Harper-Hofstadter coupling terms in the effective Bloch spheres when the complex phases are placed along the rungs. Note, $\text{Rot}_z(\Phi \cdot m)$ is meant to indicate a rotation of $\Phi \cdot m$ about the z -axis, i.e. $\cos(\Phi \cdot m)\mathbf{e}_x + \sin(\Phi \cdot m)\mathbf{e}_y$.

Reversing the direction of the magnetic field is equivalent to performing the mapping $\Phi \mapsto -\Phi$.

In the Bloch sphere picture, the result is that the Bloch vector rotates in the opposite sense about the \mathbf{e}_z axis as population propagates from one local Bloch sphere to another. This switches the sign of the chirality for a given initial state as one would expect classically.

While experimental considerations dictated that the complex phase was associated with the horizontal tunneling elements, there are other possible arrangements that result in the same magnetic field and physical observables since these are gauge invariant quantities. For example, if we had associated the complex phase with the vertical tunneling elements instead, then the coupling along each rung would carry a phase that differs by Φ from its neighboring rung. The horizontal elements would all be identical with no complex phase. In the Bloch sphere framework, the transfer of population between neighboring local Bloch spheres does not involve a rotation about the polar axis. However, the Rabi vector in each local Bloch sphere differs, rotating by Φ around the polar axis for each successive rung. We tabulate these actions in Table 5.2.

5.2 SINGLE-PARTICLE BAND STRUCTURE

The Bloch sphere picture is effective at developing intuition for the single-particle dynamics. However, by turning to the band structure of the system, we can develop a framework that is amenable to more complicated initial states and, more importantly, will be useful for understanding the two-particle interacting quantum walks in the next section. Here, we present a brief derivation of the energy spectrum, first considering the dispersion of isolated legs of the ladder and then adding in the inter-leg coupling.

Our ladder system is composed of two legs with couplings along the rungs and legs of strengths J and K . For a single particle, our system is governed by the following Harper-Hofstadter Hamiltonian

$$\mathcal{H} = - \sum_{m,n} \left(K e^{-i\phi_{m,n}} \hat{a}_{m+1,n}^\dagger \hat{a}_{m,n} + J \hat{a}_{m,n+1}^\dagger \hat{a}_{m,n} + \text{h.c.} \right). \quad (5.2)$$

The complex phase $\phi_{m,n} = \pi \cdot m + \Phi \cdot n$ in the horizontal tunneling term is given by the phase of the Raman lattice and gives rise to an effective magnetic vector potential which manifests physically as an effective flux per plaquette of Φ . Because of the gauge invariance of the vector potential, the complex phase $\phi_{m,n} = \Phi \cdot (n - 1/2)$, which gives an identical flux per plaquette*, is equally valid for describing physical observables. For ease of calculations, we implicitly perform the gauge that results in this modified form for $\phi_{m,n}$. Additionally, we will define $\hat{a}_{m,0} \equiv \hat{b}_m$ and $\hat{a}_{m,1} \equiv \hat{a}_m$ for this derivation to simplify the notation in the following calculation. Then, we can write our

*The flux per plaquette is given only by the difference in the tunneling phase between successive rows if the laser-assisted tunneling is along the rows. See earlier section on laser-assisted tunneling.

Hamiltonian as

$$\begin{aligned} \mathcal{H} = & - \sum_m \left(K e^{i\Phi/2} \hat{b}_{m+1}^\dagger \hat{b}_m + K e^{-i\Phi/2} \hat{b}_m^\dagger \hat{b}_{m+1} \right) && x\text{-tunneling in the bottom leg} \\ & + K e^{-i\Phi/2} \hat{a}_{m+1}^\dagger \hat{a}_m + K e^{i\Phi/2} \hat{a}_m^\dagger \hat{a}_{m+1} && x\text{-tunneling in the top leg} \\ & + J \hat{a}_m^\dagger \hat{b}_m + J \hat{b}_m^\dagger \hat{a}_m \right) && y\text{-tunneling.} \end{aligned}$$

SINGLE LEG We will first consider the top leg in isolation, which is achieved by considering only the first term in the preceding equation. At zero flux, this is simply a one-dimensional Bose-Hubbard system, for which, using a Fourier transformation, it is straightforward to show has a cosine dispersion (See §5.2 of Reference ⁵⁷). Here, we define momentum space operators, $\hat{\alpha}_k$ and $\hat{\alpha}_k^\dagger$, which instead of creating a particle at a particular lattice site, create a particle with a specific quasimomentum, k ,

$$\begin{aligned} \hat{a}_j &= \frac{1}{\sqrt{M}} \sum_k \hat{\alpha}_k e^{ikr_j}, & \hat{\alpha}_j &= \frac{1}{\sqrt{M}} \sum_j \alpha_k e^{ikr_j}, \\ \hat{a}_j^\dagger &= \frac{1}{\sqrt{M}} \sum_k \hat{\alpha}_k^\dagger e^{-ikr_j} & \hat{\alpha}_j^\dagger &= \frac{1}{\sqrt{M}} \sum_j \hat{\alpha}_k^\dagger e^{-ikr_j}, \end{aligned} \tag{5.3}$$

where M is the number of sites in the system, a is the lattice spacing, and $r_i = i \cdot a$ is the location of the i th site. Using this transformation, we find the eigenstates are states of definite quasimomentum with a cosine energy dependence on the quasimomentum,

$$\mathcal{H}_{\text{top leg}} = \sum_k \varepsilon(k) \alpha_k^\dagger \alpha_k, \quad \varepsilon(k) = 2K \cos(ka).$$

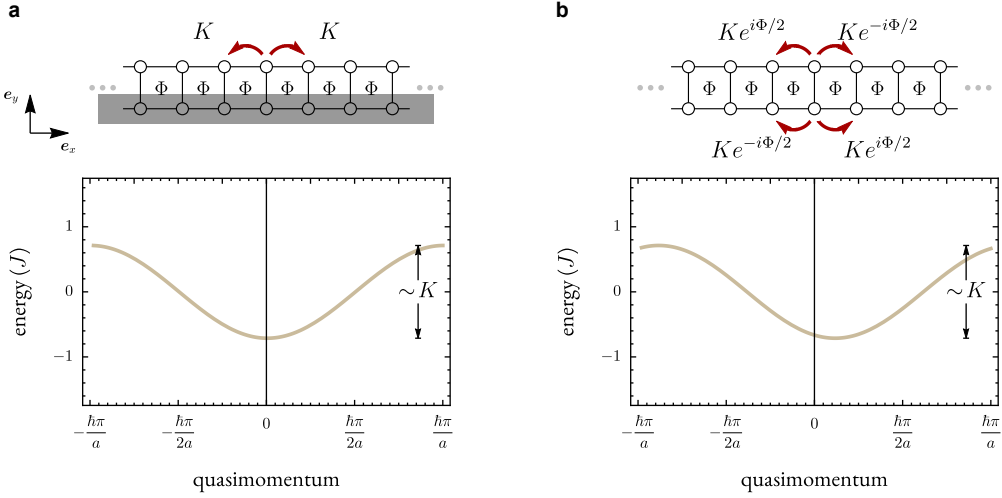


Figure 5.5: **a**, Band structure for an isolated leg of the ladder at zero flux. In the absence of flux, the Hamiltonian for a single leg of the ladder reduces to a Bose-Hubbard model, which exhibits a cosine dispersion. The peak-to-peak amplitude of the cosine is the bandwidth and is mathematically equivalent to the tunneling strength in the lattice. This band structure was computed for the parameters used in the single-particle experiments, $(J, K) = (29, 12.15)$ Hz. **b**, Band structure for two isolated legs of a Harper-Hofstadter ladder. In the presence of a magnetic field, the cosine dispersion of the Bose-Hubbard model is shifted in quasimomentum by a value proportional to the flux per plaquette Φ . For the two-leg ladder used in the single-particle experiments, we can choose a gauge such that the two cosine dispersions are shifted in opposite directions. The gray (blue) curve corresponds to eigenstates of the upper (lower) leg of the ladder.

In Figure 5.5a, we plot this cosine dispersion for the experimentally relevant parameters of $(J, K)/h = (29, 12.15)$ Hz.

For non-zero flux, the legs of our ladder differ from the Bose-Hubbard model in that the tunneling terms have a non-zero complex phase. This phase can be accounted for by shifting the dispersion in quasimomentum. We first define an expansion in the basis of on-site Fock states for a generic state $|\varphi_\alpha\rangle$,

$$|\varphi_\alpha\rangle = \sum_n c_n^{(\alpha)} a_n^\dagger |\text{vac}\rangle .$$

For the $c_n^{(\alpha)}$'s to define a wavefunction that is an eigenstate of the Bose-Hubbard Hamiltonian, they

must satisfy

$$-J_{\text{BH}} \left(c_{n-1}^{(\alpha)} + c_{n+1}^{(\alpha)} \right) = E_\alpha c_n^{(\alpha)} \quad (5.4)$$

due to the nearest neighbor tunneling J_{BH} of the Hamiltonian.

Now, we define $\tilde{c}_n^{(\alpha)}$ to be the expansion coefficients of the solutions to the Hamiltonian for the top leg of our Harper-Hofstadter ladder with energy \tilde{E}_α . By definition, an eigenstate will satisfy Schrödinger's equation,

$$\begin{aligned} \mathcal{H}_{\text{HH}} |\varphi_\alpha\rangle &= \tilde{E}_\alpha |\varphi_\alpha\rangle \\ -K \sum_n \left(e^{-i\Phi/2} a_{n+1}^\dagger a_n + e^{i\Phi/2} a_n^\dagger a_{n+1} \right) \sum_m \tilde{c}_m^{(\alpha)} a_m^\dagger |\text{vac}\rangle &= \tilde{E}_\alpha \sum_n \tilde{c}_n^{(\alpha)} a_n^\dagger |\text{vac}\rangle \\ -K \sum_n \left(e^{-i\Phi/2} \tilde{c}_n^{(\alpha)} a_{n+1}^\dagger + e^{i\Phi/2} \tilde{c}_{n+1}^{(\alpha)} a_n^\dagger \right) |\text{vac}\rangle &= \tilde{E}_\alpha \sum_n \tilde{c}_n^{(\alpha)} a_n^\dagger |\text{vac}\rangle \end{aligned}$$

We re-index the first term in the summation, $n \mapsto n - 1$.

$$-K \sum_n \left(e^{-i\Phi/2} \tilde{c}_{n-1}^{(\alpha)} a_n^\dagger + e^{i\Phi/2} \tilde{c}_{n+1}^{(\alpha)} a_n^\dagger \right) |\text{vac}\rangle = \tilde{E}_\alpha \sum_n \tilde{c}_n^{(\alpha)} a_n^\dagger |\text{vac}\rangle$$

Then we use the commutation relation of the creation operators, $[a_i, a_j^\dagger] = \delta_{ij}$, to project out the individual components.

$$\Rightarrow -K \left(e^{-i\Phi/2} \tilde{c}_{n-1}^{(\alpha)} + e^{i\Phi/2} \tilde{c}_{n+1}^{(\alpha)} \right) = \tilde{E}_\alpha \tilde{c}_n^{(\alpha)}$$

This equation is satisfied for $\tilde{c}_n^{(\alpha)} = e^{-in\Phi/2} c_n^{(\alpha)}$ where $c_n^{(\alpha)}$ are the components of the eigenstates for the 1D Bose-Hubbard Hamiltonian.

$$\begin{aligned} -K \left(e^{-i\Phi/2} c_{n-1}^{(\alpha)} e^{-i(n-1)\Phi/2} + e^{i\Phi/2} c_{n+1}^{(\alpha)} e^{-i(n+1)\Phi/2} \right) &= \tilde{E}_\alpha c_n^{(\alpha)} e^{-in\Phi/2} \\ -K \left(c_{n-1}^{(\alpha)} e^{-in\Phi/2} + c_{n+1}^{(\alpha)} e^{-in\Phi/2} \right) &= \tilde{E}_\alpha c_n^{(\alpha)} e^{-in\Phi/2} \\ -K \left(c_{n-1}^{(\alpha)} + c_{n+1}^{(\alpha)} \right) &= \tilde{E}_\alpha c_n^{(\alpha)}, \end{aligned}$$

which is satisfied by definition of $c_n^{(\alpha)}$ for $E_\alpha = \tilde{E}_\alpha$ and $J_{\text{BH}} = K$ (See Equation 5.4). This confirms that the wavefunction defined by $\tilde{c}_n^{(\alpha)} = e^{-in\Phi/2} c_n^{(\alpha)}$ is a solution with energy E_α for the top leg of the Harper-Hofstadter ladder, where $c_n^{(\alpha)}$ are expansion coefficients of any solution of the 1D Bose-Hubbard model. Physically, the transformation defined by $\tilde{c}_n^{(\alpha)} = e^{-in\Phi/2} c_n^{(\alpha)}$ represents a shift in the quasimomentum of the state defined by $c_n^{(\alpha)}$. Hence, the Harper-Hofstadter eigenstate spectrum can be obtained by simply shifting the Bose-Hubbard eigenstate spectrum by $\hbar\Phi/(2a)$.

That the two share the same set of eigenstates is not surprising — there is no notion of enclosing flux in a one-dimensional system, so the effective magnetic field should have no physical effect.

The analysis for the bottom leg is equivalent if we map $\Phi \mapsto -\Phi$. We represent both of these dispersions in Figure 5.5b where the grey (blue) curve corresponds to eigenstates of the upper (lower) leg. This is then the dispersion of the ladder system when the two legs are uncoupled, i.e. before we consider the effect of the coupling J along the rungs.

The last step is to incorporate the coupling along the rungs, which will couple the top-leg eigenstates to the bottom-leg eigenstates. As written, this coupling is between creation and annihilation

operators in real-space. In order to see how the coupling effects quasimomentum states, we perform the Fourier transformation defined in Equation 5.3,

$$\begin{aligned}
-J \sum_m (\hat{a}_m^\dagger \hat{b}_m + \text{h.c.}) &= -J \sum_m \left[\frac{1}{\sqrt{M}} \left(\sum_k e^{-ikr_m} \hat{a}_k^\dagger \right) \frac{1}{\sqrt{M}} \left(\sum_q e^{iqr_m} \hat{b}_q \right) + \text{h.c.} \right] \\
&= -J \sum_{kq} \sum_m \left(\frac{1}{M} e^{i(q-k)r_m} \hat{a}_k^\dagger \hat{b}_q + \text{h.c.} \right) \\
&= -J \sum_{kq} \left(\delta_{qk} \hat{a}_k^\dagger \hat{b}_q + \text{h.c.} \right) \\
&= -J \sum_k \left(\hat{a}_k^\dagger \hat{b}_k + \text{h.c.} \right).
\end{aligned}$$

The tunneling term only couples states of the same quasimomentum. Hence, at every quasimomentum, the band structure admits a two-level system with a Rabi coupling of strength J and detuning given by the energy separation between the dispersions of the top and bottom leg at that quasimomentum. At the location where the dispersions cross, i.e. $q = 0$, there is a resonant system resulting in dressed states that are symmetric and antisymmetric superpositions of the atom in the top and bottom leg. Elsewhere, the system is off-resonant and the dressed states are biased towards one leg in population. However, for $J > 0$, the lower (higher) energy dressed state always has a stronger overlap with the symmetric (antisymmetric) superposition.

In the limit that $J > K > 0$, the hybridization results in two sub-bands with non-zero width $\sim K$, split by an energy $\sim J$ (Figure 5.6). The eigenstates are plane wave states with quasimomentum q , running along the legs of the ladder where the rung subsystems define the unit cells of a one-dimensional lattice. The population of each site in the rung subsystems, color coded in Figure 5.6,

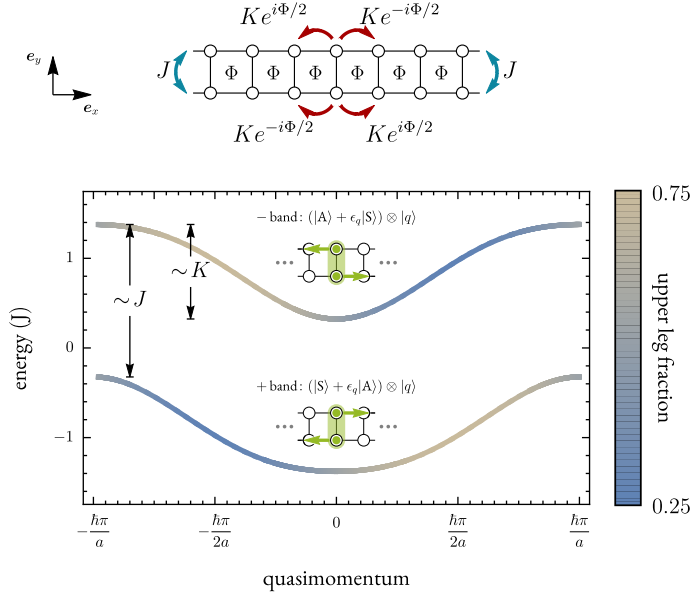


Figure 5.6: **a**, Band structure for the Harper-Hofstadter model in a $2 \times N$ ladder geometry computed for $(J, K) = (29, 12.15)$ Hz. The spectrum exhibits two bands, with the upper leg population fraction of each eigenstate encoded by color. In each band, there is a correlation between the sign of the group velocity and the leg towards which the particle is biased. However, the sign of the correlation differs between the two bands, giving rise to chiral bands of opposite sign, which we denote by $+$ and $-$. The chirality of each band is shown as an inset, where particles preferentially stick to one of the legs depending on the propagation direction. The initial state prepared in Figure 5.4b preferentially populates the lower band, resulting in chiral dynamics associated with that band.

depends on the quasimomentum of the eigenstate.

5.3 SINGLE-PARTICLE CHIRAL EIGENSTATES

We identify the two sub-bands in Figure 5.6 as $+$ or $-$ due to their symmetric and antisymmetric character in the unperturbed $K = 0$ limit. However, it is important to note that due to the non-zero flux $\Phi \neq 0$, the eigenstates of the band structure are not in general purely symmetric or anti-symmetric, i.e. leading to certain states more heavily populating, e.g., the top leg of the ladder. The

chiral character of the bands⁴⁷ emerges from a correlation between a particular eigenstate's population imbalance and its group velocity, $\partial_k \omega$. In the + band, a population imbalance towards the upper (lower) leg of the ladder is associated with a rightward (leftward) group velocity. This is exactly the correlation borne out in the propagation trajectories plotted in Figure 5.4b — y_{COM} for the right (left) half of system captures the population with positive (negative) group velocity and is biased towards the top (bottom) leg of the ladder.

Each eigenstate in the + band exhibits the same handed chiral behavior. An analogous analysis confirms that the eigenstates of the – band exhibit chirality of the opposite handedness. The chirality in the propagation dynamics of a state is the result of its decomposition between the two chiral sub-bands. The initial state shown in Figure 5.4a is a symmetric superposition between the top and bottom sites of the central rung. The symmetry of this state matches that of the + band and, hence, more heavily populates the + band, resulting in the chiral behavior associated with that band. The converse would occur for the initial state $\hat{a}_{0,\text{A}}^\dagger |\text{vac}\rangle$, resulting in chiral dynamics of opposite sign.

We can formalize this notion of chirality in the eigenstates. For an eigenstate with quasimomentum k in band τ , the chirality can be defined by

$$\mathcal{C}^\tau(k) = \text{sign}(v_g^\tau(k)) \times (p_U^\tau(k) - p_D^\tau(k)), \quad (5.5)$$

where $\text{sign}(v_g^\tau(k))$ denotes the sign of the group velocity $v_g^\tau(k) = \partial_k \omega_k^\tau$, and $p_{U,D}^\tau(k) = |u_{\tau,U}^{\text{U},\text{D}}(k)|^2$ are the probability amplitudes for a particle to reside on the upper (U) or lower (D) leg of the ladder. As an example, this chirality is shown color-coded in Figure 5.7 for magnetic field strengths of

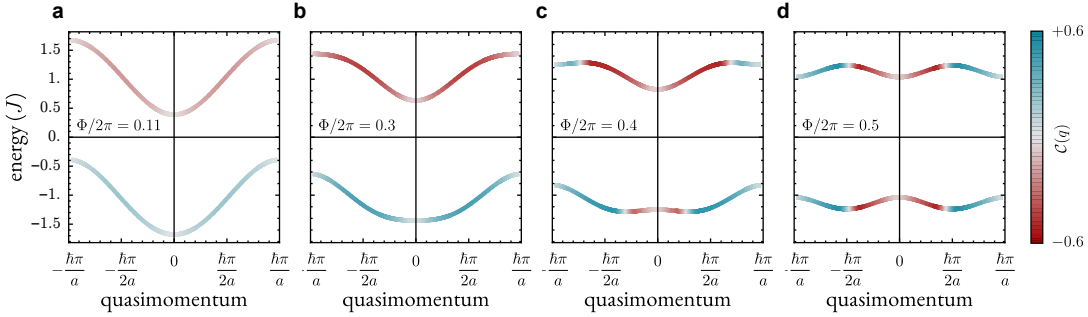


Figure 5.7: Chirality of Bloch bands: The dispersion relations $\epsilon_{\pm}(q)$ of the two Bloch bands (lower, +, and upper, -) are plotted, for $J = 2\pi \times 34.1$ Hz and $K = 2\pi \times 11.4$ Hz close to the experimental values. The color code indicates the chiralities $C^{\pm}(q)$ of the two bands, determined by Eq. (5.5). Different values of Φ are considered: **a**, $0.11 \times 2\pi$, **b**, $0.3 \times 2\pi$, **c**, $0.4 \times 2\pi$, and **d**, $0.5 \times 2\pi$.

$\Phi/2\pi = 0.11, 0.3, 0.4, 0.5$. Figure 5.7**a-b** are in the experimentally relevant regime where each sub-band contains states of only a single chirality. For stronger magnetic fields, as shown in Figure 5.7**c-d**, the minimum in each sub-band bifurcates, resulting in eigenstates with opposite chirality within the same sub-band.

Having developed the chiral band structure, we can understand qualitatively the time evolution of various initial states by studying their decomposition into the chiral eigenstates. In Figure 5.8, the decomposition is plotted for a variety of initial states. The first column (**a** and **d**) pertains to symmetric, $\hat{a}_S^\dagger |vac\rangle$, and antisymmetric, $\hat{a}_A^\dagger |vac\rangle$, delocalizations. As suggested by the symmetry of these states, they mostly project onto one of the two chiral bands, which explains the chirality in their propagation dynamics. However, both of these initial states exhibits a small admixture of population in the band of opposite chirality. This admixture is what leads to the oscillations in y_{COM} shown in Figure 5.4**b**. In contrast, the initial states shown in panels **b-c** and **e-f** have equal overlap with both chiral bands and thus we do not expect any chiral dynamics in their propagations.

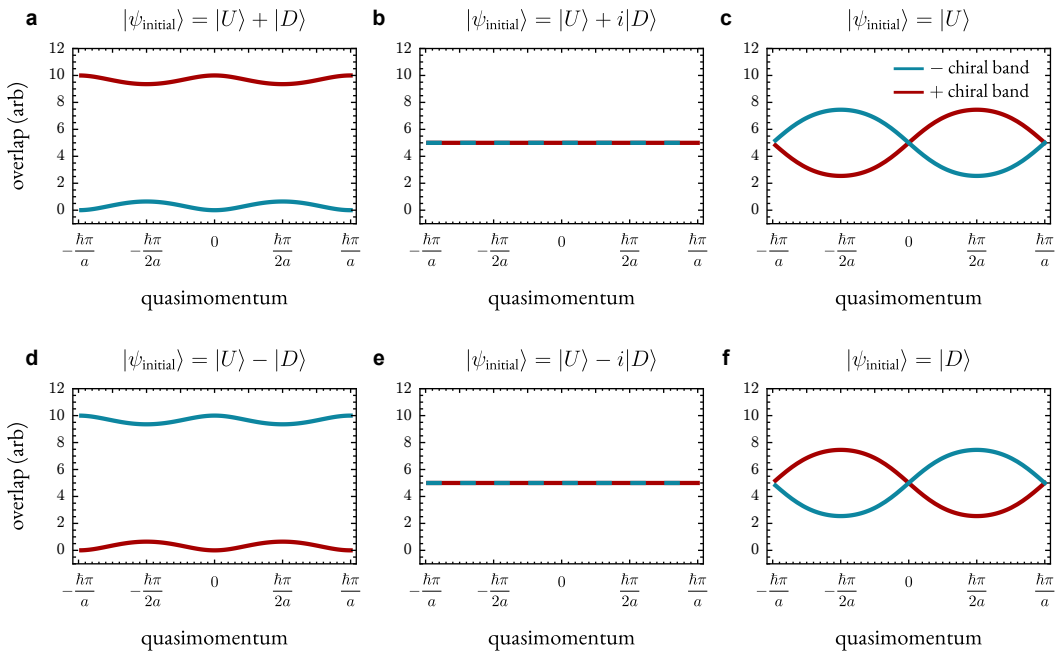


Figure 5.8: Projection on to energy eigenstates for a selection of initial states. The two-particle Harper-Hofstadter ladder exhibits two sub-bands of opposite chirality. The chirality of an initial state's propagation dynamics is a manifestation of the that initial state's population distribution in the sub-bands. Symmetric and antisymmetric delocalizations (**a** and **b**) exhibit chirality due to their imbalanced populations in the two sub-bands whereas the states shown in **b-c** and **e** and **f** equally populate both sub-bands, leading to achiral propagation.

5.4 INTERACTION-INDUCED CHIRALITY

When the ladder system contains multiple particles, we must consider the effects of interactions. In this section, we study a building block of larger interacting systems by considering a system of two particles. Even in the two-particle limit explored by these experiments, we find complexity in the underlying physics associated with the synergy of interactions and gauge fields.

As in the previous sections, our tool for studying these systems will be the quantum walk. We consider the initial state consisting of a pair of bosons on the two neighboring sites of the central rung,

$$|\psi_{\text{initial}}\rangle_{2p} = a_{0,1}^\dagger a_{0,0}^\dagger |\text{vac}\rangle.$$

We study the propagation dynamics using the center-of-mass of the density distribution and compare the propagation for leftward versus rightward moving population. As shown in Figure 5.9, we observe clear chiral orbits as the particles evolve from $|\psi_{\text{initial}}\rangle_{2p}$ — population is biased towards opposite legs of the ladder depending upon which direction it propagates.

The chirality we observe in these orbits is a direct result of the applied gauge field. The tunability afforded by our apparatus (See §2.2 for technical details) allows us to study the dependence of this effect on the magnetic field strength. In Figure 5.10a, we observe chiral propagation for $\Phi = 0.47\pi$. When the sign of the magnetic field is flipped, we find identical dynamics, but with opposite sign (Figure 5.10b). The antisymmetry of these measurements suggests that chirality should be absent at zero field strength. Indeed, when the magnetic field strength is set to zero, chirality is no longer

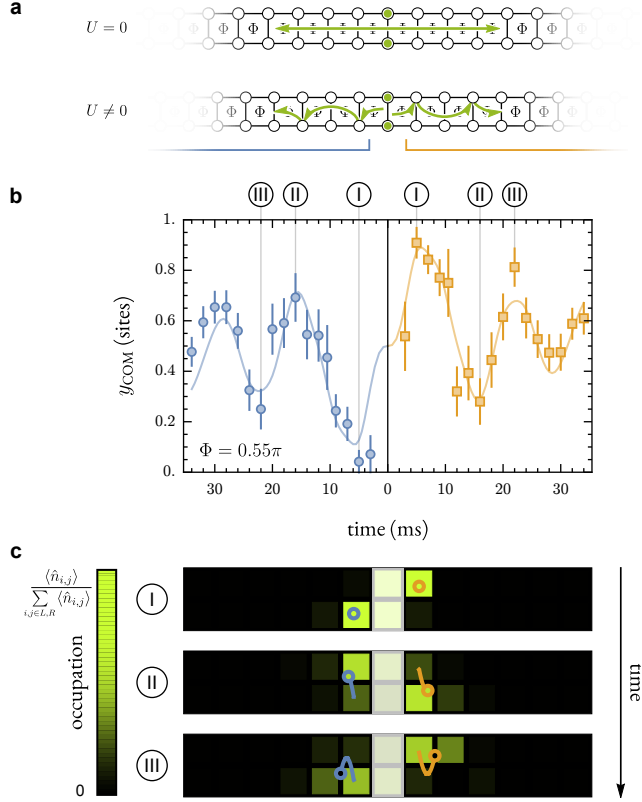


Figure 5.9: **a**, We initialize a pair of particles onto opposite sites of the central rung and track the density distribution in the presence of a gauge field. The interactions give rise to chirality in the propagation dynamics. **b**, Chirality manifests in the difference in y_{COM} for the left (blue) and right (orange) halves of the system. The solid line results from an exact diagonalization at $\Phi = 0.55\pi$ and $\{U, J, K\}/h = \{131.2(6), 34.1(6), 11(1)\}$ Hz. **c**, Exemplary density distributions for times indicated in **a**. The saturation of a square indicates the occupation probability of that lattice site normalized to the population in its half of the system, left or right. Blue and orange circles indicate the position of the center-of-mass for the left and right halves, respectively. Solid lines trace the evolution of the center-of-mass up to the point of measurement.

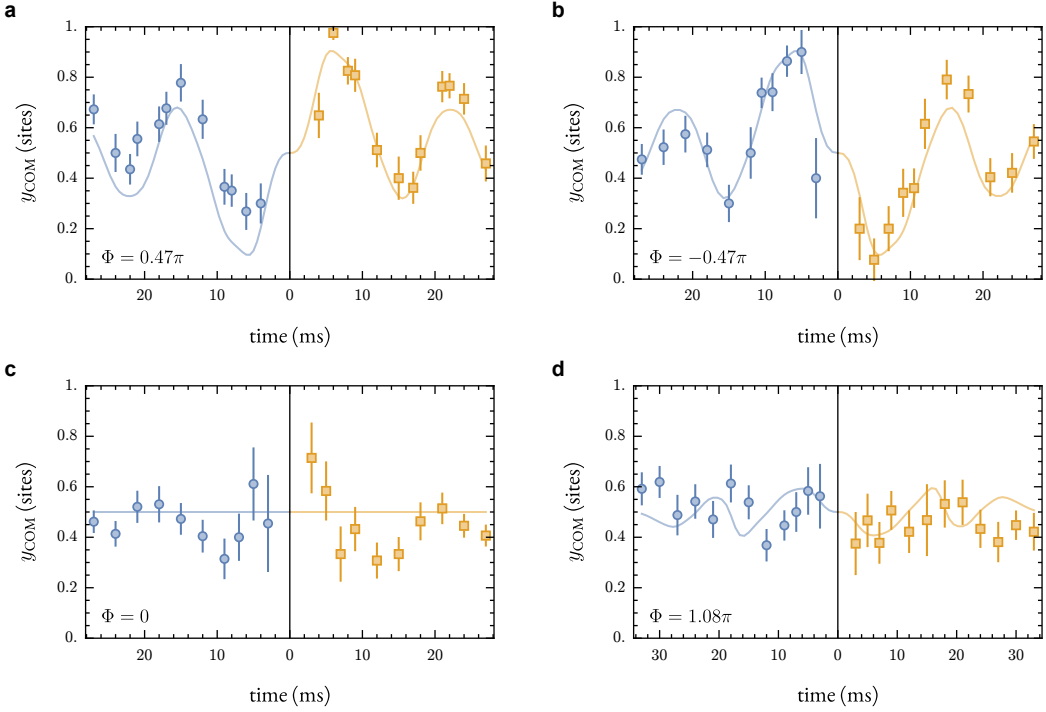


Figure 5.10: Two-particle dynamics at multiple flux values: We investigate the dynamics y_{COM} for additional flux values. We observe the reversing of chirality as the direction of the magnetic field is reversed. Additionally, we observe the disappearance of chiral propagation for flux values $\Phi \approx 0$ and $\Phi \approx \pi$.

present in the propagation. Additionally, propagation has no leftward versus rightward asymmetry when the flux $\Phi \approx \pi$, which is a field strength for which even in larger systems there is no topology (See §1.3.2 for an alternative argument for triviality of $\Phi = \pi$). In Figure 5.11, we map out the complete dependence on the magnetic field for the shearing amplitude, Δy_{COM} , of the first oscillation, which is at roughly $t = 7.2$ ms. We see that the chirality observed is present in the two-particle trajectories whenever the applied flux induces chirality in the single-particle bands, specifically, when the flux Φ is neither zero nor π .

In addition to the applied gauge field, the on-site interactions are also critical to the observed

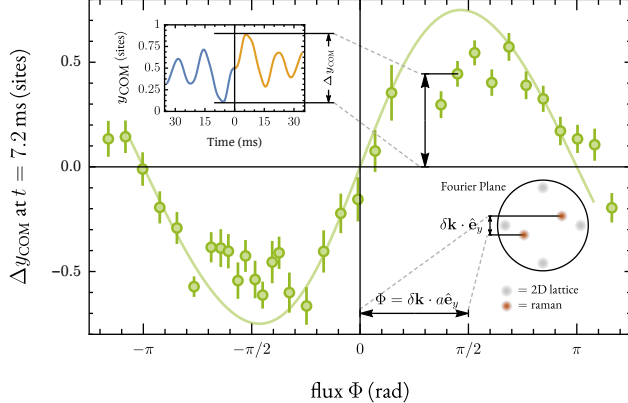


Figure 5.11: We quantify the amount of chirality by the shearing at $t = 7.2$ ms, corresponding roughly to the first maxima in the center-of-mass evolution (inset). Our data shows that chirality is absent for the case of zero flux when the gauge field is switched off, as well as at π flux, highlighting the role of the gauge field in the chiral dynamics.

trajectories. We can express the initial state $|\psi_{\text{initial}}\rangle_{2p}$ in terms of the single-particle states discussed

in the prior section as

$$|\psi_{\text{initial}}\rangle_{2p} = a_{0,1}^\dagger a_{0,0}^\dagger |\text{vac}\rangle = \frac{1}{\sqrt{2}}((a_{0,S}^\dagger)^2 - (a_{0,A}^\dagger)^2)|\text{vac}\rangle.$$

The initial state has an equal population in symmetric and antisymmetric superpositions. The single-particle band structure (Figure 5.4c) derived in the previous section indicates that these superpositions populate eigenstates of opposite chirality. Our initial state has an equal weight in single-particle bands of opposite chirality and in the non-interacting case, these weights are preserved in time since the non-interacting eigenstates are products of the single-particle eigenstates. Hence, even in the presence of a gauge field, such a state should not exhibit any chirality in the non-interacting limit.

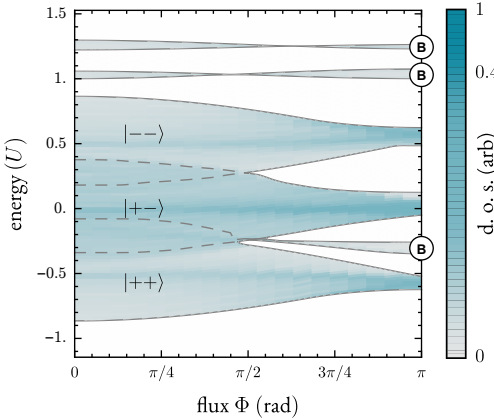


Figure 5.12: Density of states for two-particle system: We plot the density of states as a function of energy of per plaquette Φ . The regions without states are left white. Gray boundary lines are enclose the regions with states. This spectrum exhibits both bound states (labeled with \textcircled{B}) and scattering states (labeled $|\tau_1, \tau_2\rangle$), where $\tau_i = \pm$.

5.5 TWO-PARTICLE EIGENSTATES

The chiral dynamics we observe in Figure 5.9 depend on both interparticle interactions and the applied synthetic gauge field. To understand the single-particle quantum walks, we focused on the energy eigenstates and developed the band structure of the system. Those eigenstates are no longer stationary in the presence of interactions and so we turn to the eigenstates of the two-particle system to explain the chirality in the quantum walks.

Two broad classes emerge in the spectrum of two-particle eigenstates: scattering states, which can be approximated by product states of the single-particle eigenstates, and bound states, which are repulsively bound and carry a large effective mass. These states are sorted by energy in Figure 5.12 and plotted for flux values of $\Phi = 0$ to $\Phi = \pi/2$. In this work, the flux is not varied over the course of any single experiment. Hence, only a single vertical slice is relevant for a given experiment.

The grayscale level indicates the density of states with the white regions corresponding to energies and fluxes for which eigenstates do not exist. For visual clarity, the data is binned such that each bin contains approximately 10 neighboring eigenstates. In addition, solid gray lines are used to clearly separate the regions with and without any eigenstates.

The scattering states have an associated chirality and the observed two-particle chirality relies on interactions to bias the populating of these chiral eigenstates. We observe evidence in the two-particle quantum walks that the observed chirality is largely a result of this chirality in the scattering states, rather than an effect from the bound states. The bound states are long-lived and their population depends on the flux per plaquette. This flux dependence is also evident in the two-particle quantum walks. In Figure 5.12, the bands of bound states are labeled with a \textcircled{B} .

5.5.1 SCATTERING STATES

The scattering states are located in the three broad bands of eigenstates labeled $|++\rangle$, $|+-\rangle$, and $|-+\rangle$. These states are very similar to the states of free bosons, i.e. the chiral eigenstates composing the single-particle band structure (see §5.2). We describe these states as scattering states because the two bosons are likely to be far away from each other. In this case, their wavefunction can be well approximated by two independent plain waves $\hat{a}_{k_1, \tau_1}^\dagger \hat{a}_{k_2, \tau_2}^\dagger |\text{vac}\rangle$, where the operator $\hat{a}_{k, \tau}^\dagger$ creates a boson at quasimomentum k in the single-particle band labeled by $\tau = \pm$. Each two-particle band of scattering states is primarily composed of states with the same pair of single-particle band indices, which are expressed in the labels $|\tau_1, \tau_2\rangle$ shown in Figure 5.12 .

This classification by single-particle band indices can be verified by expanding the two-particle

eigenstates in product states of the single-particle states. For a two-particle eigenstate $|\phi_n\rangle$, we can write

$$|\phi_n\rangle = \sum_{k_1, k_2} \left[\frac{1}{\sqrt{2}} \phi_n^{++}(k_1, k_2) \hat{a}_{k_1,+}^\dagger \hat{a}_{k_2,+}^\dagger + \frac{1}{\sqrt{2}} \phi_n^{--}(k_1, k_2) \hat{a}_{k_1,-}^\dagger \hat{a}_{k_2,-}^\dagger + \phi_n^{+-}(k_1, k_2) \hat{a}_{k_1,+}^\dagger \hat{a}_{k_2,-}^\dagger \right] |\text{vac}\rangle, \quad (5.6)$$

where the expansion coefficient $\phi_n^{++}(k_1, k_2) = \phi_n^{++}(k_2, k_1)$ is symmetric (and analogously for ϕ_n^{--}). The summation over quasimomenta k_1 and k_2 at fixed single-particle band indices τ_1 and τ_2 of the expansion coefficients,

$$p_{\tau_1, \tau_2}(n) = \sum_{k_1, k_2} |\phi_n^{\tau_1 \tau_2}(k_1, k_2)|^2, \quad (5.7)$$

gives us the overlap of the two-particle eigenstates with a particular pair of single-particle bands. In Figure 5.13a, we plot $p_{++}(n)$ as a function of the flux per plaquette Φ of the synthetic gauge field and the eigenenergy. We use the same binning method for $p_{++}(n)$ as was used for Figure 5.12. The strong overlap indicated by the summation over expansion coefficients confirms that $|++\rangle$ is an appropriate label for that broad band of two-particle eigenstates. In Figures 5.13b and c, we repeat this calculation for $p_{--}(n)$ and $p_{+-}(n)$ defined using $|\phi_n^{--}|^2$ and $|\phi_n^{+-}|^2$, which similarly confirms the labels $|--\rangle$ and $|+-\rangle$, respectively.

The energetic distribution of each of the two-particle scattering bands follows readily from its constituent single-particle bands. For each single-particle band, we define ε_τ^{\min} and ε_τ^{\max} as the min-

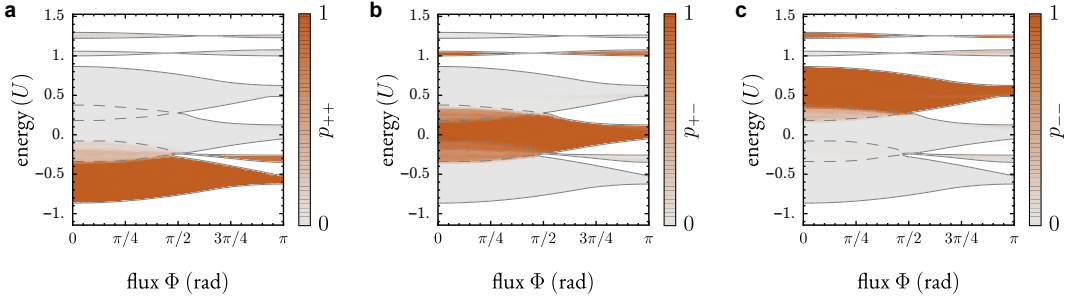


Figure 5.13: Decomposition of interacting eigenstates into free two-particle eigenstates: **a**, The overlap $p_{++}(n)$ is shown (color code) as a function of the eigenenergies E_n and the flux Φ per plaquette of the synthetic gauge field, see Equation (5.7). In **b** and **c**, the calculation is repeated for p_{+-} and p_{--} respectively.

imum and maximum eigenenergies for a given band $\tau = \pm$. The eigenstates of the two-particle scattering band $|++\rangle$ can be roughly approximated by a symmetrized product state composed of two states from the band $\tau = +$. The maximum (minimum) possible energy of such a product state is then given by $2 \times \varepsilon_+^{\max}$ ($2 \times \varepsilon_+^{\min}$). These energies approximate the solid line boundaries drawn for the $|++\rangle$ scattering band. As the flux is increased, the single-particle bands flatten and thus the difference $\varepsilon_\tau^{\max} - \varepsilon_\tau^{\min}$ decreases. This flattening manifests in the two-particle eigenspectrum as a narrowing of the $|++\rangle$ two-particle scattering band with increasing flux. An analogous analysis of the $(+, -)$ and $(-, -)$ pairs of single-particle bands is sufficient for qualitatively describing the energies of their respective two-particle scattering bands.

Given the close resemblance between the two-particle scattering states and product states of the single-particle eigenstates, it is reasonable to generalize the chirality first introduced in §5.2 to two-particle eigenstates. Using the expansion coefficients defined through Equation 5.6, we define the

chirality, \mathcal{C}_n , of a two-particle eigenstate $|\phi_n\rangle$ with the following

$$\begin{aligned} \mathcal{C}_n = \sum_{k_1, k_2} & \left[|\phi_n^{++}(k_1, k_2)|^2 (\mathcal{C}^+(k_1) + \mathcal{C}^+(k_2)) \right. \\ & + |\phi_n^{--}(k_1, k_2)|^2 (\mathcal{C}^-(k_1) + \mathcal{C}^-(k_2)) \\ & \left. + |\phi_n^{+-}(k_1, k_2)|^2 (\mathcal{C}^+(k_1) + \mathcal{C}^-(k_2)) \right]. \quad (5.8) \end{aligned}$$

In Figure 5.15b, we plot \mathcal{C}_n as a function of the eigenenergies and the synthetic magnetic field, using the binning method described earlier.

5.5.2 BOUND STATES

In addition to the scattering states, we find three narrow bands of bound states in Figure 5.13a - c corresponding to repulsively bound pairs with a large effective mass. Unlike the scattering states, these states have energy scales that do not correspond to the single-particle band energies, ε_τ^{\max} and ε_τ^{\min} . Instead, we find these bound states located at energies related to the interaction and superexchange energies, i.e. $U + J_{\text{ex}}$, U , and $-J_{\text{ex}}$. The energetically lowest branch mostly consists of particles in the lowest (+) band. The two upper branches, with energy $\sim U$, mostly correspond to one boson in each band and two bosons in the – band, respectively.

5.6 TWO-PARTICLE CHIRALITY

Since the bosons in our initial state are close to each other, we expect that there can be sizable overlaps with both types of eigenstates for our experimental parameters. The bound states are repulsively bound to either the same site or the same rung. Hence, the physically observable probability P_{11} for two bosons to occupy the same rung anywhere in the system gives us an experimental measure for the bound state fraction in our system. In Figure 5.14a, we plot this quantity as a function of time and gauge field strength. Indeed, even at long times we find a sizable, flux-dependent probability for the bosons to remain close to each other, consistent with the presence of a bound state.

The large effective mass of these bound states is apparent in both the density distributions and the temporal dynamics of the x center-of-mass. In Figure ??a, the density distribution integrated along the y axis following 22 ms of evolution in the ladder is plotted. The same density distribution for a single particle is shown for comparison. The slower tunneling of the repulsively bound state is apparent in the slow spreading of the wavefunction density. In addition, the temporal dynamics of x_{COM} is plotted in Figure ??b, which exhibits substantially slower propagation than would be expected from the tunneling rates alone.

In contrast to the bound states which manifest in atoms occupying the same rung, the scattering states are not energetically detuned from separating. Also unlike the bound states, we expect these states to contribute most to the chiral signature. To support this claim, we study the shearing amplitude (as in Figure 5.11) as a function of the inter-particle distance. At long times, we expect the population in eigenstates of largely free-particle (bound) character to yield atoms that are farther

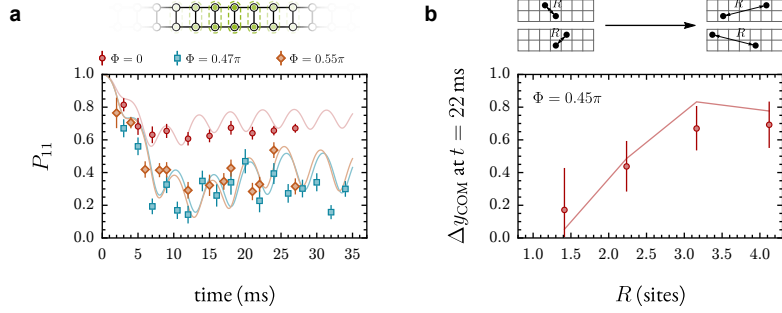


Figure 5.14: The interacting two-particle dynamics give rise to both bound states and scattering states, the interplay of which leads to chirality. **a**, We plot the probability P_{11} that the particles are on different sites of the same rung as a function of time and flux; this quantity provides a measure of the population in the lowest energy bound state (see panel d). The dynamics in P_{11} are shown for fluxes of $\Phi = 0$, $\Phi = 0.47\pi$, and $\Phi = 0.55\pi$. **b**, The degree of shearing, Δy_{COM} , following 22 ms of evolution in the ladder is plotted as a function of the inter-particle spacing, i.e. the average Δy_{COM} when the atoms are a distance R apart. The shearing, a proxy for the chirality, suggests that the scattering states where particles are further separated contribute most to the chirality.

apart (closer together). We find that the shearing increases for bosons farther apart (Figure 5.14b), suggesting that the populated, unbound scattering states contribute most to the observed chirality. This implies that there is an imbalance in the populations of $|++\rangle$ and $|--\rangle$ states, which are of opposite chirality. Given the stationary and equal population of the chiral bands in the non-interacting case, the imbalance in these observed dynamics must be induced by the interactions. We confirm this conclusion by calculating numerically the overlaps of our initial state, $|\psi_{\text{initial}}\rangle$, with the eigenstates of the full interacting Hamiltonian, $|\phi_n\rangle$,

$$|\psi_{\text{initial}}\rangle = \sum_n c_n |\phi_n\rangle .$$

In Figure 5.15a, we first show[†] the squared amplitudes $|c_n|^2$ plotted against the corresponding

[†]The data is binned such that each bin contains about 10 neighboring eigenstates and the bin's value is the sum of $|c_n|^2$ for all the constituent eigenstates.

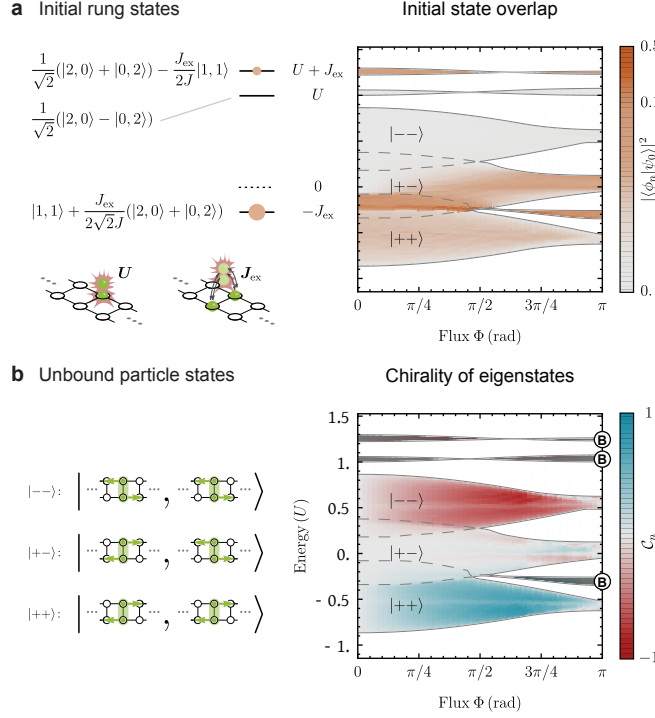


Figure 5.15: **a**, We show (left) the population of the eigenstates of a given rung in the $K = 0$ limit and (right) the full many-body spectrum as a function of flux Φ , given the calibrated J , K , and U . In the latter, the color encodes the overlap between our initial state and these many-body eigenstates as a function of Φ , where the boundaries of the different eigenstate regions of interest are differentiated by the gray lines. The regions enclosing $|- \rangle$, $|+ - \rangle$, and $|+ + \rangle$ are then largely described by product states of the unbound eigenstates. **b**, Chiral character of the many-body eigenstates. The + and - labels describe what single-particle bands mostly describe the colored bands in this plot. The color denotes the chirality, C_n , of the eigenstates within the bands and the dark gray regions refer to the eigenstates that compose the bound states in the ladder system.

eigenenergies E_n as a function of the flux Φ . Because the squared amplitudes $|c_n|^2$ are conserved in

the dynamics, this decomposition allows us to understand the behavior of the system at long times.

In Figure 5.15b, we plot the associated chirality, C_n of the two-particle eigenstates, $|\phi_n\rangle$. Clearly evident is a heavier overlap with eigenstates in the $|+ + \rangle$ sector as compared to the $|- \rangle$ section.

To illustrate the physical process by which interactions induce a population imbalance between $(|+ + \rangle)$ and upper $(|- \rangle)$ scattering states, we analyze the eigenstates of two interacting bosons on

the central rung and study how they hybridize with delocalized states as the tunnel coupling K is introduced. In the limit $U \gg J$, two of the three two-boson eigenstates involve double occupancy of one site, causing an energy shift of order U (Figure 5.15a). These states are largely detuned from the delocalized states and do not influence the dynamics. There is a third eigenstate near zero energy, with large overlap to our initial state. Due to the finite J and U , this eigenstate is shifted down in energy by $J_{\text{ex}} = 4J^2/U$ through a super-exchange process (Figure 5.15a). For $U = 0$, the tunnel coupling K along the legs hybridizes this rung eigenstate equally with states $|--\rangle$ and $|++\rangle$. However, because of the downward energy shift of J_{ex} for $U \neq 0$, the state is energetically closer to $|++\rangle$ states and hybridizes primarily with this chiral band (Figure 5.15a). The interactions also create a delocalized bound state when $J_{\text{ex}} \sim K$, corresponding to a particle on each site of a rung somewhere in the system, which is reflected by the non-vanishing P_{11} . Lastly, as the magnetic flux Φ is increased, the motion of the particles in the x and y directions becomes increasingly coupled by the gauge field, leading to additional hybridization with the $|+-\rangle$ states (Figure 5.15a). This effect is also in agreement with the observed reduction of P_{11} at long times when introducing the gauge field (Figure 5.14a), because we expect an increase in the size of the bound state caused by the coupled motion in the x and y direction.

The combined effect of interactions and a synthetic gauge field is necessary to explain our observation of chirality in the multi-particle dynamics of bosons in a $2 \times N$ ladder. Our observations depend on being in a regime where the interactions are neither vanishing nor infinite — in either of these limiting cases, there is no exchange-energy shift J_{ex} , leading to symmetric populations in the two chiral sectors.

5.7 SHORT-TIME PERTURBATION THEORY OF THE INTERACTING PROPAGATION DYNAMICS

ICS

For short times, the chiral propagation dynamics can also be described analytically. A short-time perturbative expansion shows that

$$y_{\text{COM}}(t) = \pm a(t/\hbar)^5 (KJ)^2 U \sin(\Phi)$$

to leading order in the evolution time t for the right (+) and left (−) side of the ladder, indicating that the dynamics depend both on the flux per plaquette Φ and the interaction energy U .

We compute $\langle \hat{n}_{i,1} - \hat{n}_{i,0} \rangle$ for the initial state $|\psi(t)\rangle = a_{0,1}^\dagger a_{0,0}^\dagger |\text{vac}\rangle$, where $i = 0$ is the center of the ladder. Using the Hamiltonian in Equation 5.1 and $|\psi(t)\rangle = e^{-i\mathcal{H}t/\hbar} a_{0,1}^\dagger a_{0,0}^\dagger |\text{vac}\rangle$, we Taylor expand in t (valid for $t \ll \frac{\hbar}{\max(J,K,U)}$) and compute $\langle \hat{n}_{i,1} - \hat{n}_{i,0} \rangle$. As expected, when $i = 0$, $\langle \hat{n}_{0,1} - \hat{n}_{0,0} \rangle = 0$. Then, for $i = 1$, the relevant non-vanishing terms in $|\psi(t)\rangle$ are

$$\begin{aligned} |\psi(t)\rangle &= \dots - \frac{1}{2!} \left(\frac{t}{\hbar} \right)^2 \left[2JK \left(\left(e^{-i\Phi/2} + \cos \left(\frac{\Phi}{2} \right) \right) a_{1,0}^\dagger a_{0,0}^\dagger \right. \right. \\ &\quad \left. \left. + \left(e^{i\Phi/2} + \cos \left(\frac{\Phi}{2} \right) \right) a_{1,1}^\dagger a_{0,1}^\dagger \right) \right] |\text{vac}\rangle \\ &\quad + \frac{1}{3!} i \left(\frac{t}{\hbar} \right)^3 \left[2JKU (e^{i\Phi/2} a_{1,1}^\dagger a_{0,1}^\dagger + e^{-i\Phi/2} a_{1,0}^\dagger a_{0,0}^\dagger) \right] |\text{vac}\rangle, \end{aligned} \quad (5.9)$$

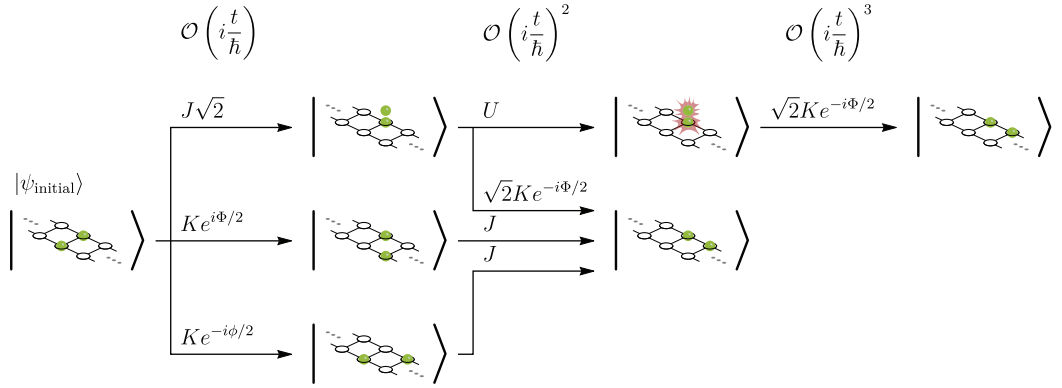


Figure 5.16: Illustration of the leading-order terms contributing to the short-time perturbative expansion: The $\mathcal{O}\left(i \frac{t}{\hbar}\right)^2$ paths interfere with the $\mathcal{O}\left(i \frac{t}{\hbar}\right)^3$ path including on-site interactions on the upper leg of the ladder. An equivalent set of interfering paths, with the upper and lower legs exchanged, leads to the leading-order non-vanishing chiral signal scaling like $U t^5 \sin \Phi$, as described in the text.

as illustrated in Figure 5.16. This yields ($i = -1$ is similar)

$$\langle \hat{n}_{1,1} - \hat{n}_{1,0} \rangle = - \langle \hat{n}_{-1,1} - \hat{n}_{-1,0} \rangle = t^5 \left(\frac{U}{\hbar}\right) \left(\frac{KJ}{\hbar^2}\right)^2 \sin(\Phi). \quad (5.10)$$

The odd dependence on the flux, Φ , arising from the on-site interaction occurring on the top versus the bottom leg, indicates that the effect is chiral. For small t , Figure 5.17 shows good agreement between equation 5.10 and numerical results, convincingly showing a t^5 dependence. In the $U \rightarrow \infty$ limit, we recompute the short-time expansion with hard-core bosons, and notice the non-vanishing terms in equation 5.9 require the asymmetry of the particles interacting on the top versus the bottom legs of the ladder. Such a case is not possible in the hard-core boson limit, and up to order t^5 , all terms vanish.

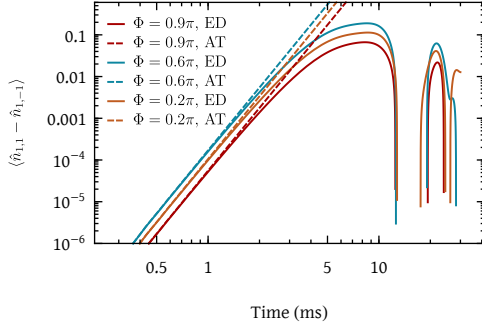


Figure 5.17: Log plot of both the analytical theory (AT) result $\langle \hat{n}_{1,1} - \hat{n}_{1,0} \rangle = t^5 \left(\frac{U}{\hbar}\right) \left(\frac{KJ}{\hbar^2}\right)^2 \sin(\Phi)$, which can be obtained using a short-time expansion, and the numerical results obtained from exact diagonalization (ED) for different flux values Φ . Note the strong agreement for $t \lesssim 1$ ms at all flux and the clear t^5 dependence.

5.8 CONCLUSION

We combined two workhorse techniques of atomic physics, artificial gauge fields and quantum gas microscopy, to perform the first microscopic studies of an interacting Harper-Hofstadter system. The exquisite quantum control afforded by this apparatus gives us the unique ability to create chiral matter from the bottom-up. First, we studied the propagation of a single particle in a $2 \times N$ ladder through the time evolution of the center-of-mass of the density distribution. We found that, in the presence of an artificial gauge field, the population experiences a direction-dependent deflection analogous to a classical Lorentz force. The resulting chirality is a signature of the underlying chiral band structure, which contains two sub-bands of opposite chirality. This description gives us a tool for understanding the character of the propagation of arbitrary initial states.

Having developed the single-particle eigenstates, we looked at the effect of interactions on such a system by looking at an initial state consisting of a pair of atoms initialized to opposite sites of

a single rung. We observed a chirality in the propagation dynamics that depends crucially upon both the applied gauge field and the presence of interactions. In explaining this interaction-induced chirality, we investigated the two-particle eigenstate spectrum, which contains scattering states and bound states. Our data suggests that the scattering states are primarily responsible for the observed chirality. By generalizing the chiral framework of the single-particle eigenstates to the interacting eigenstates, we explained the observed chirality in terms of an imbalance in the population of two-particle chiral scattering states caused by a superexchange energy shift in the initial state.

Residing in such a regime where interactions and the gauge field work in concert is crucial to studying strongly-correlated chiral matter, such as chiral Mott insulators and fractional quantum Hall states. The technical achievements developed herein and summarized below are instrumental towards reaching these goals.

COMBINING GAUGE FIELDS AND MICROSCOPY. Introducing microscopy to systems under the influence of a gauge field was essential to our studies of the Harper-Hofstadter model and establishes future opportunities. For our observations, microscopic control was required to prepare low-entropy states in which to controllably include interactions and microscopic detection was key to the characterization of the physics. For the future, microscopy can be used for spatially resolved detection of edge state phenomena (as we observe here) in larger systems, local spectroscopy to see a gapped bulk and gapless edge in a Chern insulator, and projection of optical potentials with feature sizes at the scale of a lattice site. The ability to project high resolution potentials is a powerful tool for creating arbitrary confinement geometries and is the basis of anyonic statistics detection proto-

cols⁷⁴.

TWO-DIMENSIONAL, CUSTOM, REAL-SPACE FINITE LATTICES We study a real-space, bounded lattice system under the influence of a gauge field, where individual particles pick up a geometric phase upon traversing closed loops in real space. Our use of a real-space lattice allows us to achieve isotropic interactions in a scalable, versatile geometry, drawing a close analogy to the condensed matter systems in which this exotic physics was discovered.

A TUNABLE FLUX IN REAL-SPACE. We demonstrate the ability to tune the real-space magnetic flux threaded through the system, in principle dynamically. This capability can be leveraged for ground-state preparation of correlated states. As was shown via rotation³⁴, the ability to dynamically ramp on a magnetic field, thereby introducing angular momentum into the system, can be used to prepare a Laughlin state.

This successful integration of demonstrated, new, and repurposed techniques was essential to the first observations of low-entropy, interacting, chiral quantum states. Furthermore, the demonstrated toolset establishes the viability of our approach for further studies of chiral many-body states.

A

Atomic Physics

A.1 TWO-LEVEL ATOM

Based upon conventions in Daniel Steck's Quantum Optics Notes and Rubidium⁸⁷ numbers. A time-varying electric field $\mathbf{E}(t)$ with polarization $\hat{\varepsilon}$ can be written

$$\mathbf{E}(t) = \hat{\varepsilon} E_0 \cos(\omega t)$$

$$\mathbf{E}(t) \equiv \mathbf{E}_0^{(+)} e^{-i\omega t} + \mathbf{E}_0^{(-)} e^{i\omega t}$$

$$\mathbf{E}(t) \equiv \mathbf{E}_0^{(+)}(t) + \mathbf{E}_0^{(-)}(t)$$

The field interacts with an atom through the dipole interaction,

$$H_{\text{AF}} = -\mathbf{d} \cdot \mathbf{E}, \quad \mathbf{d} = -e\mathbf{r}_e,$$

where \mathbf{r}_e is the electron's position. In the limit of the *slowly-varying envelope approximation*^{*}, the complete Hamiltonian of the system takes the form,

$$\mathcal{H} = \hbar\omega_{12}|2\rangle\langle 2| - (\mathcal{E}(r, t)e^{-i\nu t} + \mathcal{E}^*(r, t)e^{i\nu t}) (\mu_{12}|1\rangle\langle 2| + \mu_{21}|2\rangle\langle 1|),$$

where we have expanded the dipole operator in terms of $|i\rangle\langle j|$ so that $\mu_{ij} = \langle i|\hat{\varepsilon} \cdot \mathbf{d}|j\rangle$. We transform to a rotating frame using the unitary transformation $U = \exp(-i\nu|2\rangle\langle 2|t)$, which takes $|\psi\rangle = U|\psi_{\text{RF}}\rangle$. Schrödinger's Equation for the state vector in the original frame is,

$$\begin{aligned} \frac{\partial}{\partial t}|\psi\rangle &= -\frac{i}{\hbar}\mathcal{H}|\psi\rangle \\ \frac{\partial}{\partial t}(U|\psi_{\text{RF}}\rangle) &= -\frac{i}{\hbar}\mathcal{H}U|\psi_{\text{RF}}\rangle \\ \Rightarrow \frac{\partial}{\partial t}|\psi_{\text{RF}}\rangle &= -\frac{i}{\hbar}\underbrace{\left(U^\dagger\mathcal{H}U - i\hbar U^\dagger\frac{\partial}{\partial t}U\right)}_{\mathcal{H}_{\text{RF}}}|\psi_{\text{RF}}\rangle \end{aligned}$$

The second term of \mathcal{H}_{RF} follows readily

$$-i\hbar U^\dagger\frac{\partial}{\partial t}U = -i\hbar U^\dagger(-i\nu|2\rangle\langle 2|)U = -\nu|2\rangle\langle 2|.$$

*In the *slowly-varying envelope approximation*, we take the length scale and time scale over which the envelope function $\mathcal{E}(r, t)$ changes to be much smaller than the wavelength ($2\pi/|\mathbf{k}|$) and the period ($1/\nu$), respectively.

For the first term, we begin by expanding U in a power series,

$$U = \sum_{m=0}^{\infty} \frac{(-i\nu t)^m}{m!} (|2\rangle\langle 2|)^m.$$

From the orthonormality of the state $|2\rangle$,

$$(|2\rangle\langle 2|)^m = \begin{cases} |2\rangle\langle 2|, & m \geq 1 \\ 1, & m = 0 \end{cases}.$$

Hence,

$$\begin{aligned} U &= 1 + |2\rangle\langle 2| \sum_{m=1}^{\infty} \frac{(-i\nu t)^m}{m!} \\ U &= 1 - |2\rangle\langle 2| + |2\rangle\langle 2| + |2\rangle\langle 2| \sum_{m=1}^{\infty} \frac{(-i\nu t)^m}{m!} \\ U &= 1 - |2\rangle\langle 2| + |2\rangle\langle 2| \left(1 + \sum_{m=1}^{\infty} \frac{(-i\nu t)^m}{m!} \right) \\ U &= 1 - |2\rangle\langle 2| + |2\rangle\langle 2| e^{-i\nu t} \end{aligned}$$

The unitary transformation U then has the following action on the basis states,

$$U^\dagger |1\rangle = |1\rangle, \quad U^\dagger |2\rangle = e^{i\nu t} |2\rangle.$$

This allows us to compute the second term of \mathcal{H}_{RF} ,

$$U^\dagger \mathcal{H} U = \omega_{12}|2\rangle\langle 2| - (\mathcal{E}(r, t)e^{-i\nu t} + \mathcal{E}^*(r, t)e^{i\nu t}) (\mu_{12}|1\rangle\langle 2|e^{-i\nu t} + \mu_{21}|2\rangle\langle 1|e^{i\nu t}).$$

This part of \mathcal{H}_{RF} contains terms that oscillate as $e^{2i\nu t}$ or $e^{-2i\nu t}$, which can be eliminated because they are too fast to be relevant for our timescales of interest. With this approximation, the Hamiltonian in the rotating frame is then

$$\begin{aligned}\mathcal{H}_{\text{RF}} &= U^\dagger \mathcal{H} U - i\hbar U^\dagger \frac{\partial}{\partial t} U \\ \mathcal{H}_{\text{RF}} &= -\hbar(\nu - \omega_{12})|2\rangle\langle 2| - (\mathcal{E}(r, t)\mu_{21}|2\rangle\langle 1| + \mathcal{E}^*(r, t)\mu_{12}|1\rangle\langle 2|) \\ \mathcal{H}_{\text{RF}} &= -\hbar\delta|2\rangle\langle 2| - \hbar(\Omega|2\rangle\langle 1| + \Omega^*|1\rangle\langle 2|),\end{aligned}$$

where we have defined the Rabi frequency

$$\Omega = \frac{\mu_{21}\mathcal{E}(r, t)}{\hbar}.$$

If we define raising and lowering operators $\sigma \equiv |g\rangle\langle e|$, the dipole interaction can be written in the rotating frame as

$$\tilde{H}_{\text{AF}} = \frac{\hbar\Omega}{2} (\sigma + \sigma^\dagger), \quad \Omega \equiv -\frac{2\langle g|\hat{\varepsilon} \cdot \mathbf{d}|e\rangle}{\hbar} \mathbf{E}_0^{(+)} = -\frac{\langle g|\hat{\varepsilon} \cdot \mathbf{d}|e\rangle}{\hbar} E_0$$

where we have defined the Rabi frequency Ω . For a resonant interaction, the populations evolve as

$$c_g(t) = c_g(0) \cos\left(\frac{1}{2}\Omega t\right) - i\tilde{c}_e(0) \sin\left(\frac{1}{2}\Omega t\right)$$

$$\tilde{c}_e(t) = \tilde{c}_e(0) \cos\left(\frac{1}{2}\Omega t\right) - i c_g(0) \sin\left(\frac{1}{2}\Omega t\right)$$

DEFINE C1 AND C2 AND C2 TILDE.

For nearly-resonant interactions, we define a generalized Rabi frequency $\tilde{\Omega}$,

$$\tilde{\Omega} \equiv \sqrt{\Omega^2 + \Delta^2}, \quad \Delta \equiv \omega - \omega_0$$

In this case, the excited state population follows

$$p_e(t) = \frac{\Omega^2}{\tilde{\Omega}^2} \sin^2\left(\frac{1}{2}\tilde{\Omega}t\right)$$

The dressed states of the system have the following energies and form

$$E_{\pm} = -\frac{\hbar\Delta}{2} \pm \frac{\hbar\tilde{\Omega}}{2} \quad |+\rangle = \sin\theta|g\rangle + \cos\theta|e\rangle$$

$$\tan(2\theta) = -\frac{\Omega}{\Delta} \quad |-\rangle = \cos\theta|g\rangle - \sin\theta|e\rangle$$

In the far-detuned limit, $|-\rangle \approx |g\rangle$ with an AC Stark Shift,

$$E_- \Big|_{\Omega \ll \Delta} = -\frac{\hbar\Omega^2}{4\Delta}$$

SATURATION INTENSITY

The saturation intensity is defined[†]

$$I_{\text{sat}} \equiv \frac{2\Omega^2}{\Gamma^2} = \frac{c\epsilon_0\Gamma^2\hbar^2}{4|\langle g| \hat{\varepsilon} \cdot \mathbf{d} |e\rangle|^2}$$

There is a different saturation intensity for every transition between an initial state $|F, m_F\rangle$ and final state $|F', m'_F\rangle$ for a given polarization of light owing to the $|\langle g| \hat{\varepsilon} \cdot \mathbf{d} |e\rangle|$ appearing in the above expression. These can be computed as follows:

$$\begin{aligned} \langle F, m_F | e\mathbf{r}_q | F', m'_F \rangle &= \underbrace{\langle F | e\mathbf{r} | F' \rangle}_{A} \underbrace{\langle F, m_F | F', 1, m'_F, q \rangle}_{B} \\ A: \langle F | e\mathbf{r} | F' \rangle &= \langle J | e\mathbf{r} | J' \rangle (-1)^{F'+J+1+I} \sqrt{(2F'+1)(2J+1)} \begin{Bmatrix} J & J' & 1 \\ F' & F & I \end{Bmatrix} \\ B: \langle F, m_F | F', 1, m'_F, q \rangle &= (-1)^{F'-1+m_F} \sqrt{2F+1} \begin{pmatrix} F' & 1 & F \\ m'_F & q & -m_F \end{pmatrix} \end{aligned}$$

[†]The saturation parameter

$$s = \frac{I/I_{\text{sat}}}{1 + 4\Delta^2/\Gamma^2}$$

matches $R_{\text{opt}}/\gamma_{21} = 2|\Omega/\Gamma_{21}|^2$ with $\Gamma_{21} = \gamma_{21} - i\Delta$ in Misha's notes if you replace $\Omega \mapsto \Omega/2$ and $\gamma_{21} \mapsto \Gamma/2$. In Misha's notes, $\gamma_{21} = \gamma/2$, so probably $\Gamma_{\text{Steck}} = \gamma_{\text{Misha}}$.

Thus, atom-specific properties relevant to all the transitions of a specific D line can be reduced to a single reduced matrix element. The rest of the terms are calculable from F , F' , m_F , and m'_F .

$$D^2 \text{ line: } \left\langle J = \frac{1}{2} \middle\| e\mathbf{r} \middle\| J' = \frac{3}{2} \right\rangle$$

$$D^1 \text{ line: } \left\langle J = \frac{1}{2} \middle\| e\mathbf{r} \middle\| J' = \frac{1}{2} \right\rangle$$

Combining A and B into one expression,

$$\begin{aligned} \langle F, m_F | e\mathbf{r}_q | F', m'_F \rangle &= \langle J | e\mathbf{r} | J' \rangle (-1)^{F'+J+1+I} \sqrt{(2F'+1)(2J+1)} \begin{Bmatrix} J & J' & 1 \\ F' & F & I \end{Bmatrix} \\ &\times (-1)^{F'-1+m_F} \sqrt{2F+1} \begin{pmatrix} F' & 1 & F \\ m'_F & q & -m_F \end{pmatrix} \end{aligned}$$

STEADY-STATE POPULATION

The saturation intensity is the energy scale for the saturation of the excitation of a two-level atom.

The steady-state population is

$$\rho_{ee}(t \rightarrow \infty) = \frac{1}{2} \frac{I/I_{\text{sat}}}{1 + 4\Delta^2/\Gamma^2 + I/I_{\text{sat}}}$$

which for a resonant drive simplifies to

$$\rho_{ee}(t \rightarrow \infty) = \frac{1}{2} \frac{I/I_{\text{sat}}}{1 + I/I_{\text{sat}}}$$

For $I \gg I_{\text{sat}}$, the excited state population ρ_{ee} saturates to half. For $I \ll I_{\text{sat}}$, the atomic response is linear $\rho_{ee} \sim I/I_{\text{sat}}$.

1D CONSERVATIVE LATTICE

For the typical lattice used in lab, the nearest atomic transition is $\lambda_0 = 780 \text{ nm}$ and we detune the lasers to $\lambda_{\text{laser}} = 755 \text{ nm}$, which translates to $\Delta \approx 12 \text{ THz}$. The natural linewidth $\Gamma \approx 6 \text{ MHz}$. Hence,

$$\left(\frac{\Delta}{\Gamma}\right)^2 \approx 4 \times 10^{12}$$

Additionally, both the D₁ and D₂ transitions have saturation intensities $I_{\text{sat}} \approx 2 \text{ mW/cm}^2$. For a 200 mW beam with waist 100 μm , that gives an intensity of

$$I \approx \frac{200 \text{ mW}}{\pi (100 \mu\text{m})^2} \quad \Rightarrow \quad \frac{I}{I_{\text{sat}}} \approx 10^6$$

In this limit, we may then simplify the excited state population to

$$\rho_{ee} = \frac{1}{8} \frac{\Gamma^2}{\Delta^2} \frac{I}{I_{\text{sat}}}, \quad \frac{\Delta^2}{\Gamma^2} \gg \frac{I}{I_{\text{sat}}}, \Delta^2 \gg \Gamma^2$$

Our potentials are a result of a spatially varying Stark shift, so

$$V(z) = \Delta E_{\text{Stark}}(z) = \frac{\hbar\Gamma^2}{8\Delta} \frac{I(z)}{I_{\text{sat}}} \quad \Rightarrow \quad \frac{I(z)}{I_{\text{sat}}} = V(z) \left(\frac{8\Delta}{\hbar\Gamma^2} \right)$$

The probability of excitation then has a simple spatially varying form

$$\rho_{ee} = \frac{V(z)}{\hbar\Delta}$$

For reasonably large lattice depths, the atomic wavefunction can be approximated as a Gaussian with spread ℓ ,[‡]

$$\psi(z) = \frac{1}{\pi^{1/4}\sqrt{\ell}} e^{-\frac{z^2}{2\ell^2}}$$

If we integrate over the lattice potential, we get the overall probability of excitation,

$$\begin{aligned} \rho_{ee} &= \int_{-\infty}^{\infty} \rho_{ee}(z) |\psi(z)|^2 dz \\ \rho_{ee} &= \int_{-\infty}^{\infty} \frac{V(z)}{\hbar\Delta} |\psi(z)|^2 dz \\ \rho_{ee} &= \int_{-\infty}^{\infty} \frac{V_0}{2} \frac{1 \pm \cos(2kz)}{\hbar\Delta} \frac{1}{\sqrt{\pi\ell^2}} e^{-z^2/\ell^2} dz \\ \rho_{ee} &= \pm \frac{V_0}{2\hbar\Delta} \left(1 - e^{-k^2\ell^2} \right) \end{aligned}$$

In terms of the Lamb-Dicke parameter, $\eta = k\ell$, we can identify the following relations in the limit

[‡]The spread of the Gaussian is given by $\ell = \sqrt{\frac{\hbar}{m\omega}}$, where the trap frequency ω is $\hbar\omega = 2\sqrt{V_0 E_{\text{recoil}}}$ where V_0 is the depth of the optical lattice potential.

of $V_0 \gg E_{\text{recoil}}$,

$$\rho_{ee} = \begin{cases} \frac{V_0}{2\hbar\Delta} (1 - e^{-\eta^2}) \longrightarrow \frac{V_0}{2\hbar\Delta} \eta^2 & \Delta > 0 \\ \frac{V_0}{2\hbar\Delta} (e^{-\eta^2} - 1) \longrightarrow \frac{V_0}{2\hbar\Delta} (2 - \eta^2) & \Delta < 0 \end{cases}$$

AC STARK SHIFT

In terms of the saturation intensity, the AC Stark Shift can be written^s

$$\Delta E_{\text{Stark}} = \frac{\hbar\Gamma^2}{8\Delta} \frac{I}{I_{\text{sat}}}$$

For a Gaussian Beam^t, the intensity in the center is $2P/(\pi w^2)$ so that the Stark shift is

$$\Delta E_{\text{Stark}} = \frac{\hbar\Gamma^2}{8\Delta I_{\text{sat}}} \frac{2P}{\pi w^2}$$

Now converting $\Delta \equiv \omega_0 - \omega_L$ into wavelengths λ_0 and λ_L

$$\Delta E_{\text{Stark}} = \frac{\hbar\Gamma^2 P \lambda_0 \lambda_L}{\pi \cdot 8\pi w^2 I_{\text{sat}} c (\lambda_L - \lambda_0)}$$

^sThe decay Γ is defined in the optical Bloch equations:

$$\begin{aligned} \partial_t \rho_{ee} &= i \frac{\Omega}{2} (\tilde{\rho}_{eg} - \tilde{\rho}_{ge}) - \Gamma \rho_{ee} \\ \partial_t \tilde{\rho}_{ge} &= -(\gamma_\perp + i\Delta) \tilde{\rho}_{ge} - i \frac{\Omega}{2} (\rho_{ee} - \rho_{gg}) \end{aligned}$$

where the decay $\Gamma = 1/T_1$ is the longitudinal relaxation time and $\gamma_\perp = 1/T_2$ is the transverse relaxation time.

Lastly, we convert to Hertz using $h\nu_{\text{Stark}} = \Delta E_{\text{Stark}}$,

$$\nu_{\text{Stark}} = \frac{P\Gamma^2\lambda_0\lambda_L}{2\pi \cdot 8\pi^2 w^2 I_{\text{sat}} c (\lambda_L - \lambda_0)}$$

SCATTERING RATE

With the excited state population ρ_{ee} , the scattering rate R_{sc} is simply $\Gamma\rho_{ee}$,

$$R_{\text{sc}} = \frac{\Gamma}{2} \frac{I/I_{\text{sat}}}{1 + 4(\Delta/\Gamma)^2 + (I/I_{\text{sat}})}$$

A.1.1 BLOCH SPHERE

A.2 THREE-LEVEL ATOM

In this section, we consider a three-level Λ -type atom with driving fields that couple the two lower-lying states to the excited states. As was done in §A.1 for the two-level atom, we use the dipole approximation to treat the atom-field interaction and consider the slowly-varying envelope limit. In

[¶]The Gaussian beam takes the following normalized form,

$$E(r) = \sqrt{\frac{2P}{\pi w^2}} e^{-r^2/w^2}$$

where normalization is such that

$$P = \int_{-\infty}^{\infty} \int_{-\infty}^{\infty} E^2(r) dx dy = \int_0^{2\pi} \int_0^{\infty} E^2(r) r dr d\theta$$

this case, we can write the Hamiltonian

$$\begin{aligned}\mathcal{H} = & \hbar (\omega_{12}|2\rangle\langle 2| + \omega_{13}|3\rangle\langle 3|) \\ & - (\mathcal{E}_1(r, t)e^{-i\nu_1 t} + \mathcal{E}_1^*(r, t)e^{i\nu_1 t}) (\mu_{13}|1\rangle\langle 3| + \mu_{31}|3\rangle\langle 1|) \\ & - (\mathcal{E}_2(r, t)e^{-i\nu_2 t} + \mathcal{E}_2^*(r, t)e^{i\nu_2 t}) (\mu_{23}|2\rangle\langle 3| + \mu_{32}|3\rangle\langle 2|)\end{aligned}$$

We apply the unitary transformation defined by

$$U = e^{-i\nu_1 t|3\rangle\langle 3| - i(\nu_1 - \nu_2)t|2\rangle\langle 2|}$$

to transform into a rotating frame. As with the two-level atom, the Hamiltonian transforms according to

$$\mathcal{H}_{\text{RF}} = U^\dagger \mathcal{H} U - i\hbar U^\dagger \frac{\partial}{\partial t} U.$$

The second term of the effective Hamiltonian is

$$-i\hbar U^\dagger \frac{\partial}{\partial t} U = -\hbar\nu_1|3\rangle\langle 3| - \hbar(\nu_1 - \nu_2)|2\rangle\langle 2|.$$

Using the same power series technique as in §A.1, we can also obtain the identities,

$$U^\dagger |1\rangle = |1\rangle, \quad U^\dagger |2\rangle = |2\rangle e^{-i(\nu_1 - \nu_2)t}, \quad U^\dagger |3\rangle = |3\rangle e^{-i\nu_1 t},$$

which we use to compute the first term in the effective Hamiltonian. The Hamiltonian in this new frame is then,

$$\begin{aligned}\mathcal{H}_{\text{RF}} = & \hbar (\omega_{12}|2\rangle\langle 2| + \omega_{13}|3\rangle\langle 3|) - \hbar ((\nu_1 - \nu_2)|2\rangle\langle 2| + \nu_1|3\rangle\langle 3|) \\ & - (\mathcal{E}_1(r, t)e^{-i\nu_1 t} + \mathcal{E}_1^*(r, t)e^{i\nu_1 t}) (\mu_{13}|1\rangle\langle 3|e^{i\nu_1 t} + \mu_{31}|3\rangle\langle 1|e^{-i\nu_1 t}) \\ & - (\mathcal{E}_2(r, t)e^{-i\nu_2 t} + \mathcal{E}_2^*(r, t)e^{i\nu_2 t}) (\mu_{23}|2\rangle\langle 3|e^{i\nu_2 t} + \mu_{32}|3\rangle\langle 2|e^{-i\nu_2 t}),\end{aligned}$$

which after removing the fast oscillating terms simplifies to,

$$\begin{aligned}\Rightarrow \mathcal{H}_{\text{RF}} = & \hbar [(\omega_{12} - (\nu_1 - \nu_2)) |2\rangle\langle 2| + (\omega_{12} - \nu_1)|3\rangle\langle 3|] \\ & - (\mu_{13}\mathcal{E}_1(r, t)|1\rangle\langle 3| + \mu_{31}\mathcal{E}_1^*(r, t)|3\rangle\langle 1|) \\ & - (\mu_{23}\mathcal{E}_2(r, t)|2\rangle\langle 3| + \mu_{32}\mathcal{E}_2^*(r, t)|3\rangle\langle 2|).\end{aligned}$$

B

Orbital Excitation Blockade

B.1 STATE PREPARATION

Our experiments begin with a degenerate 2D Bose gas of ^{87}Rb atoms prepared in the $|F = 1, m_f = -1\rangle$ state in a single layer of a 1D optical lattice with spacing $1.5 \mu\text{m}$, in the focal plane of a high resolution imaging system as described in previous work. The atoms are then loaded into a 2D optical lattice with spacing 680 nm , which is ramped up to a depth of $45E_r$ adiabatically on either a single-

or many- body timescale, depending upon the experiment to be performed.

B.2 HIGHER BAND REMOVAL

The orbital blockade is observed through the deterministic removal of atoms in higher bands of the $1.5 \mu\text{m}$ lattice. For removal of atoms from the second band, this is achieved by reducing the depth of this lattice to 3.8 kHz from an initial depth of 35.8 kHz. Gravity produces a shift of 3.2 kHz per well, thus inducing second band atoms to Zener tunnel away within a few ms. The Landau-Zener tunneling rate from the ground state is given by $\Gamma_{LZ} = \frac{mga}{2\pi\hbar} e^{-g_c/g} \approx 12 \text{ Hz}$. Here g is the gravitational acceleration and $g_c = a\omega_z^2/4$. This effect leads to a loss of ground state atoms on the percent level, but can be made negligible by using excitations to the fourth band.

B.3 BAND DEPENDENT ENERGY SHIFTS

Due to its large spacing, the $1.5 \mu\text{m}$ lattice has a recoil energy of only 250 Hz. Consequently its depth is ~ 150 recoils, and its low-lying eigenstates are, to good approximation, the Hermite-Gaussians of a harmonic oscillator. The interaction energy between particles in bands m and n may thus be written in terms of the ground band interaction energy U_{00} as:

$$U_{nm} = U_{00}(2 - \delta_{nm}) \frac{\int |\psi_m(x)|^2 |\psi_n(x)|^2 dx}{\int |\psi_0(x)|^4 dx}$$

$\Delta\omega_z/2\pi$ [Hz]	$n = 1$	$n = 2$	$n = 3$	$n = 4$
$m = 0$	0	-217	-434	-651
$m = 1$	-9	-226	-443	
$m = 2$	-18	-235		
$m = 3$	-27			

Table B.1: Frequency shifts in Hz for a transition transferring an atom from the ground band to the fourth band, starting with n and m atoms in each of these bands. The shifts are measured relative to an initial state with one atom in the ground band and none in the excited band.

where $\psi_m(x)$ is the normalized m th harmonic oscillator wavefunction. The total interaction shift

for M particles in band m , and N particles in band n is thus:

$$\frac{M(M-1)}{2}U_{mm} + \frac{N(N-1)}{2}U_{nn} + MNU_{mn}.$$

The interactions also produce off-resonant band changing collisions, with a Rabi frequency:

$$\Omega_{mn \leftrightarrow pq} = U_{00}C_{mn \leftrightarrow pq} \frac{\int \psi_m(x)\psi_n(x)\psi_p^*(x)\psi_q^*(x) dx}{\int |\psi_0(x)|^4 dx}$$

up to a combinatoric factor $C_{mn \leftrightarrow pq}$ resulting from Bose enhancement. For an energy defect of $\delta_{mn \leftrightarrow pq} \gg \Omega_{mn \leftrightarrow pq}$, this process produces an energy shift of $\Delta_{mn} = -|\Omega_{mn \leftrightarrow pq}|^2/\delta_{mn \leftrightarrow pq}$. For our experiment, the dominant band changing collision is $|m = 0, n = 2\rangle \rightarrow |p = 1, q = 1\rangle$ with a Rabi frequency $\Omega_{02 \leftrightarrow 11} = 2\pi \times 120$ Hz. In this case lattice anharmonicity and interaction shifts produce an energy defect of $\delta_{02 \leftrightarrow 11} = 2\pi \times 330$ Hz, resulting in an additional overall shift of the $|0, 2\rangle$ state of $\Delta_{02} = -2\pi \times 45$ Hz.

B.4 LIMITS ON ENTROPIES ACHIEVABLE WITH ALGORITHMIC COOLING

In our system, the main limitation on the achievable entropies with algorithmic cooling is losses during the Landau-Zener chirp. Spontaneous emission after absorption of photons from the lattice leads to excitation of atoms from the ground state at a rate of 0.1 s^{-1} . These atoms are quickly lost due to tunneling in the higher bands in the case of the in-plane lattice or in the band filtering step in the case of the axial lattice. This leads to holes in an $n = 1$ Mott insulator (3% during the 250 ms ramp), setting a lower bound on the reachable entropy after thermalization of $\approx 0.15k_B$ per particle. The lattice light is detuned 25 nm to the blue of the atomic resonance, and the heating rate can be made negligible by increasing the detuning (e.g. using 1064 nm lattice light). A more fundamental limit on the single-shot cooling algorithm demonstrated here is given by initial holes in the Mott insulator that cannot be corrected. For our Mott insulators, the hole fraction is on the order of 0.5% corresponding to a post-thermalization entropy of $\approx 0.06k_B$ per particle. This limit can be overcome by the iterative algorithm described in the text. For Mott insulators with large initial atom numbers per site, it is also important to take into account the efficiency of the Landau-Zener chirp. For excitation to the second band, the measured efficiency is 0.94(1).

C

Harper-Hofstadter ladder

C.1 EXPERIMENTAL SEQUENCE

All of the experiments described in this letter start with a 2-D, single layer Mott insulator of ^{87}Rb in a deep optical lattice ($V_x = V_y = 45E_r$, $E_r/2\pi \sim 1.24 \text{ kHz}$) with a 680 nm spacing¹². The experimental sequences for both the single-particle and interacting two-particle experiments are illustrated in Fig. C.1.

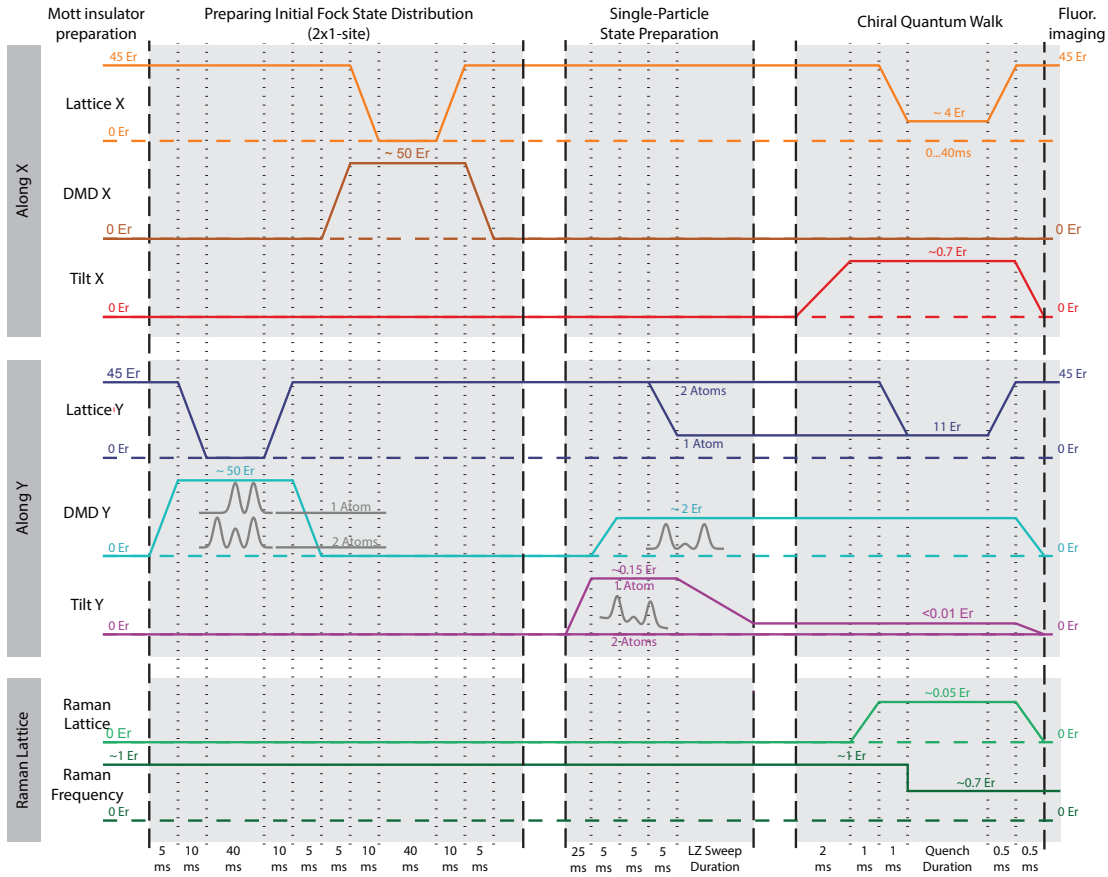


Figure C.1: Experimental sequence: Schematic showing the approximate ramps and relative timing of the x -, y -lattices, the x -, y -DMD-potentials, the x -, y -tilts, and the Raman lattice. The profiles of the DMD potentials are sketched for the dimension labeled on the left. The other dimension of the profiles is well described by a smooth flattop potential within the region used for the experiment. All optical ramps are changed exponentially in depth as a function of time and are sketched with a logarithmic y-scale here. The x -, y -tilts that are created by magnetic field gradients are, however, plotted and ramped linearly.

C.1.1 INITIAL STATE PREPARATION

PREPARATION OF THE INITIAL FOCK STATE DISTRIBUTION

For both experiments we deterministically prepare an initial state from the $N = 1$ shell of a Mott insulator. We choose the number of atoms for each experiment by projecting an additional confining (or “cutting”) optical potential from a digital micromirror device (DMD) located in the Fourier plane of our imaging system⁹⁹. This “cutting” potential is either a single-well or a double-well along one dimension, and a smoothed flattop potential along the other dimension. The additional potential is superimposed on top of the atoms which are still situated in a deep lattice. The atoms outside of the “cutting” potential are then removed from the system by turning off the optical lattice and applying an anti-confining potential to efficiently expel them from the system. The lattice is then ramped back on and the anti-confinement potential is turned off. As illustrated in Fig. C.2, this sequence is first applied in the x - and then in the y -direction of the lattice such that either a 1×1 or a 2×1 initial state is produced. The loading efficiency of these states is $\approx 93\%$ and is largely dominated by the initial Mott insulator fidelity.

SINGLE-PARTICLE STATE PREPARATION

There is an additional Landau-Zener preparation step for the single-particle experiments, which require an individual atom to be delocalized across the central rung of the ladder system. First, the ladder-forming double-well potential is projected on top of a deep, non-tilted lattice with a single atom being located on one side of the central double-well. While the tunneling is still suppressed,

we add an additional tilt $\Delta \gg J$ with a physical magnetic field gradient along the rung direction, which is used to prepare the occupied site as the ground state of the tilted double-well system (cf. Fig. C.2 (c)). Tunneling is then rapidly increased by ramping down the lattice potential (final parameters: $V_y = 11E_r, \frac{\Delta}{J} \approx 20$). Finally, we adiabatically prepare the $\Delta = 0$ ground state of the balanced double-well system by ramping down the magnetic field gradient over a period of 100ms, which results in the state $|\psi_{\text{initial}}\rangle = \frac{1}{\sqrt{2}}(a_U^\dagger + a_D^\dagger)|\text{vac}\rangle$. In doing so, we bring the gradient close to zero but eventually set it to a small finite value for the remainder of the experiment. This empirically chosen value compensates for any other sources of tilt in the double-well system and maintains the balanced population in the $|U\rangle$ and $|D\rangle$ states until the experiment is started.

C.1.2 QUENCH DYNAMICS WITH A GAUGE FIELD

After the preparation of the initial state (either one or two particles), the dynamics are initiated by a quench in both directions. In the two-particle case, a double-well potential whose minima align with those of the y -lattice is superimposed on the lattice to create a $2 \times N$ confining potential. Afterwards, complex tunneling along the x -direction is engineered by ramping on a physical magnetic field gradient while still maintaining a deep optical lattice. This gradient is large enough to suppress tunneling even after the next step, during which the optical lattice is ramped down to a lower depth. It is noteworthy that the resonance frequency for restoring the tunneling is calibrated at this lower lattice depth, since optical potentials of different strengths can have residual gradients resulting in a lattice-depth dependent resonance condition. To restore the tunneling suppressed by the tilt, the Raman lattice power is first ramped up to $V_R \approx 0.05E_r$, then the optical lattice along the x -

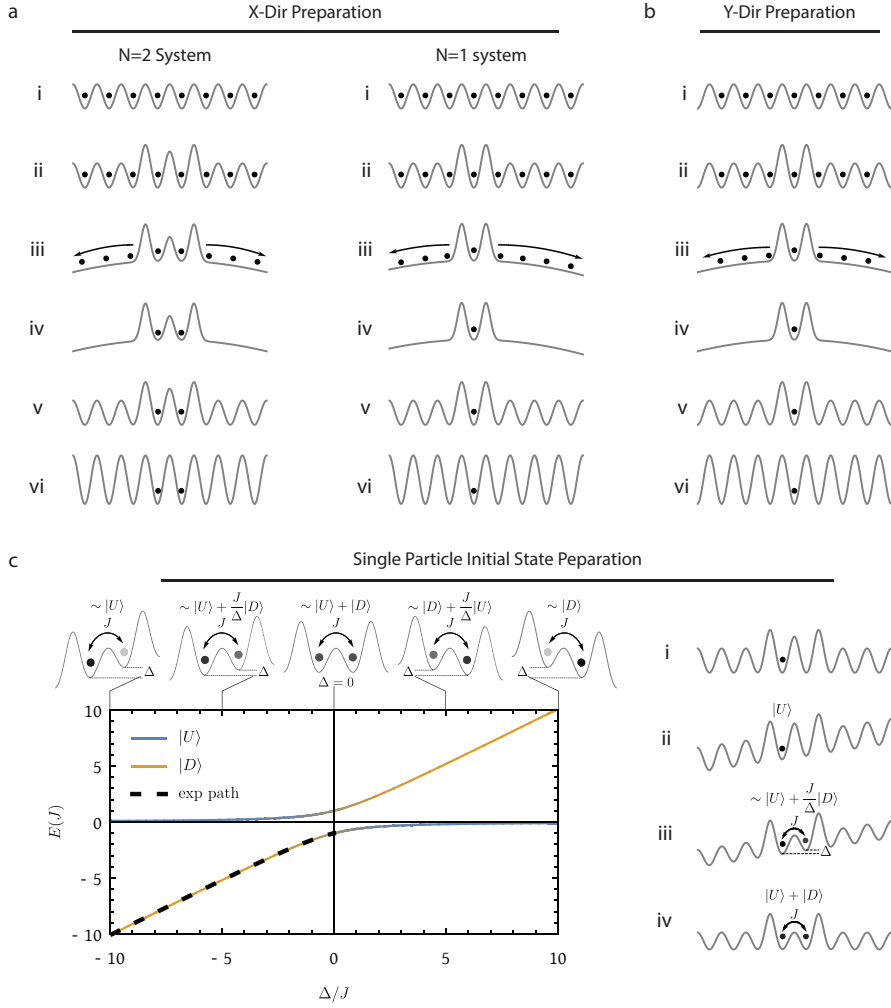


Figure C.2: Initial state preparation: The steps for preparing the one- or two-particle states are shown in part **a** and **b** for the x - and y -directions, respectively. **i,ii** illustrate the superposition of the confining DMD potential and the bare lattice potential. **iii,iv** illustrate the removal of unwanted atoms from the system due to the removal of the optical lattice and the addition of an anti-confining potential. **v,vi** illustrate the reloading of the optical lattice and the removal of the additional “cutting” potential from the DMD. The preparation of the delocalized single-particle initial state is illustrated in panel **c**. The left plot shows the energy of the two instantaneous eigenstates of the system as a function of $\frac{\Delta}{J}$ where the color denotes the overlap of the bare states $|U\rangle$ and $|D\rangle$ with these eigenstates. The initial state for the single-particle experiments is obtained by starting at $\frac{\Delta}{J} \approx 20$ and adiabatically following the ground state to the $\Delta = 0$ point in the diagram, as denoted by the dashed black line in panel **b**. The sketches above the plot visualize the approximate description of the system at given ratios of Δ/J . The overall preparation sequence is visualized in the additional sketches **i-iv**. **i,ii** show the tilting of the lattice while tunneling is still strongly suppressed. **iii** shows the restoration of tunneling after the depth of the tilted lattice has been reduced. **iv** shows the final state produced by the Landau-Zener sweep after the tilt has been ramped down. The overall sequence thus corresponds to the state transformation $|U\rangle \rightarrow \frac{1}{\sqrt{2}}(|U\rangle + |D\rangle)$.

direction is ramped down to $\approx 4E_r$ to increase the bare tunneling in this direction. Afterwards, the frequency of the Raman lattice is chirped to the resonant frequency to enable complex tunneling and thereby realize the Harper-Hofstadter Hamiltonian on the $2 \times N$ ladder that is defined by the bare lattice and the remaining DMD potential. In the two-particle case, the y -lattice is additionally quenched to $11E_r$ at the time the Raman lattice is chirped to resonance. In the single-particle case, this is unnecessary since the lattice is left at $11E_r$ from the Landau-Zener sweep. After a given quench time all lattices are ramped to their maximum depth to suppress all dynamics and the atoms are then imaged with single-site resolution (C.1). For all two particle experiments conducted, the doublon fraction at any time during the evolution is sufficiently small such that the results are not affected by the loss of atoms due to parity projection.

References

- [1] (1991). *LT1011/LT1011A Voltage Comparator*. Linear Technology Corporation.
- [2] (2008). *AD9522-0*. Analog Devices.
- [3] Abo-Shaeer, J. R., Raman, C., Vogels, J. M., & Ketterle, W. (2001). Observation of vortex lattices in bose-einstein condensates. *Science*, 292(5516), 476–479.
- [4] Aidelsburger, M. (2015). *Artificial gauge fields with ultracold atoms in optical lattices*. PhD thesis, Ludwig-Maximilians-Universität.
- [5] Aidelsburger, M., Atala, M., Lohse, M., Barreiro, J. T., Paredes, B., & Bloch, I. (2013). Realization of the Hofstadter Hamiltonian with Ultracold Atoms in Optical Lattices. *Phys. Rev. Lett.*, 111(18), 185301.
- [6] Aidelsburger, M., Atala, M., Nascimbène, S., Trotzky, S., Chen, Y.-A., & Bloch, I. (2011). Experimental Realization of Strong Effective Magnetic Fields in an Optical Lattice. *Phys. Rev. Lett.*, 107(25), 255301.
- [7] Aidelsburger, M., Lohse, M., Schweizer, C., Atala, M., Barreiro, J. T., Nascimbène, S., Cooper, N. R., Bloch, I., & Goldman, N. (2015). Measuring the Chern number of Hofstadter bands with ultracold bosonic atoms. *Nat. Phys.*, 11(2), 162–166.
- [8] An, F. A., Meier, E. J., & Gadway, B. (2016). Direct observation of chiral currents and magnetic reflection in atomic flux lattices. *arXiv:1609.09467 [cond-mat, physics:physics, physics:quant-ph]*. arXiv: 1609.09467.
- [9] Anderson, M. H., Ensher, J. R., Matthews, M. R., Wieman, C. E., & Cornell, E. A. (1995). Observation of Bose-Einstein Condensation in a Dilute Atomic Vapor. *Science*, 269(5221), 198–201.
- [10] Bakr, W. (2011). *Microscopic Studies of Quantum Phase Transitions in Optical Lattices*. PhD thesis, Harvard University.

- [11] Bakr, W. S., Gillen, J. I., Peng, A., Fölling, S., & Greiner, M. (2009a). A quantum gas microscope for detecting single atoms in a hubbard-regime optical lattice. *Nature*, 462(7269), 74–77.
- [12] Bakr, W. S., Gillen, J. I., Peng, A., Fölling, S., & Greiner, M. (2009b). A quantum gas microscope for detecting single atoms in a hubbard-regime optical lattice. *Nature*, 462, 74.
- [13] Bakr, W. S., Peng, A., Tai, M. E., Ma, R., Simon, J., Gillen, J. I., Fölling, S., Pollet, L., & Greiner, M. (2010). Probing the superfluid--to--Mott insulator transition at the single-atom level. *Science*, 329(5991), 547 –550.
- [14] Bakr, W. S., Preiss, P. M., Tai, M. E., Ma, R., Simon, J., & Greiner, M. (2011). Orbital excitation blockade and algorithmic cooling in quantum gases. *Nature*, 480(7378), 500–503.
- [15] Bardeen, J., Cooper, L. N., & Schrieffer, J. R. (1957a). Microscopic Theory of Superconductivity. *Physical Review*, 106(1), 162–164.
- [16] Bardeen, J., Cooper, L. N., & Schrieffer, J. R. (1957b). Theory of Superconductivity. *Physical Review*, 108(5), 1175–1204.
- [17] Baugh, J., Moussa, O., Pyan, C., Nayak, A., & Laflamme, R. (2005). Experimental implementation of heat-bath algorithmic cooling using solid-state nuclear magnetic resonance. *Nature*, 438, 470–473.
- [18] Baumann, K., Guerlin, C., Brennecke, F., & Esslinger, T. (2010). Dicke quantum phase transition with a superfluid gas in an optical cavity. *Nature*, 464(7293), 1301–1306.
- [19] Blatt, R. & Roos, C. F. (2012). Quantum simulations with trapped ions. *Nature Physics*, 8(4), 277–284.
- [20] Bloch, I., Dalibard, J., & Zwerger, W. (2008). Many-body physics with ultracold gases. *Rev. Mod. Phys.*, 80(3), 885–964.
- [21] Boykin, P., Mor, T., Roychowdhury, V., Vatan, F., & Vrijen, R. (2002). Algorithmic cooling and scalable NMR quantum computers. *Proc. Natl. Acad. Sci.*, 99, 3388–3393.
- [22] Campbell, G. K., Mun, J., Boyd, M., Medley, P., Leanhardt, A. E., Marcassa, L. G., Pritchard, D. E., & Ketterle, W. (2006). Imaging the Mott insulator shells by using atomic clock shifts. *Science*, 313(5787), 649 –652.

- [23] Celi, A., Massignan, P., Ruseckas, J., Goldman, N., Spielman, I. B., Juzeliūnas, G., & Lewenstein, M. (2014). Synthetic gauge fields in synthetic dimensions. *Phys. Rev. Lett.*, 112, 043001.
- [24] Cheinet, P., Trotzky, S., Feld, M., Schnorrberger, U., Moreno-Cardoner, M., Fölling, S., & Bloch, I. (2008). Counting atoms using interaction blockade in an optical superlattice. *Phys. Rev. Lett.*, 101(9), 090404.
- [25] Chen, X., Gu, Z.-C., & Wen, X.-G. (2010). Local unitary transformation, long-range quantum entanglement, wave function renormalization, and topological order. *Phys. Rev. B*, 82, 155138.
- [26] Coddington, I., Engels, P., Schweikhard, V., & Cornell, E. A. (2003). Observation of Tkachenko Oscillations in Rapidly Rotating Bose-Einstein Condensates. *Phys. Rev. Lett.*, 91(10), 100402.
- [27] Dalibard, J. & Cohen-Tannoudji, C. (1989). Laser cooling below the Doppler limit by polarization gradients: simple theoretical models. *JOSA B*, 6(11), 2023–2045.
- [28] Davis, K. B., Mewes, M. O., Andrews, M. R., van Druten, N. J., Durfee, D. S., Kurn, D. M., & Ketterle, W. (1995). Bose-Einstein Condensation in a Gas of Sodium Atoms. *Physical Review Letters*, 75(22), 3969–3973.
- [29] Dhar, A., Maji, M., Mishra, T., Pai, R. V., Mukerjee, S., & Paramekanti, A. (2012). Bose-hubbard model in a strong effective magnetic field: Emergence of a chiral mott insulator ground state. *Phys. Rev. A*, 85, 041602.
- [30] Endres, M., Fukuhara, T., Pekker, D., Cheneau, M., Schauß, P., Gross, C., Demler, E., Kuhr, S., & Bloch, I. (2012). The ‘higgs’ amplitude mode at the two-dimensional superfluid/Mott insulator transition. *Nature*, 487(7408), 454–458.
- [31] Feynman, R. (1981). Simulating Physics with Computers. *International Journal of Theoretical Physics*, 21, 467.
- [32] Fukuhara, T., Kantian, A., Endres, M., Cheneau, M., Schauß, P., Hild, S., Bellem, D., Schollwöck, U., Giamarchi, T., Gross, C., Bloch, I., & Kuhr, S. (2013). Quantum dynamics of a mobile spin impurity. *Nature Physics*, 9(4), 235–241.
- [33] Gaëtan, A., Miroshnychenko, Y., Wilk, T., Chotia, A., Viteau, M., Comparat, D., Pillet, P., Browaeys, A., & Grangier, P. (2009). Observation of collective excitation of two individual atoms in the Rydberg blockade regime. *Nat. Phys.*, 5(2), 115–118.

- [34] Gemelke, N., Sarajlic, E., & Chu, S. (2010). Rotating Few-body Atomic Systems in the Fractional Quantum Hall Regime. *preprint at <http://arXiv.org/abs/1007.2677>*.
- [35] Greif, D. (2013). *Quantum magnetism with ultracold fermions in an optical lattice*. PhD thesis, ETH Zurich.
- [36] Greiner, M. (2000). *Magnetischer Transfer von Atomen ein Weg zur einfachen Bose-Einstein-Kondensation*. PhD thesis, Ludwig-Maximilians-Universität.
- [37] Greiner, M. (2003). *Ultracold quantum gases in three-dimensional optical lattice potentials*. PhD thesis, Ludwig-Maximilians-Universität.
- [38] Greiner, M., Mandel, O., Esslinger, T., Hänsch, T. W., & Bloch, I. (2002). Quantum phase transition from a superfluid to a Mott insulator in a gas of ultracold atoms. *Nature*, 415(6867), 39–44.
- [39] Hafezi, M., Mittal, S., Fan, J., Migdall, A., & Taylor, J. M. (2013). Imaging topological edge states in silicon photonics. *Nat. Photonics.*, 7(12), 1001–1005.
- [40] Hafezi, M., Sørensen, A. S., Demler, E., & Lukin, M. D. (2007). Fractional quantum hall effect in optical lattices. *Phys. Rev. A*, 76, 023613.
- [41] Harper, P. G. (1955). Single band motion of conduction electrons in a uniform magnetic field. *Proceedings of the Physical Society. Section A*, 68(10), 874.
- [42] Hartmann, T., Keck, F., Korsch, H. J., & Mossmann, S. (2004). Dynamics of Bloch oscillations. *New J. Phys.*, 6.
- [43] Hasan, M. Z. & Kane, C. L. (2010). *Colloquium : Topological insulators*. *Rev. Mod. Phys.*, 82, 3045–3067.
- [44] Hofstadter, D. R. (1976). Energy levels and wave functions of bloch electrons in rational and irrational magnetic fields. *Phys. Rev. B*, 14, 2239–2249.
- [45] Houck, A. A., Tureci, H. E., & Koch, J. (2012). On-chip quantum simulation with superconducting circuits. *Nature Physics*, 8(4), 292–299.
- [46] Huber, F. (2014). *Site-Resolved Imaging with the Fermi Gas Microscope*. PhD thesis, Harvard University.

- [47] Hügel, D. & Paredes, B. (2014). Chiral ladders and the edges of quantum hall insulators. *Phys. Rev. A*, 89, 023619.
- [48] Islam, R., Ma, R., Preiss, P. M., Tai, M. E., Lukin, A., Rispoli, M., & Greiner, M. (2015). Measuring entanglement entropy in a quantum many-body system. *Nature*, 528(7580), 77–83.
- [49] Jaksch, D., Bruder, C., Cirac, J. I., Gardiner, C. W., & Zoller, P. (1998). Cold Bosonic Atoms in Optical Lattices. *Physical Review Letters*, 81(15), 3108–3111.
- [50] Jaksch, D. & Zoller, P. (2003). Creation of effective magnetic fields in optical lattices: the hofstadter butterfly for cold neutral atoms. *New Journal of Physics*, 5(1), 56.
- [51] Jotzu, G., Messer, M., Desbuquois, R., Lebrat, M., Uehlinger, T., Greif, D., & Esslinger, T. (2014). Experimental realization of the topological haldane model with ultracold fermions. *Nature*, 515(7526), 237–240. Letter.
- [52] Kaufman, A. M., Tai, M. E., Lukin, A., Rispoli, M., Schittko, R., Preiss, P. M., & Greiner, M. (2016). Quantum thermalization through entanglement in an isolated many-body system. *Science*, 353(6301), 794–800.
- [53] Kolkowitz, S., Bromley, S. L., Bothwell, T., Wall, M. L., Marti, G. E., Koller, A. P., Zhang, X., Rey, A. M., & Ye, J. (2016). Spin-orbit coupled fermions in an optical lattice clock. *arXiv:1608.03854 [cond-mat, physics:physics, physics:quant-ph]*. arXiv: 1608.03854.
- [54] Kolovsky, A. R. (2011). Creating artificial magnetic fields for cold atoms by photon-assisted tunneling. *Europhys. Lett.*, 93(2), 20003.
- [55] Laughlin, R. B. (1983). Anomalous quantum hall effect: An incompressible quantum fluid with fractionally charged excitations. *Phys. Rev. Lett.*, 50, 1395–1398.
- [56] Léonard, J., Morales, A., Zupancic, P., Esslinger, T., & Donner, T. (2017). Supersolid formation in a quantum gas breaking a continuous translational symmetry. *Nature*, 543(7643), 87–90.
- [57] Lewenstein, M., Sanpera, A., & Ahufinger, V. (2012). *Ultracold Atoms in Optical Lattices*. Oxford University Press, 1 edition.

- [58] Lewenstein, M., Sanpera, A., Ahufinger, V., Damski, B., Sen, A., & Sen, U. (2007). Ultracold atomic gases in optical lattices: mimicking condensed matter physics and beyond. *Adv. Phys.*, 56(2), 243–379.
- [59] Lignier, H., Sias, C., Ciampini, D., Singh, Y., Zenesini, A., Morsch, O., & Arimondo, E. (2007). Dynamical control of matter-wave tunneling in periodic potentials. *Phys. Rev. Lett.*, 99, 220403.
- [60] Lin, Y.-J., Compton, R. L., Jiménez-García, K., Porto, J. V., & Spielman, I. B. (2009). Synthetic magnetic fields for ultracold neutral atoms. *Nature*, 462(7273), 628–632.
- [61] Ma, R. (2014). *Engineered potentials and dynamics of ultracold quantum gases under the microscope*. PhD thesis, Harvard University.
- [62] Madison, K. W., Chevy, F., Wohlleben, W., & Dalibard, J. (2000). Vortex formation in a stirred bose-einstein condensate. *Phys. Rev. Lett.*, 84, 806–809.
- [63] Madison, K. W., Fischer, M. C., Diener, R. B., Niu, Q., & Raizen, M. G. (1998). Dynamical bloch band suppression in an optical lattice. *Phys. Rev. Lett.*, 81, 5093–5096.
- [64] Mancini, M., Pagano, G., Cappellini, G., Livi, L., Rider, M., Catani, J., Sias, C., Zoller, P., Inguscio, M., Dalmonte, M., & Fallani, L. (2015). Observation of chiral edge states with neutral fermions in synthetic Hall ribbons. *Science*, 349(6255), 1510–1513.
- [65] Mazurenko, A., Chiu, C. S., Ji, G., Parsons, M. F., Kanôsz-Nagy, M., Schmidt, R., Grusdt, F., Demler, E., Greif, D., & Greiner, M. (2016). Experimental realization of a long-range antiferromagnet in the Hubbard model with ultracold atoms. *arXiv:1612.08436 [cond-mat]*. arXiv: 1612.08436.
- [66] McKay, D. C. & DeMarco, B. (2011). Cooling in strongly correlated optical lattices: prospects and challenges. *Rep. Prog. Phys.*, 74(5), 054401.
- [67] Medley, P., Weld, D. M., Miyake, H., Pritchard, D. E., & Ketterle, W. (2011). Spin gradient demagnetization cooling of ultracold atoms. *Phys. Rev. Lett.*, 106(19), 195301.
- [68] Miyake, H., Siviloglou, G. A., Kennedy, C. J., Burton, W. C., & Ketterle, W. (2013). Realizing the Harper Hamiltonian with Laser-Assisted Tunneling in Optical Lattices. *Phys. Rev. Lett.*, 111(18), 185302.

- [69] Monroe, C., Swann, W., Robinson, H., & Wieman, C. (1990). Very cold trapped atoms in a vapor cell. *Physical Review Letters*, 65(13), 1571–1574.
- [70] Müller, T., Fölling, S., Widera, A., & Bloch, I. (2007). State preparation and dynamics of ultracold atoms in higher lattice orbitals. *Phys. Rev. Lett.*, 99(20), 200405.
- [71] Nayak, C., Simon, S. H., Stern, A., Freedman, M., & Das Sarma, S. (2008). Non-abelian anyons and topological quantum computation. *Rev. Mod. Phys.*, 80, 1083–1159.
- [72] Nelson, K. D., Li, X., & Weiss, D. (2007). Imaging single atoms in a three-dimensional array. *Nature Phys.*, (pp. 556–560).
- [73] Nikolopoulos, G. M. & Petrosyan, D. (2010). Atom-number filter in an optical lattice. *J. Phys. B*, 43(13), 131001.
- [74] Paredes, B., Fedichev, P., Cirac, J. I., & Zoller, P. (2001). $\frac{1}{2}$ -Anyons in Small Atomic Bose-Einstein Condensates. *Physical Review Letters*, 87(1), 010402.
- [75] Parsons, M. F., Huber, F., Mazurenko, A., Chiu, C. S., Setiawan, W., Wooley-Brown, K., Blatt, S., & Greiner, M. (2015). Site-Resolved Imaging of Fermionic ${}^6\text{Li}$ in an Optical Lattice. *Physical Review Letters*, 114(21), 213002.
- [76] Parsons, M. F., Mazurenko, A., Chiu, C. S., Ji, G., Greif, D., & Greiner, M. (2016). Site-resolved measurement of the spin-correlation function in the Fermi-Hubbard model. *Science*, 353(6305), 1253–1256.
- [77] Popp, M., Garcia-Ripoll, J.-J., Vollbrecht, K. G., & Cirac, J. I. (2006). Ground-state cooling of atoms in optical lattices. *Phys. Rev. A*, 74(1), 013622.
- [78] Preiss, P. (2015). *Atomic Bose-Hubbard Systems with Single-Particle Control*. PhD thesis, Harvard University.
- [79] Preiss, P. M., Ma, R., Tai, M. E., Lukin, A., Rispoli, M., Zupancic, P., Lahini, Y., Islam, R., & Greiner, M. (2015a). Strongly correlated quantum walks in optical lattices. *Science*, 347(6227), 1229–1233.
- [80] Preiss, P. M., Ma, R., Tai, M. E., Simon, J., & Greiner, M. (2015b). Quantum gas microscopy with spin, atom-number, and multilayer readout. *Physical Review A*, 91(4), 041602.

- [81] Raab, E. L., Prentiss, M., Cable, A., Chu, S., & Pritchard, D. E. (1987). Trapping of Neutral Sodium Atoms with Radiation Pressure. *Physical Review Letters*, 59(23), 2631–2634.
- [82] Rabl, P., Daley, A. J., Fedichev, P. O., Cirac, J. I., & Zoller, P. (2003). Defect-suppressed atomic crystals in an optical lattice. *Phys. Rev. Lett.*, 91(11), 110403.
- [83] Roushan, P., Neill, C., Megrant, A., Chen, Y., Babbush, R., Barends, R., Campbell, B., Chen, Z., Chiaro, B., Dunsworth, A., Fowler, A., Jeffrey, E., Kelly, J., Lucero, E., Mutus, J., O’Malley, P. J. J., Neeley, M., Quintana, C., Sank, D., Vainsencher, A., Wenner, J., White, T., Kapit, E., Neven, H., & Martinis, J. (2016). Chiral ground-state currents of interacting photons in a synthetic magnetic field. *Nat. Phys.*, advance online publication, –.
- [84] Schneider, P. & Saenz, A. (2011). Quantum computation with ultracold atoms in a driven optical lattice. *arXiv:1103.4950*.
- [85] Schweikhard, V., Coddington, I., Engels, P., Mogendorff, V. P., & Cornell, E. A. (2004). Rapidly Rotating Bose-Einstein Condensates in and near the Lowest Landau Level. *Phys. Rev. Lett.*, 92(4), 040404.
- [86] Setiawan, W. (2013). *Fermi Gas Microscope*. PhD thesis, Harvard University.
- [87] Sherson, J. F. & Mølmer, K. (2010). Shaking the entropy out of a lattice: atomic filtering by vibrational excitations. *arXiv:1012.1457*.
- [88] Sherson, J. F., Weitenberg, C., Endres, M., Cheneau, M., Bloch, I., & Kuhr, S. (2010). Single-atom-resolved fluorescence imaging of an atomic Mott insulator. *Nature*, 467(7311), 68–72.
- [89] Simon, J., Bakr, W. S., Ma, R., Tai, M. E., Preiss, P. M., & Greiner, M. (2011). Quantum simulation of antiferromagnetic spin chains in an optical lattice. *Nature*, 472(7343), 307–312.
- [90] Soltan-Panahi, P., Struck, J., Hauke, P., Bick, A., Plenkers, W., Meineke, G., Becker, C., Windpassinger, P., Lewenstein, M., & Sengstock, K. (2011). Multi-component quantum gases in spin-dependent hexagonal lattices. *Nature Phys.*, 7, 434–440.
- [91] Sørensen, A. S., Demler, E., & Lukin, M. D. (2005). Fractional quantum hall states of atoms in optical lattices. *Phys. Rev. Lett.*, 94, 086803.

- [92] Stuhl, B. K., Lu, H.-I., Aycock, L. M., Genkina, D., & Spielman, I. B. (2015). Visualizing edge states with an atomic Bose gas in the quantum Hall regime. *Science*, 349(6255), 1514–1518.
- [93] Tsui, D. C., Stormer, H. L., & Gossard, A. C. (1982). Two-dimensional magnetotransport in the extreme quantum limit. *Phys. Rev. Lett.*, 48, 1559–1562.
- [94] Warren, H. S. (2012). *Hacker's Delight*. Upper Saddle River, NJ: Addison-Wesley Professional, 2 edition edition.
- [95] Weitenberg, C., Endres, M., Sherson, J. F., Cheneau, M., Schauß, P., Fukuhara, T., Bloch, I., & Kuhr, S. (2011). Single-spin addressing in an atomic Mott insulator. *Nature*, 471(7338), 319–324.
- [96] Will, S., Best, T., Schneider, U., Hackermüller, L., Lühmann, D., & Bloch, I. (2010). Time-resolved observation of coherent multi-body interactions in quantum phase revivals. *Nature*, 465(7295), 197–201.
- [97] Wirth, G., Ölschläger, M., & Hemmerich, A. (2011). Evidence for orbital superfluidity in the p-band of a bipartite optical square lattice. *Nat. Phys.*, 7(2), 147–153.
- [98] Zupancic, P., Preiss, P. M., Ma, R., Lukin, A., Tai, M. E., Rispoli, M., Islam, R., & Greiner, M. (2016a). Ultra-precise holographic beam shaping for microscopic quantum control. *Opt. Express*, 24(13), 13881.
- [99] Zupancic, P., Preiss, P. M., Ma, R., Lukin, A., Tai, M. E., Rispoli, M., Islam, R., & Greiner, M. (2016b). Ultra-precise holographic beam shaping for microscopic quantum control. *arXiv:1604.07653*.
- [100] Zwierlein, M. W., Abo-Shaeer, J. R., Schirotzek, A., Schunck, C. H., & Ketterle, W. (2005). Vortices and superfluidity in a strongly interacting Fermi gas. *Nature*, 435(7045), 1047–1051.



THIS THESIS WAS TYPESET using L^AT_EX,
originally developed by Leslie Lamport
and based on Donald Knuth's T_EX.

The body text is set in 11 point Egenolff-Berner Garamond, a revival of Claude Garamont's humanist typeface. The above illustration, *Science Experiment 02*, was created by Ben Schlitter and released under CC BY-NC-ND 3.0. A template that can be used to format a PhD dissertation with this look & feel has been released under the permissive AGPL license, and can be found online at github.com/suchow/Dissertate or from its lead author, Jordan Suchow, at suchow@post.harvard.edu.